Göttingen Series in
X-ray Physics

Julia Sedlmair

Soft X-Ray Spectromicroscopy of Environmental and Biological Samples

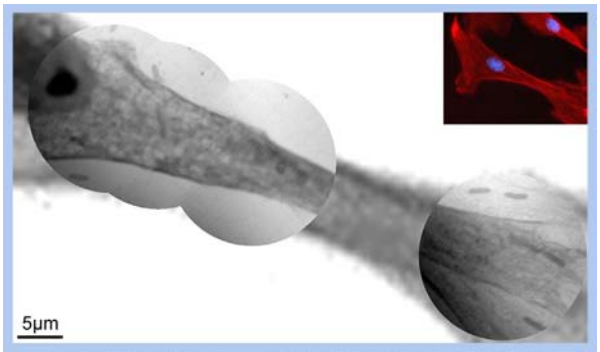

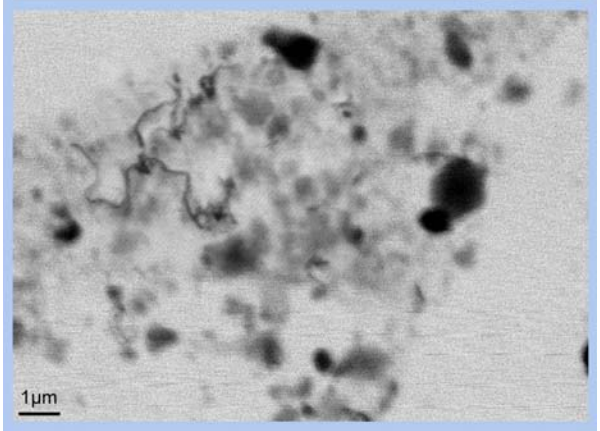

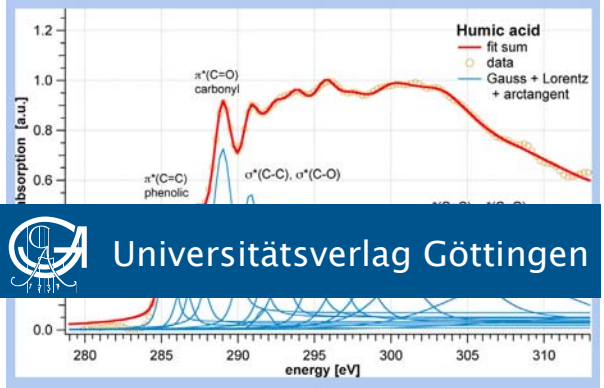

Universitätsverlag Göttingen

Julia Sedlmair

Soft X-Ray Spectromicroscopy of
Environmental and Biological Samples

Published in 2011 by Universitätsverlag Göttingen
as Volume 7 in the series „Göttingen series in x-ray physics“

Julia Sedlmair

Soft X-Ray Spectromicroscopy of Environmental and Biological Samples

Göttingen series in x-ray physics
Volume 7

Universitätsverlag Göttingen
2011

Bibliographische Information der Deutschen Nationalbibliothek

Die Deutsche Nationalbibliothek verzeichnet diese Publikation in der Deutschen Nationalbibliographie; detaillierte bibliographische Daten sind im Internet über <http://dnb.ddb.de> abrufbar.

This work has been supported financially by the DFG Collaborative Research Center SFB 755 "Nanoscale Photonic Imaging" (projects B5 and B1) and the Institute for X-Ray Physics at the Georg-August-University Göttingen.

Address of the Author
Dr. Julia Sedlmair
e-mail: jsedlma@gwdg.de

Dissertation zur Erlangung des
mathematisch-naturwissenschaftlichen Doktorgrades
„Doctor rerum naturalium"
der Georg-August-Universität Göttingen
vorgelegt von Julia Maria Sedlmair aus München

Referent: Prof. Dr. Tim Salditt
Koreferent: Prof. Dr. Hans-Ulrich Krebs
Tag der mündlichen Prüfung: 23.6.2011

Layout: Julia Sedlmair
Cover: Jutta Pabst
Cover image: Julia Sedlmair

http://univerlag.uni-goettingen.de
ISBN: 978-3-86395-036-1
ISSN: 2191-9860

Preface of the series editor

The Göttingen series in x-ray physics is intended as a collection of research monographs in x-ray science, carried out at the Institute for X-ray Physics at the Georg-August-Universität in Göttingen, and in the framework of its related research networks and collaborations.
It covers topics ranging from x-ray microscopy, nano-focusing, wave propagation, image reconstruction, tomography, short x-ray pulses to applications of nanoscale x-ray imaging and biomolecular structure analysis.
In most but not all cases, the contributions are based on Ph.D. dissertations. The individual monographs should be enhanced by putting them in the context of related work, often based on a common long term research strategy, and funded by the same research networks. We hope that the series will also help to enhance the visibility of the research carried out here and help others in the field to advance similar projects.

Prof. Dr. Tim Salditt, Editor
Göttingen February 2011

Contents

1 Motivation

Since their first observation by W.C. Röntgen in 1895, x-rays have added to science and fascinated researchers. Not only their property to permeate matter, but also the short wavelengths and the fact that they comprise the spectral area of atomic absorption allow for multiple applications.
In this work, environmental and biological samples were studied, which have one important characteristic in common: They are organic matter and thus largely comprised of carbon. Due to this, they belong to the category of samples that can be characterized using soft x-ray spectroscopy, microscopy and spectromicroscopy at energies around the carbon K-edge, located in the so-called water window, see Chapter 2. Within this unique spectral range, organic specimens can be studied within a water layer of several microns, providing the possibility to establish real or close-to-real sample environments.
This work is incorporated into the *Sonderforschungsbereich (SFB) 755 - Nanoscale Photonic Imaging*, mainly in the realms of project *B5* (*X-ray spectromicroscopy of biomolecular matter in the environment*). This *SFB* seeks to explore the dynamics and structure of organic specimens from small molecules to large cells, by combining microscopic, diffractive, spectroscopic, and mathematic techniques to invent or improve instrumental and analytical tools. The *SFB* has three complementary parts. Developing instrumental techniques and establishing theoretical methods, each build one part to enquire the regime in the nm-scale. The third part, investigating complex fluids with spectromicroscopy, deals with the application of these techniques and methods, and puts them into context with established methods. The work presented here, involving among other the examination of aqueous environmental samples or living cells by means of x-ray spectromicroscopy, fits therefore well into this framework.
Of course, there are many ways to use x-rays in research, for example in absorption, diffraction or scattering experiments. To provide an overview of this field, the theory of experiments based on x-ray absorption is described briefly in Chapter 2.
X-ray spectroscopy provides information about spatial orientation and chemical composition of a sample. Here, near edge x-ray absorption fine structure (NEXAFS) spectroscopy is applied to investigate chemical bonds by means of observing transitions of core electrons to unoccupied molecular orbitals. Such experiments have been conducted, among other, with polymers, proteins, crystals, as well as with environmental specimens such as humic substances [26, 52, 89, 188, 205].
State of the art x-ray microscopy based on zone plate lenses reaches a spatial resolution of 12 nm [39]. Due to differences in element specific absorption behavior, natural contrast

is formed either in transmission or in fluorescence mode within one sample for specific elements, addressed by choosing an adequate energy, and is visible in the micrographs [49, 196]. Even three dimensional information can be gained by stereo-microscopy or tomography [68, 119].
The combination of both techniques, termed x-ray spectromicroscopy, allows for high spectral and spatial resolution. This is extremely useful for the investigation of heterogeneous samples, like colloids, environmental samples, meteorite particles, or nano materials [1, 94, 197].
In the beginning, such experiments were only feasible using light generated by synchrotron facilities, because of the requirement of high brilliance. Currently, more and more compact x-ray sources are developed [142, 206] that are based on laser driven plasmas. Emitting either broad-band or line radiation they allow for spectroscopy or microscopy, yielding results almost comparable to synchrotron-based experiments [74, 143].
The experiments presented in this thesis are chosen in such a way that either the application of new instruments or methods are studied on different non-model sample specimens. Preceding, a short introduction illustrating the interaction between x-radiation and matter is given in Chapter 2. Thereafter, the instruments that were used for the experiments are described in Chapter 3, followed by the experimental Chapters 4 - 6.
Chapter 4 concerns x-ray spectroscopy of natural organic matter. Usually, such experiments are carried out at a synchrotron facility, for which beam time has to be granted. Efficient preparation is essential to fully make use of the limited experimenting time. Testing equipment and getting an understanding of the samples already in the home laboratory is therefore desirable, and could be an alternative to some extent. Here, heterogeneous samples of environmental origin are studied. Due to their complexity, an analysis with exact standards as is often used for crystals or polymers is complicated, and high spectral resolution is not always necessary. In order to characterize the sample spectra, a semi-empirical analysis approach was developed.
The second experimental part, described in Chapter 5 is thematically connected to Chapter 4, as again soil samples are studied. The focus lies more on the impact of anthropogenic carbon in the environment, i.e., the interaction between carbon nanotubes (CNTs) and soil colloids. In this case, bulk spectra would not be sufficient, but spatial resolution is needed, too. New materials like CNTs have to be characterized thoroughly - a task for which x-ray spectromicroscopy is ideally suited, because even aqueous samples can be assessed. Afterwards, dispersions of CNTs and soils are studied with increasing complexity of the samples. The results of Chapter 4 thereby facilitate the assignment of the spectral resonances. Owing to their characteristic spectral signature, the CNTs could also be used as samples to test an alternative evaluation method.
In Chapter 6, x-ray spectromicroscopy is applied to gain insight into the effect of different preparation methods on cells. In contrast to non-living matter, special care has to be taken regarding the preparation, when working with biomolecular specimens that are very sensitive to radiation damage. Besides, if the preparation method is too invasive, the essential point of the experiment might be missed. A compact instrument, this time an x-ray microscope was used for the first steps. But since chemical, i.e., spectral information was needed, too; the main part was carried out using x-ray spectromicroscopy at a synchrotron facility.

These three experimental parts of the thesis are then finalized by a summary given in Chapter 7.

2 Principles of X-Ray Spectroscopy and Microscopy

2.1 Interaction of X-Rays and Matter

In this section, the fundamentals of the interaction between x-rays and matter are summarized, equations and estimates are given, but not derived in greater detail. The descriptions are based mainly on Agarwal [3], Attwood [8] and Als-Nielsen and McMorrow [5].
The photoelectric absorption of x-radiation by matter is described by the Lambert-Beer law,

$$I = I_0 \, \mathrm{e}^{-\mu d} = I_0 \, \mathrm{e}^{-oD}. \tag{2.1}$$

The intensity I_0 of an incident x-ray beam traversing a sample with thickness d and absorption coefficient μ decreases exponentially to the intensity I. The expression in the exponent is often referred to as the optical density oD.
The Lambert-Beer law, or rather μ, contains all the physics needed to understand (x-ray) spectroscopy and microscopy. For spectroscopy, conclusions about the chemical components and bonds of a samples can be drawn from the way the absorption coefficient varies with energy. For microscopy, the fact of μ changing rapidly at absorption edges , see Fig. 2.1, is sufficient to provide contrast or even to perform elemental mapping.
Already found empirically in 1729 by P. Bouguer, the deduction of the Lambert-Beer law is straightforward. An electromagnetic wave of x-rays incident on matter, $\mathbf{E}(\mathbf{x}, t) = \mathbf{E}(\mathbf{x})\mathrm{e}^{-i\omega t}$, induces the bound electrons (mass m, charge e, natural oscillating frequency ω_0) in the sample to perform damped harmonic oscillations, with the damping coefficient γ,

$$m\ddot{\mathbf{x}} + m\gamma\dot{\mathbf{x}} + m\omega_0^2\mathbf{x} = -e\mathbf{E}\mathrm{e}^{-i\omega t}. \tag{2.2}$$

The ansatz $\mathbf{x}(t) = \mathbf{x}_0\mathrm{e}^{-i\omega t}$ leads to the solution for $\mathbf{x}$:

$$\begin{aligned} -m\omega^2\mathbf{x} - i\omega m\mathbf{x} + m\omega_0^2\mathbf{x} &= -e\mathbf{E} \\ \rightarrow \mathbf{x} &= \frac{e}{m}\frac{1}{(\omega^2 - \omega_0^2) + i\gamma\omega}\mathbf{E}. \end{aligned} \tag{2.3}$$

In the spectral range of soft x-rays, the interaction of the electrons in a sample and the incoming photons is almost only due to photoelectric absorption, because the cross-section of the latter is several orders of magnitudes higher than the scattering cross-sections. The absorptive part of the photoelectric cross-section is shown in Fig. 2.1. The absorption cross-section σ_{ab} and the absorption coefficient are related via $\mu = \frac{N_A\rho}{A}\sigma_{ab}$, with the Avogadro constant N_A, the mass density ρ and the atomic mass number A. The

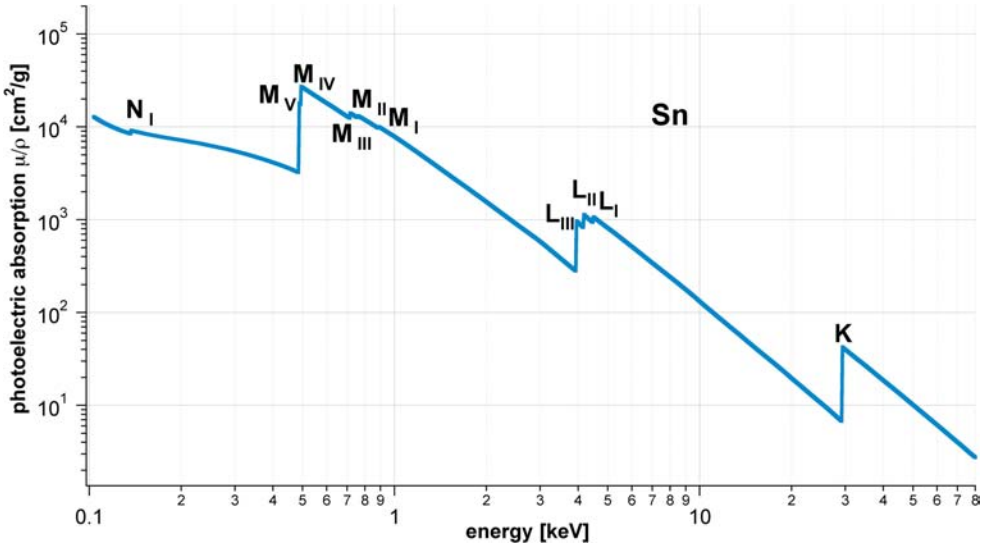

Figure 2.1: *Log-log plot of the mass photoabsorption coefficient μ/ρ of Tin (Sn) as an example to illustrate the different absorption edges for the K-, L-, M-, and N-shells. The data was taken from [132].*

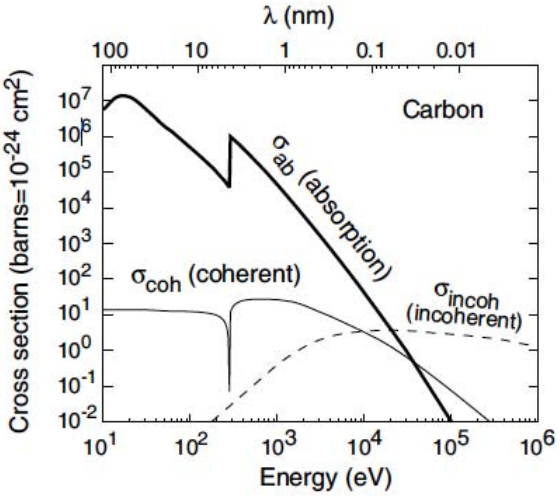

Figure 2.2: *Contributions from photoelectric absorption σ_{ab}, coherent scattering σ_{coh}, and incoherent or Compton scattering σ_{incoh} to photon cross-sections in carbon as a function of energy; adapted from Howells et al. [82], p. 836.*

solution for one single electron of Equ. (2.2) leads to its dipole moment **p**,

$$\mathbf{p} = -e\mathbf{x} = -\frac{e^2}{m}\frac{1}{(\omega^2-\omega_0^2)+i\gamma\omega}\mathbf{E}. \tag{2.4}$$

For a substance with N atoms (with Z electrons) per unit volume the polarization is given by

$$\mathbf{P} = -\frac{Ne^2}{m}\left(\sum_j \frac{f_j}{(\omega^2-\omega_{0_j}^2)+i\gamma_j\omega}\right)\mathbf{E}. \tag{2.5}$$

The f_j are the oscillator strengths, which are weighting factors for the probability that an electron at an atom level of frequency ω_{0_j} and damping factor γ_j undergoes a transition. In general, it holds that $\sum_j f_j = Z$, with Z the atomic number.
This yields the dielectric constant, $\epsilon(\omega) = \epsilon_0 + \frac{\mathbf{P}}{\mathbf{E}}$, with ϵ_0 the vacuum permittivity. Inserted into the equation for the refractive index, $n = \frac{\sqrt{\mu\epsilon}\omega}{\sqrt{\mu_0\epsilon_0}\omega} \simeq \frac{\sqrt{\epsilon}}{\sqrt{\epsilon_0}}$, whereby the magnetic permeability μ and the vacuum permeability μ_0 are negligible, this yields the dispersion relation:

$$\begin{aligned} n^2(\omega) &= \frac{\epsilon}{\epsilon_0} = 1 + \frac{\mathbf{P}}{\epsilon_0\mathbf{E}} \\ &= 1 - \frac{Ne^2}{m\epsilon_0\omega^2}\left(\sum_j \frac{f_j\omega^2}{(\omega^2-\omega_{0_j}^2)+i\gamma_j\omega}\right). \end{aligned} \tag{2.6}$$

Since for soft x-radiation it holds that $\omega^2 \gg \frac{Ne^2}{m\epsilon_0}$, the refractive index $n(\omega)$ can be approximated by

$$n(\omega) \approx 1 - \frac{1}{2}\frac{Ne^2}{m\epsilon_0\omega^2}\left(\sum_j \frac{f_j\omega^2}{(\omega^2-\omega_{0_j}^2)+i\gamma_j\omega}\right) = 1 - \frac{1}{2}\frac{Ne^2}{m\epsilon_0\omega^2} f^0(\omega). \tag{2.7}$$

In the last step, the effective atomic scattering factor $f^0(\omega) = \sum_j \frac{f_j\omega^2}{(\omega^2-\omega_{0_j}^2)+i\gamma_j\omega}$ was introduced, which can be expressed in complex components, too:

$$f^0 = f' + if''. \tag{2.8}$$

Hereby, f' is referred to as the effective number of electrons, which phase shifts an incoming wave, and f'' describes the attenuation. The values of f' and f'' are tabulated for photon energies from 10 eV – 30 000 eV in Thompson et al. [198] and CXRO [47], based on Henke et al. [72].
Using the classical electron radius $r_e = \frac{e^2}{4\pi m\epsilon_0 c^2} = 2.82\cdot 10^{-15}$ m and $\lambda = \frac{hc}{eE[\mathrm{eV}]}$, with E as the photon energy, this can be transformed further to

$$n(\omega) = 1 - \frac{Nr_e\lambda^2}{2\pi} f^0(\omega) = 1 - \frac{Nr_e}{2\pi}\left(\frac{hc}{eE}\right)^2 f^0(\omega). \tag{2.9}$$

Often, the refractive index is split up according to the complex components of f^0, resulting into

$$n = 1 - \delta - i\beta, \tag{2.10}$$

with $\delta = \frac{Nr_e\lambda^2}{2\pi} f'$ and $\beta = \frac{Nr_e\lambda^2}{2\pi} f''$.
After traversing a sample specimen of thickness d and refractive index n, a plane electromagnetic wave ψ with amplitude ψ_0 and wave vector k has the form $\psi = \psi_0 \mathrm{e}^{-iknd}$. The intensity I is calculated via

$$I = |\psi|^2 = \psi^* \psi \,. \tag{2.11}$$

Inserting the expression for n cancels out the phase shift δ, leaving only the contribution of the attenuation part β,

$$I = \psi_0^2 \mathrm{e}^{-2k\beta d} = I_0 \mathrm{e}^{-\mu d} \,. \tag{2.12}$$

This leads to the Lambert-Beer law, Equ. (2.1), with the linear absorption coefficient $\mu = 2k\beta = \frac{kNr_e\lambda^2}{\pi} f''$.
That means, f'' of a substance is directly measurable from the transmitted intensity through a sample. The corresponding f' is then obtainable using the Kramers-Kronig relations [8]. The units of μ are cm^{-1}, but often the mass absorption coefficient $\mu_\mathrm{m} = \frac{\mu}{\rho}$ is used, which is independent of the material density with units $\frac{\mathrm{cm}^2}{\mathrm{g}}$.
The reciprocal value of μ is called the attenuation length or penetration depth. In Fig. 2.3a,

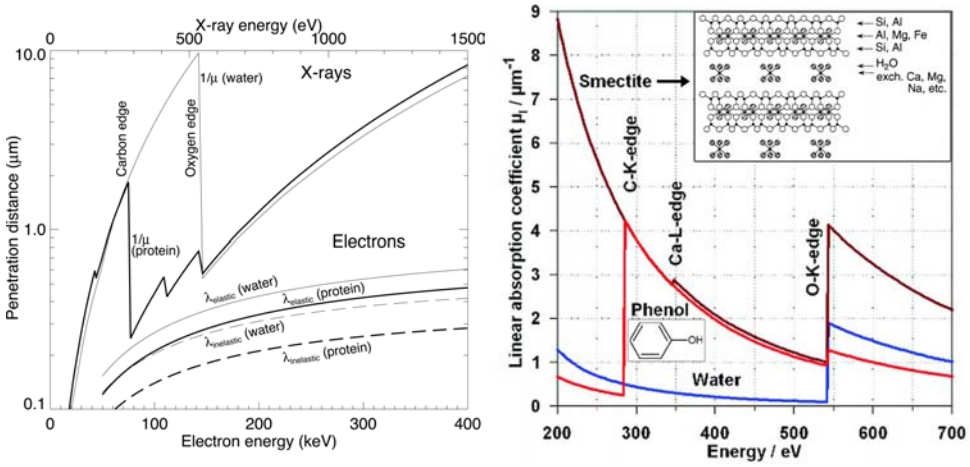

(a) *Penetration depth of soft x-rays* **(b)** *Linear absorption of soft x-rays*

Figure 2.3: a) *Comparison of penetration distances of water and a model protein for x-rays and electrons, adapted from Kirz et al. [107].* **b)** *Linear absorption cross section µ of the smectite clay mineral montmorillonite (structure in inset taken from Sparks [181]), an organic molecule (phenol, see inset) and of water as a function of x-ray energy; the absorption edges of oxygen, calcium and carbon are marked, adapted from Thieme et al. [197], modified.*

$\frac{1}{\mu}$ is plotted for water and a model protein against photon energies in the soft x-ray regime. For comparison, the mean free paths of electrons resulting from elastic and inelastic scattering, λ_elastic and $\lambda_\mathrm{inelastic}$, at the same energies is plotted. The mean free path is the average distance an electron can travel in a medium; here, protein and water. For matter

with a high carbon (C) content like proteins, the penetration depth of x-rays and the mean free paths of electrons is comparable between 100 eV and 400 eV. In water, however, the penetration depth of x-rays is approximately one order of magnitude higher. The spectral region between the K-shell absorption edges of carbon, at 284 eV, and oxygen (O), at 543 eV, is called the *water window*. Here, water absorbs much less than organic material, e.g., in biological or environmental samples, providing natural contrast. That way, it is possible to study such samples in hydrated state, achieving natural or close to natural sample environments.
Fig. 2.3b shows the linear absorption coefficients of water, an organic molecule (phenol, C_6H_6O), and the smectic clay mineral montmorillonite ($(M)_{0.33}(Al,Mg)_2(Si_4O_{10})(OH)_2 \cdot nH_2O$, where M refers to a metal cation such as Ca or Na) [181] as an example of an inorganic substance, to illustrate the possibility of studies in aqueous sample environment.
The interaction between x-radiation and matter can be used for sample investigations in three different ways, which will be explained in the following sections. Spectroscopy gives information about the chemical composition. Microscopy on the other hand uses the different absorption intensities of a sample to provide natural contrast in imaging. The combination of both, spectromicroscopy, comprises of sets or stacks of images recorded at different energies. That way, a spectrum for every pixel in the imaged area is available.

2.2 Spectroscopy

With NEXAFS (near edge x-ray absorption fine structure) spectroscopy, the change in the absorption coefficient $\mu(E)$ at a specific absorption edge can be analyzed and interpreted. It is therefore of great interest in many scientific fields, like polymer, biomolecular or environmental science, since local chemical information in complex and disordered materials is provided.

2.2.1 Definition

The description of NEXAFS firstly requires a definition of the terms involved. X-ray absorption spectroscopy (XAS) describes the change of the absorption coefficient μ, which has been mentioned in the preceding section. Absorption of a photon by an electron either leads to an ionized atom, if the photoelectron is lifted to the continuum, or to an excited atom, if the photoelectron fills an unoccupied atomic or molecular orbital state. The variations of μ at absorption edges are termed x-ray absorption fine structure (XAFS). For illustration, a hypothetical XAFS spectrum with the spectral features and ranges explained below is depicted in Fig. 2.4.
The spectral range of XAFS is not exactly determined, sometimes it is described as the "oscillatory structure [...] just above an absorption edge" [150], but more often it also includes the pre-edge region. The NEXAFS region of the x-ray absorption spectrum is dominated by strong photoelectron scattering. The width of this spectral region is not fixed, but can be approximated by comparing the interatomic distances d_i and the wavelength λ_{e^-} of the photoelectron:

$$E = \hbar\omega - E_{bind} = \frac{\hbar^2 k^2}{2m} = \frac{\hbar^2 2\pi^2}{m\lambda_{e^-}^2}. \tag{2.13}$$

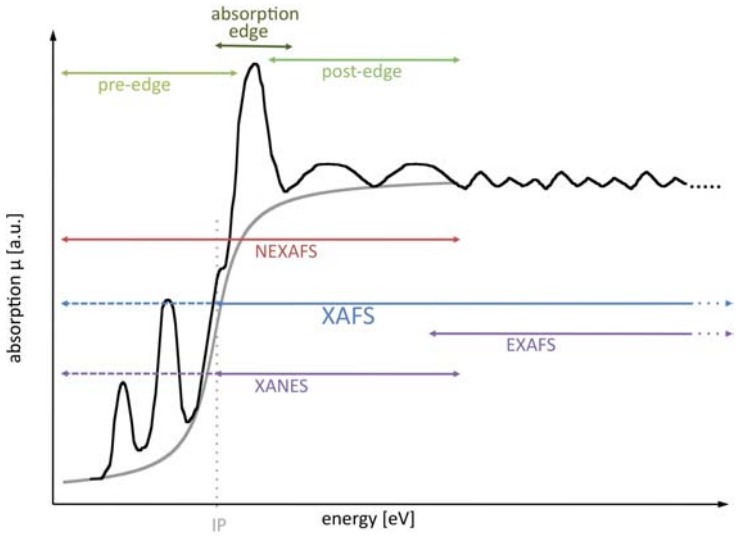

Figure 2.4: *Hypothetical XAFS spectrum to illustrate the approximate spectral regions for NEXAFS (or XANES) and EXAFS.*

Here, $\hbar\omega$ is the energy of the incident photon, E_{bind} the binding energy of the electron, m the electron mass and k its wave vector.

- For high E, $\lambda_{e^-} < d_i$ and single scattering dominates, leading to smaller changes in the absorption spectrum. This defines the EXAFS regime, which yields information about the bond lengths and coordination numbers.

- For low energies E, $\lambda_{e^-} > d_i$, multiple scattering occurs which defines the NEXAFS regime.

Typically, the NEXAFS spectral region extends from about 10 eV below to about 40 eV above an absorption edge, see Fig. 2.4. XANES (x-ray absorption near edge structure) often refers to the same region as NEXAFS, but sometimes the pre-edge features are not included.
To make things more complicated, some differences in linguistic usage of the terms *NEXAFS* and *XANES* are also found in the literature, however, they are more trends than rules. The first difference regards the energy range that is used for the experiments. For experiments with hard x-rays the term *XANES* is used more often, whereas for soft x-ray experiments the term *NEXAFS* is used. Furthermore, if fluorescence or electron yield is detected *XANES* is more frequent, whereas for transmission detection *NEXAFS* is more common. Another difference is correlated to the background of the author or experimentator. In publications by European authors, *NEXAFS* is used more frequently used than by authors from the US. In the following, only the term *NEXAFS* is used, to prevent confusion.

2.2.2 Theoretical Description of NEXAFS

The theoretical description of NEXAFS is still incomplete and no general concept explaining both NEXAFS and EXAFS exists. Then again, the theory of EXAFS is quite well understood. In EXAFS spectroscopy, χ is the central parameter instead of μ, and the so called EXAFS-equation describes the oscillations of the spectrum. The EXAFS-equation and χ are explained in section 2.2.2.1, in particular see Equ. (2.24) and (2.25).
The outline of the theory, the description of the spectra and the detection methods is mainly based on the fundamental book by Stöhr [187], a new summary and tutorials by Bunker [36, 37], the publications by J. J. Rehr and coworkers [6, 150–152], and the books by Als-Nielsen and McMorrow [5] and de Groot and Kotani [70]. As many approaches for a NEXAFS theory use the (E)XAFS picture, this will be explained first, followed by the MO (molecular orbital) picture, which provides a more intuitive way to analyze NEXAFS spectra of heterogeneous samples.

2.2.2.1 XAFS Picture

The modulations in μ result from the moving photoelectron, which has been released by an incident x-ray photon, and its interaction with neighboring atoms. The starting point is Fermi's Golden Rule, which describes the transition rate of a core level electron to the final state. For simplicity, only 1s core level (or K-shell) transitions are regarded here. The absorption of a given core level is then proportional to the transition amplitude:

$$\mu \propto \sum_f \left|\langle i\,|\mathcal{H}|\,f\rangle\right|^2 \delta(E_i+\hbar\omega-E_f) \tag{2.14}$$

$$\propto \sum_f \left|\langle i\,|\mathbf{p}\cdot\mathbf{A}(\mathbf{r})|\,f\rangle\right|^2 \delta(E_i+\hbar\omega-E_f) =$$

$$= \sum_f \left|\langle i\,|\hat{\boldsymbol{\epsilon}}\cdot\mathbf{r}\,\mathrm{e}^{i\mathbf{k}\cdot\mathbf{r}}|\,f\rangle\right|^2 \delta(E_i+\hbar\omega-E_f)\,, \tag{2.15}$$

with the initial $|i\rangle$ and the final $|f\rangle$ electron states and their corresponding energies $E_{i,f}$. The energy of the incident x-ray photon is $\hbar\omega$. The sum is taken over all unoccupied final states f. The Hamiltonian $\mathcal{H}$ describes the coupling of the electrons to the incident field. It can be written in terms of the initial and the final state of the photoelectron. $\mathcal{H}$ is proportional to $\mathbf{p}\cdot\mathbf{A}(\mathbf{r})$, with the momentum operator $\mathbf{p}$ of the electron and the vector potential $\mathbf{A}$ of the incoming wave; for the wave vector $\mathbf{k}$ and $\hat{\boldsymbol{\epsilon}}$ the electric polarization vector it holds that $\mathbf{k}\perp\hat{\boldsymbol{\epsilon}} \rightarrow \mathbf{A}(\mathbf{r},t) \cong \hat{\boldsymbol{\epsilon}} A_0 \mathrm{e}^{i\mathbf{k}\cdot\mathbf{r}}$. The final form of Equ. (2.14) is achieved using commutation relations.
The matrix element $\langle i\,|\hat{\boldsymbol{\epsilon}}\cdot\mathbf{r}\,\mathrm{e}^{i\mathbf{k}\cdot\mathbf{r}}|\,f\rangle$ can be expanded to

$$\langle i\,|\hat{\boldsymbol{\epsilon}}\cdot\mathbf{r}\,\mathrm{e}^{i\mathbf{k}\cdot\mathbf{r}}|\,f\rangle \approx \langle i\,|\hat{\boldsymbol{\epsilon}}\cdot\mathbf{r}|\,f\rangle + i\,\langle i\,|(\hat{\boldsymbol{\epsilon}}\cdot\mathbf{r})(\mathbf{k}\cdot\mathbf{r})|\,f\rangle + \ldots\,, \tag{2.16}$$

where the first term is the dipole term, the second the quadrupole term etc.. That means, for deep core excitations, the spatial dependence of $\mathbf{A}$ can be neglected, such that $\mathrm{e}^{i\mathbf{k}\cdot\mathbf{r}} \simeq 1$. Approximating the core state of an atom as a hydrogen atom with $e \rightarrow Ze$, it can be concluded from the ratio of both terms that the quadrupole term is negligible for low Z

atoms [36], e.g., for C the ratio of quadrupole to dipole element is ~ 2.2%.
Typically, for XAFS calculations the final state Hamiltonian $\mathcal{H}'$ is used, which is referred to as the *final-state-rule* [13] – in the following variables of the final state of the electron are indicated with a prime. The final states of the electron are calculated in the presence of a screened core hole. Vibrational effects, inelastic losses, and ground state exchange correlation functions are described by a complex valued self-energy or optical potential $\Sigma(E)$. Finding accurate ways to calculate $\Sigma(E)$ is one of the major challenges in XAFS theory. The final states are then represented as a quasi-particle moving through the optical potential - this approach is called the *standard quasi-particle model* and forms the basis for most XAFS calculations [151]. Within this model, the final states ψ_f of the quasi-particle solve the equation (Dyson equation)

$$\mathcal{H}'\psi_n = \left(\frac{p^2}{2m} + V'_{\text{coul}} + \Sigma(E)\right)\psi_n = E\psi_n, \tag{2.17}$$

where the final state Hamiltonian $\mathcal{H}'$ is comprised of the energy of the photoelectron $\frac{p^2}{2m}$, the Coulomb potential of the final state V'_{coul}, and the optical potential $\Sigma(E)$.
The reason for using the final state approach becomes clear, when expressing Equ. (2.15) as

$$\mu \propto \sum_f \langle i\ |\hat{\boldsymbol{\epsilon}}\cdot\mathbf{r}'|\ f\rangle\,\delta(E-E_f)\,\langle f\ |\hat{\boldsymbol{\epsilon}}\cdot\mathbf{r}|\ i\rangle\ . \tag{2.18}$$

With $\mathbf{r}'$ the position of the final state of the electron and $E = E_i + \hbar\omega$, one avoids to explicitly calculate the final state, which is a bottleneck in XAFS calculations. Instead, it is common to use the one-particle Green's function of the photoelectron,

$$\begin{aligned} G(E) &= \frac{1}{E-\mathcal{H}'+i\eta} = \\ &= \sum_f |\ f\rangle\,\frac{1}{E-E_f+i\eta}\,\langle f\ |, \quad \eta\to 0^+, \end{aligned} \tag{2.19}$$

with η a net lifetime. Using

$$-\frac{1}{\pi}\text{Im}G = \sum_f |\ f\rangle\,\delta(E-E_f)\,\langle f| \tag{2.20}$$

leads to

$$\mu(E) \propto -\frac{1}{\mu}\text{Im}\,\langle i\ |\hat{\mathbf{e}}\mathbf{r}'\,G(\mathbf{r},\mathbf{r}',E)\,\hat{\mathbf{e}}\mathbf{r}|\ i\rangle\ . \tag{2.21}$$

This means that the spectrum is directly obtained from the Green's function, without the necessity to compute the final states.
The remaining difficulty is to find an appropriate potential. As mentioned before, the photo-electron traverses the sample as a quasi-particle in an optical potential and is scattered off the other electrons taking different paths. Depending on the elaborateness of the theory, scattering only of the nearest neighbor (single scattering) or multiple scattering

(MS) is taken into account.
In MS theory, a localized potential is assigned to each atom at the positions **R**:

$$V'_{\text{coul}} + \Sigma(E) = \sum_{\mathbf{R}} v_{\mathbf{R}}(\mathbf{r} - \mathbf{R}) \,. \tag{2.22}$$

The potential of the other atoms as seen by the particle is most often described as the muffin-tin (MT) potential V_{mt}, sketched in Fig. 2.5. In the MT potential, atoms or ions are

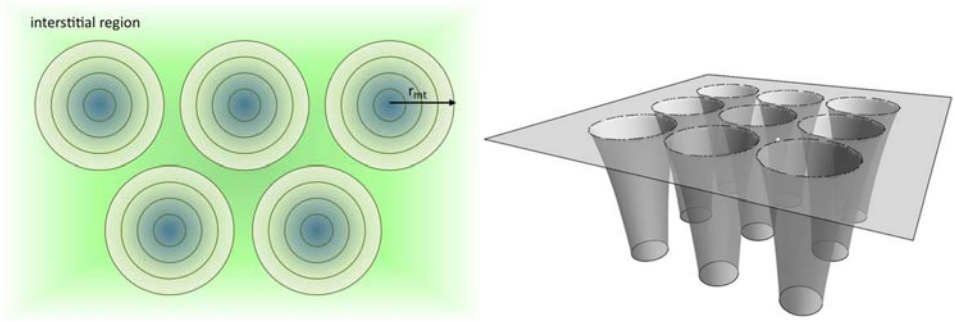

(a) **(b)**

Figure 2.5: a) *MT potential, sketched as spherical two dimensional approximation for a crystal lattice.* **b)** *Three dimensional model of the MT potential, taken from Bunker [36].*

described as spherical potentials with radius r_{mt} around the core region of the atoms in a sample, with r_{mt} usually in the range of half the interatomic distance, see e.g., Ashcroft and Mermin [7]. In the interstitial regions, the potential is constant (*muffin-tin zero*). Thus,

$$V_{mt} = \begin{cases} V(\mathbf{r} - \mathbf{R}) & |\mathbf{r} - \mathbf{R}| < r_{mt} \quad \text{core region} \\ V(r_{mt}) = const. & |\mathbf{r} - \mathbf{R}| < r_{mt} \quad \text{interstitial region} \,. \end{cases} \tag{2.23}$$

The MT approximation is often used to describe the band structure of atoms. Therefore, the MT approximation of the potential works best for densely packed structures. For the NEXAFS pre-edge region, the MT potential is not fully satisfactory and full MS has to be taken into account. This stems partly from the fact that the real core potential is not spherical and the real interstitial region does not have a constant potential. Apart from that, alternative approaches are applied like real-space multiple scattering (RSMS) [6] or finite difference method (FDM) [101], which avoids the muffin tin approximation.
The Green's formalism mentioned above shows the connection between NEXAFS and EXAFS theories in the following way. It is separable into contributions from the central atom (μ_0) and a varying background from the neighboring atoms ($\mu_0\chi$):

$$\mu = \mu_0(1 + \chi) \,. \tag{2.24}$$

The expansion of G and the exact expressions for μ_0 and χ in terms of G are found in Ankudinov et al. [6] and Rehr and Alberts [150]. It should be noted that the electronic

density of states ρ can be expressed similarly.
Further aspects that are included in the XAFS picture will be mentioned only briefly. To limit the computing time of the MS approach, several filters to reduce the number of paths taken by the electron are used. In the first approaches, the incident x-rays were described as plane wave, but very soon, this approach was changed. Modern computations and programs use curved wave approximations.
Rewriting Equ. (2.24) into $\chi = \frac{\mu-\mu_0}{\mu_0}$ leads to the interpretation of the correction factor χ as the fractional change in the absorption coefficient due to the neighboring atoms. That way, structural information is separated from the energy dependence of the absorption coefficient. The factor χ is the key expression for describing EXAFS. Based on several parameters, such as mean free path of the photoelectron $\lambda(=\frac{1}{k})$ or the radius R of the so called coordination shell of neighboring atoms where the electron scatters, Sayers et al. [160] developed a quantitative expression for χ, which now is called the EXAFS-equation:

$$\chi(k) = -\sum_j S_0^2 \frac{N_j}{kR_j^2} |f_j(k)| \mathrm{e}^{-\frac{2R_j}{\lambda(k)}} \mathrm{e}^{-2\sigma_j^2 k_j^2} \sin\left(2kR_j + 2\delta_1(k) + \Phi_j(k)\right). \tag{2.25}$$

The amplitude-reduction factor S_0^2 describes the influence of intrinsic effects, which stem from the creation of the core hole. It is close to 1 and was included in the original formula, but is added for completeness. As the theoretical description became more accurate and the computable spectral range extended more and more towards lower energies until reaching the edge, the weighting factor S_0^2 was introduced. Thus, especially when calculating features of the NEXAFS regime, S_0^2 is important. N_j is the number of atoms in the j^{th} coordination shell at distance R_j. $f_j(k)$ is the backscattering amplitude with phase $\Phi_j(k)$; $f_j(k) = |f_j(k)|\mathrm{e}^{i\Phi_j(k)}$. $\delta_1(k)$ is the partial wave shift of the central atom. The Debye-Waller factor $\mathrm{e}^{-2\sigma_j^2 k_j^2}$ takes thermal effects into account, describing a displacement of σ_j of the atoms in shell j from the position R_j. Using curved wave approximations, $f(k)$ is replaced by an effective backscattering amplitude $f_{\text{eff}}(k)$, after which the program package FEFF is named, a program for ab-initio multiple scattering calculations for XAFS (FEFF-Project). A detailed derivation is for example found in Als-Nielsen and McMorrow [5].
At the absorption edge, the MS approach does not converge and not only scattering but also bonding effects are important. Therefore, the (E)XAFS picture yields only a good approximation above the absorption edge, even if full MS is applied. The central point is the choice of the right potential for the description of the interatomic regions and the electronic structure.

Pre-edge region. For the pre-edge region, several approaches have been proposed, which are complementary to the method outlined above. Using the static exchange (STEX) approach, the spectra of amino acids were calculated [38, 102, 224]. Another approach is the time dependent density function theory as proposed by Buckley and Besley [34], which was used to compute the NEXAFS spectra of amino acids and proteins. For the calculations of benzene rings and other aromatic structures Bâldea et al. [10] used second order algebraic diagrammatic construction (ADC(2)).
These methods also start with Fermi's Golden Rule, but then use different assumptions,

e.g., to get different potentials [101]. The drawback here is that the relative energies of the contributions to the NEXAFS spectra are achieved quite well, e.g., the distance between the π^* and σ^* peaks and their distance from the computed absorption edge, but the absolute peak heights, energies and absorption edge position still need improvement. In contrast to the EXAFS theory, these models often are insufficient for the calculations above the absorption edge.

It should be noted that the theoretical approach explained above provides very good results for ordered structures such as crystals and metals. The understanding of the underlying principles is of key importance to interpret NEXAFS spectra. For (heterogeneous) organic compounds, however, the timescales to compute the NEXAFS spectra would be huge.

2.2.2.2 MO Picture

The picture of discrete molecular orbitals (MO), also commonly used in NEXAFS spectroscopy provides a more intuitive access. In general, XAFS probes the unfilled antibinding orbitals.
Since NEXAFS spectra are more often interpreted than mathematically analyzed, MO theory allows the assignment of spectral features by relatively simple symmetry considerations. The symmetries in MOs are best described using group theory, which also facilitates the labeling of the distinct orbitals. R. S. Mulliken won the Nobel price in 1966 for the development of MO theory [127, 128].
MOs arise from linear combination of atomic orbitals (LCAO). The simplest version of MOs belong to diatomic molecules, either homo- or heteroatomic, as illustrated by carbon monoxide (CO) and diatomic carbon (C_2) in Fig. 2.6. Conventionally, the z-axis lies on the connecting axis between the two atoms. Since MOs have a strong directional character which is exploited in NEXAFS spectroscopy of surfaces [188]. MOs of diatomic molecules are symmetric, but in heteroatomic molecules this is not the case. However, the resulting orbitals can still be labeled π and σ. σ-orbitals are always present, but the formation of π-orbitals depends on the atoms involved. Only orbitals of the same symmetry can mix, e.g., p_x and p_y or p_z and s.
Including the valence bond concept in MO theory allows for the determination of ionization energies and adds degeneracy to the MOs. The MOs then evolve from hybridization of atomic orbitals to localized hybrid MOs of equal energies, e.g., the sp^2-hybridization of aromatic C rings in carbon nanotubes. The MOs of larger molecules are established by combining the MOs of smaller building blocks, also called linear combination of bond orbitals (LCBO).
This is possible, because LCAO states that the wave function ψ_{MO} of a MO can be written as a linear combination of hybrid or atomic orbitals ϕ_k [187, p. 61],

$$\psi_{\mathrm{MO}} = \sum_{k=1}^{M} a_{\mathrm{MO},k}\phi_k \,. \tag{2.26}$$

Introducing a Hamiltonian, it is feasible to compute the characteristic self-energies of the orbitals from the trace of the matrix $\langle\phi_k|H|\phi_k\rangle$ and the interaction energies between the

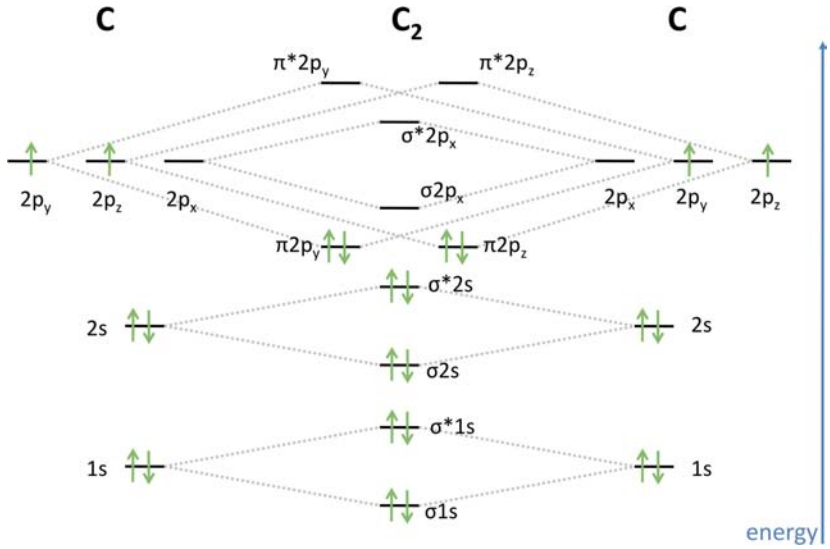

(a) *MOs of* C_2

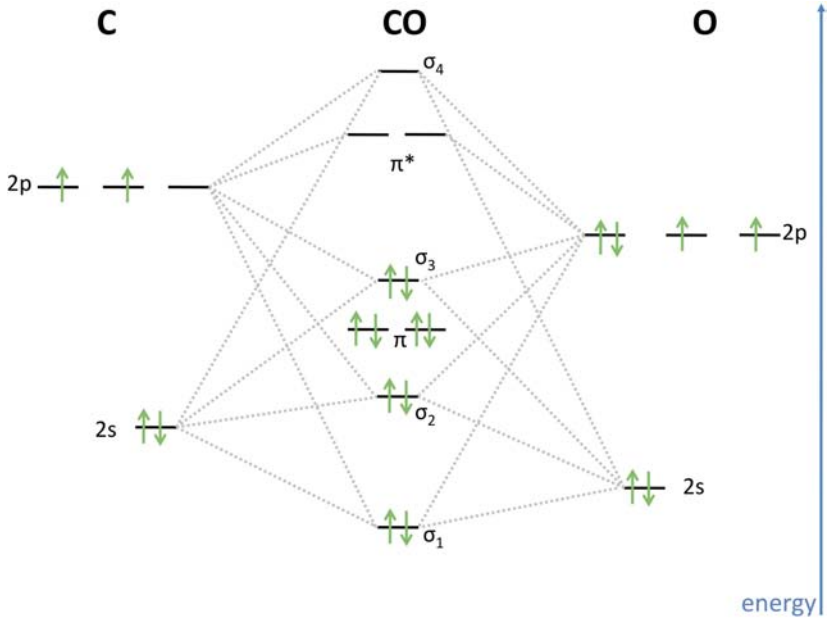

(b) *MOs of CO*

Figure 2.6: *Diagram illustrating the formation of MOs in diatomic molecules; as an example* **a)** C_2 *and* **b)** *CO were chosen. Antibinding MOs are denoted by a star. Degeneracy of the p-orbitals and inversion symmetry (gerade/ungerade) are not specified.*

orbitals from $\langle\phi_k|H|\phi_l\rangle$. The transitions of a core shell electron are determined by dipole (and quadrupole) selection rules following Pauli's principle. The transitions are mainly dipole transitions; quadrupole transitions are much weaker. Expressed with quantum numbers, the selection rules are $\Delta l = \pm 1$, $\Delta j = \pm 1$ and $\Delta s = 0$, for dipole transitions, and $\Delta l = \pm 2$ for quadrupole transitions, which are weaker by three orders of magnitude. That means that for K and L_I shell electrons, only the transitions s→p are allowed, for $L_{II,\,III}$ electrons, p→d and p→s are allowed, or at least the final state needs a contribution of one of these orbitals. The spin is conserved in the transitions.

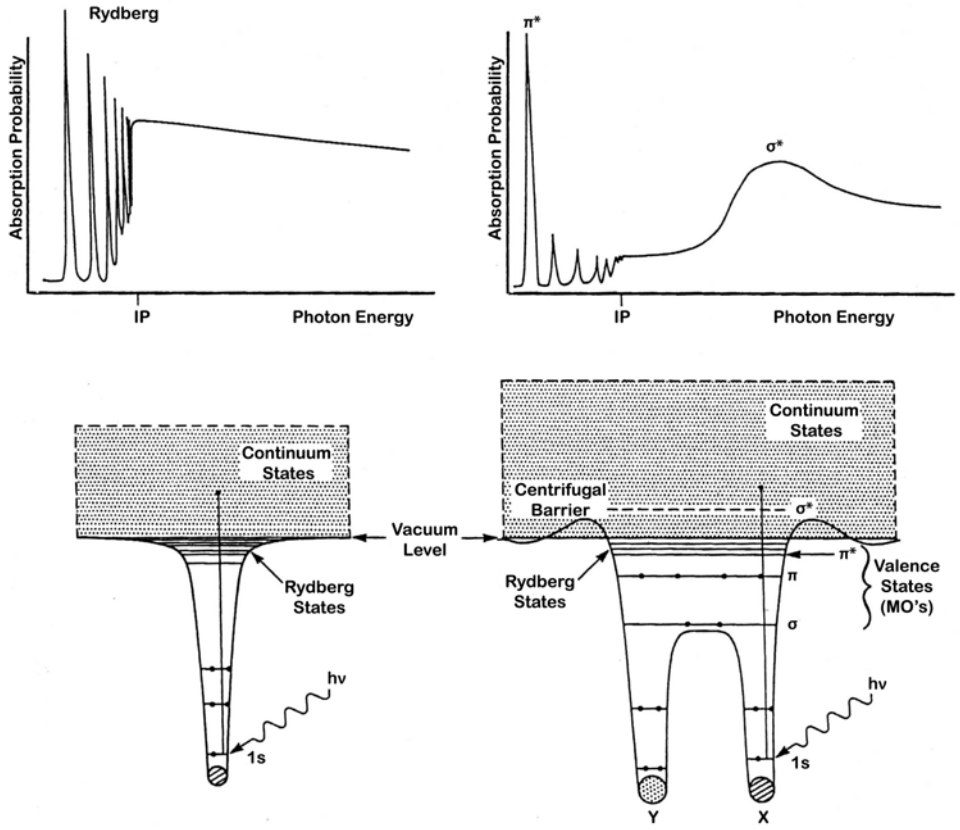

Figure 2.7: *Schematic potentials and 1s spectra of an atom (left) and a diatomic molecule (right), adapted from Stöhr [187], p. 85.*

In Fig. 2.7, energy schemes of the effective potentials of an atom and a diatom and the corresponding K-shell NEXAFS spectra are shown. The potential barrier of the diatomic potentials results from writing the Schrödinger equation in spherical coordinates, which gives rise to a centrifugal term $\frac{l(l+1)\hbar^2}{2mr^2}$. The resulting valence bond is illustrated and the unfilled orbitals are shown, too. Due to the interaction between the Coulomb potential and the core hole after the electron is excited, the π^* orbital is pulled below the vacuum

energy level. Therefore, 1s→ π^* transition peaks are located below the ionization point.
The correlation between the XAFS picture and the MO picture can be established by understanding the wavefunctions yielded by MS theory as describing the contour maps of the MOs. It should be noted, however, that most calculations of NEXAFS spectra, either using the XAFS oder the MO approach deal with relatively simple molecules, crystals and better results are achieved for higher Z elements like transition metals, for instance manganese oxide (MnO) [36, 124] or ceramics [192]. In the following section, typical features in a K-shell NEXAFS spectrum are listed.

2.2.3 General Characteristics of NEXAS Spectra

As mentioned above, NEXAFS probes the allowed transitions of an electron inside a molecule or atom, thereby giving information about the chemical environment. A NEXAFS spectrum consists of three overlapping regions, the pre-edge region, the absorption edge and the post-edge region, as illustrated in Fig. 2.4 and 2.7.
Since the π^* orbitals of a molecule are below the vacuum level, they have a localized character, which leads to sharp and narrow peaks in the pre-edge region. The electron transitions go to empty but bound MOs. The spectral width depends on the lifetime of the excited state, i.e., the core hole lifetime, and also on the length of a chemical bond. (However, intrinsic properties of the spectrometer used, might lead to an even wider broadening.) Information about oxidation state, local geometry and chemical bonds, e.g., double or triple bonds, bond length, can be gained from these transitions.
At energies around the edge, transitions to the continuum or Rydberg orbitals take place. As for large molecules, however, the latter do not result into high peaks. They rather lead to a broad background and mix with hydrogen-derived antibonding MOs. From the analysis of this region, a possible chemical shift in the oxidation state is observable.
The post-edge region originates from transitions to unbound MOs, i.e., σ^* orbitals, and (depending on the detection method) multiple scattering of the photoelectron. The atomic bond gives rise to a centrifugal barrier, therefore, the σ^* resonances are located above the absorption edge. Being close to or even overlapping with the EXAFS regime, ab-initio calculations are possible. Furthermore, the position of neighboring atoms, i.e., bond lengths might be inferred.
The positions of the ionization point (IP) and the peaks of small molecules are directly linked to the π and σ orbitals in the molecules. In a simple approach, the peaks and IPs of NEXAFS spectra of larger molecules are viewed as a combination of the spectra of small-molecule building blocks. This approach is also used here but, as will be discussed later, the chemical bond in such large samples influence each other, too. Especially in heterogeneous samples without ordering such as environmental or biological specimens, an exact approach to calculate the NEXAFS spectra is not possible.

2.2.4 Detection and Analysis Methods

The detection of NEXAFS spectra can be achieved by three different methods: fluorescence yield or electron yield and absorption, schematically depicted in Fig. 2.8.
Due to the excited electron, a core hole is formed, which is filled by an electron from a

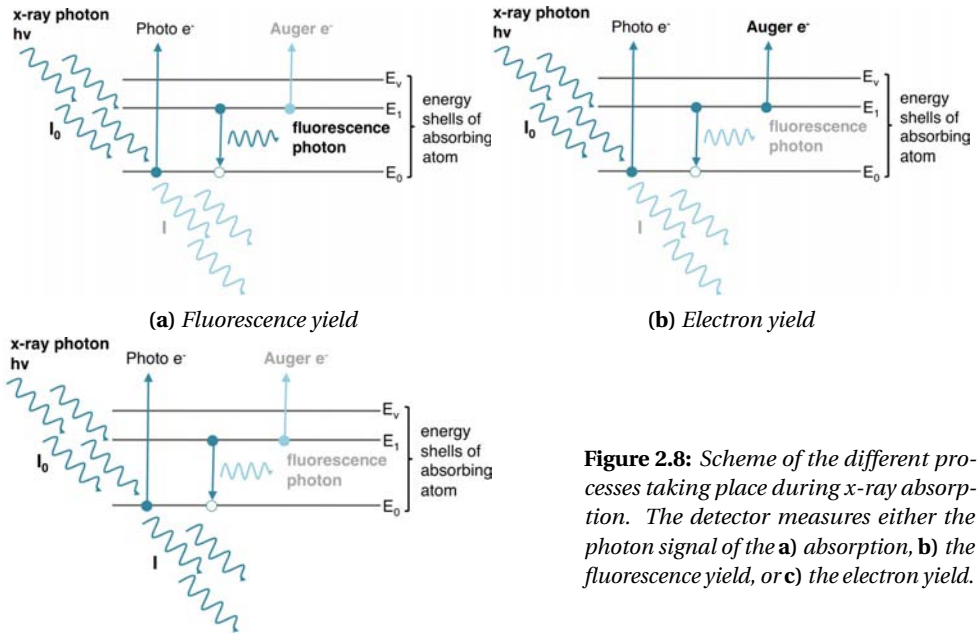

(a) *Fluorescence yield*

(b) *Electron yield*

(c) *Absorption*

Figure 2.8: *Scheme of the different processes taking place during x-ray absorption. The detector measures either the photon signal of the* **a)** *absorption,* **b)** *the fluorescence yield, or* **c)** *the electron yield.*

higher shell. In case of fluorescence (Fig. 2.8a), the atom relaxes by emitting a photon with a characteristic energy. In the non-radiative Auger process (Fig. 2.8b), the released energy of the transition of the electron from a higher shell is transferred to another electron (not necessarily from the same shell), which is emitted, again with characteristic energy. The index of the Auger electron consists of three capital letters, representing the shell of the original hole, the shell of which this vacancy is filled and the shell of which the Auger electron is emitted.
For absorption measurements (Fig. 2.8c), the Lambert-Beer law applies, i.e.,

$$\mu(E) \propto \ln\left(\frac{I}{I_0}\right). \tag{2.27}$$

This method was used for the work presented here, because all samples had a sufficiently small thickness and the concentration of the studied element (mainly C) was high enough. A major advantage of absorption measurements is that the background signal only adds as a constant.
Fluorescence and Auger yield were not measured here, but for completeness the relevant detection relations shall be addressed briefly. Especially for low concentrations or thick samples, the fluorescence yield (Fig. 2.8a) is detected, because it is capable of sensing even concentrations in the ppm-range. Furthermore, the detector is placed in front of the

sample, thereby yielding surface-specific information. The absorption coefficient scales as

$$\mu(E) \propto \frac{I_f}{I_0}. \tag{2.28}$$

The detection of the electron yield (Fig. 2.8b) scales as

$$\mu(E) \propto \frac{I_{EY}}{I_0}. \tag{2.29}$$

The probabilities of both processes, which depend on the atomic number Z and the shell of the photoelectron, are depicted in Fig. 2.9.

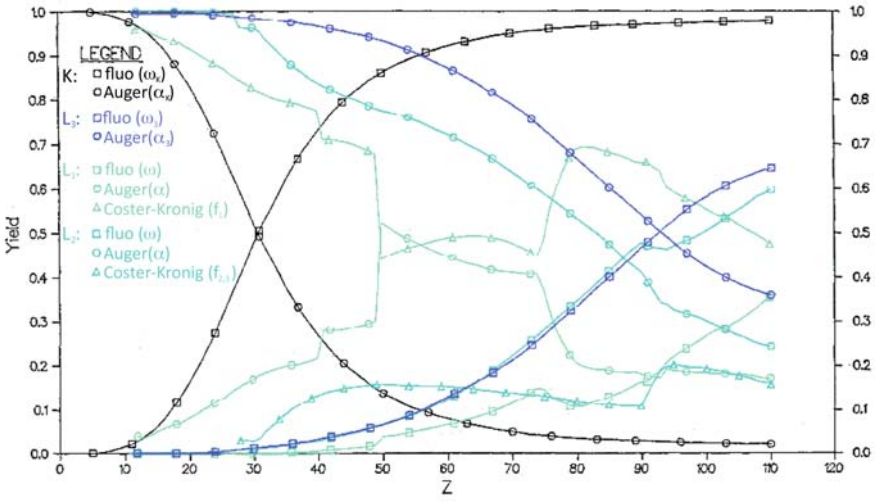

Figure 2.9: *Fluorescence and Auger yields for the K and L shells as a function of the atomic number Z. For completeness, for the $L_{1,2}$-shells the Coster-Kronig yield is plotted, too, but is not referred to any further. Adapted from [109].*

Spectral measurements can be performed using two different methods. If the source emits broadband radiation and is not monochromatized, the emitted or transmitted intensity has to be detected with an energy sensitive detector. If the energy of the source, e.g., from a synchrotron beamline, can be adjusted, the recorded intensities are synchronized with the monochromator. The setup of a table-top spectrometer with a laser-driven source is described in section 3.1.1.
A classical and commonly used approach of analyzing NEXAFS spectra consists of representing the absorption edge with an arctangent curve and fitting the peaks with Gaussian or Lorentzian curves, or with Voigt profile, the combination of both. Due to the challenging theoretical explanation of NEXAFS, a unique fitting algorithm is hard to find. In the course of this work, an alternative to the classic approach is presented and will be explained in detail in Chapter 4.

2.3 X-Ray Microscopy

Optical microscopes using light in the visible spectrum (400 nm - 800 nm) reach the resolution limit at 200 nm, as stated by Abbé ($d = \frac{\lambda}{2n\sin\alpha}$). To resolve smaller structures, shorter wavelengths have to be applied. Another way to achieve high resolution images, e.g., of cells is the application of STED microscopy (stimulated emission depletion) [53, 214], STORM (stochastic optical reconstruction microscopy) [83, 84], or PALM (photoactivated localization microscopy) [25, 156], at what the samples are still alive, but certain molecules are marked with fluorescence dyes. However, this is not the natural state of the samples and furthermore, only the stained parts are visible, whereas the rest has to be imaged using other techniques, often involving more sample preparation.
Electron microscopy has developed as one of the primary imaging techniques [115, 154, 175, 186, 203]. However, the small penetration depth of electrons requires the samples like cells to be fixed and cut into small sections of less than 0.5 µm. Besides, the samples have to be embedded before slicing – a process, which might have a significant impact on their structure [119]. Furthermore, with CDI (coherent diffractive imaging) [65, 84, 171, 194] there is also an alternative by calculating the image using the diffractive pattern of a sample.
For x-ray microscopy, no staining of the sample is needed, because contrast results naturally from differences in the absorption coefficient μ, which depends directly on the elemental composition, and thickness variations in a sample [107, 217], as described in section 2.1. Another advantage is the possibility to study aqueous samples in water layers of up to 10 µm diameter [197]. Using cryo-fixation, x-ray tomography is also realizable [113, 119, 140, 195].
X-rays have a comparably large penetration depth, see Fig. 2.3, and with a range of 10 nm - 0.01 nm not the wavelength is the limiting resolution factor at present but rather the optical elements. With a refractive index close to one, Fresnel zone plates, serving as diffractive lenses are used. Other approaches work with reflective optics such as a multilayer coated mirrors [75, 122, 126, 202]. At present the best resolution with such microscopes is 12 nm [39]. X-ray microscopes can either work as full-field or scanning microscopes, described in more detail subsequently.
The description of x-ray microscopy theory and instruments used in this thesis primarily follows Attwood [8] and Howells et al. [82], chap. 13.

2.3.1 Fresnel Zone Plates

For the x-ray microscopes used here, Fresnel zone plates are employed as focusing elements. Zone plates can be regarded as circular diffraction gratings. Diffraction by gratings leads to constructive interference (of m-th order) at a certain angle α, if the difference in path length d of the interfering beams is a multiple of the wavelength,

$$\sin\alpha = \frac{m\lambda}{d}\,. \tag{2.30}$$

In order to focus the first order of diffraction into one point, the width of the zones of a zone plate have to decrease with increasing distance from the center, resulting in an

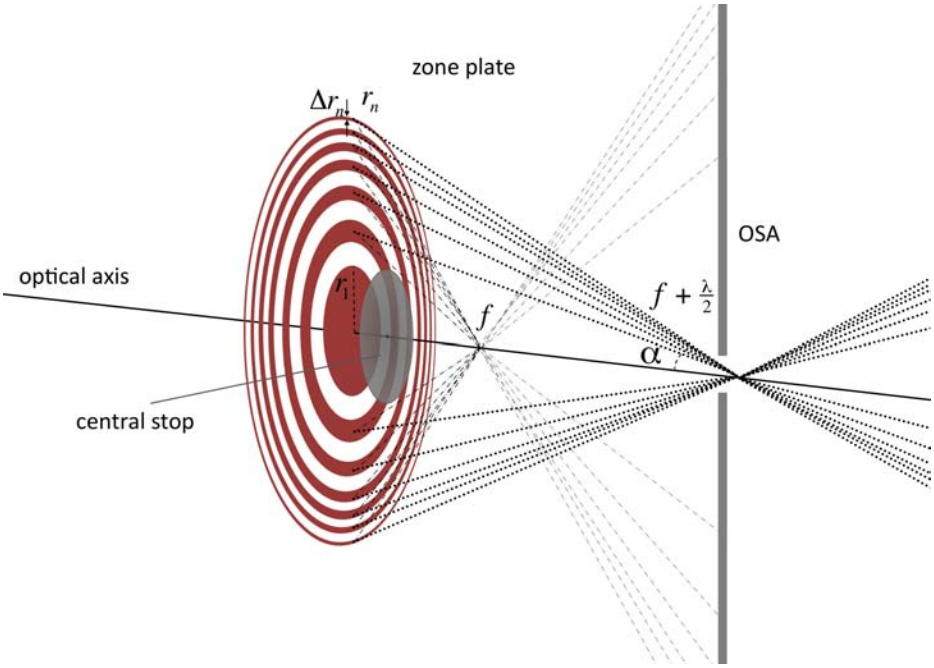

Figure 2.10: *Sketch of a Fresnel zone plate lens with n alternating opaque and transparent zones, showing the first and third order of diffraction, in case of plane wave illumination. An order sorting aperture (OSA) blocks unwanted radiation of higher orders. More information is given in the text.*

increasing diffraction angle as illustrated in Fig. 2.10. Using Pythagoras, this gives

$$f^2 + r_n^2 = \left(f + \frac{n\lambda}{2}\right)^2 \quad \Leftrightarrow \quad \sqrt{r_n^2 + f^2} - \frac{n\lambda}{2} = f\,. \tag{2.31}$$

Expanding the square root, this leads to the focusing condition in fourth order

$$r_n^2 = f n\lambda + \frac{n^2\lambda^2}{4}\,. \tag{2.32}$$

Keeping in mind that $f \gg \frac{n\lambda}{2}$ is usually fulfilled for x-rays, this simplifies to

$$r_n \simeq \sqrt{f n\lambda}\,. \tag{2.33}$$

In terms of higher orders m of diffraction, the path difference has to be correspondingly longer, i.e., $\frac{mn\lambda}{2}$ instead of $\frac{n\lambda}{2}$. From this it can be inferred that

$$r_n^2 \simeq f_m m n\lambda \quad \Leftrightarrow f_m = \frac{f}{m}\,. \tag{2.34}$$

This also demonstrates that the focal lengths for higher orders are shorter, as depicted in Fig. 2.10, and can therefore be blocked by an order sorting aperture (OSA). The radiation of the zeroth order is blocked by a central stop.

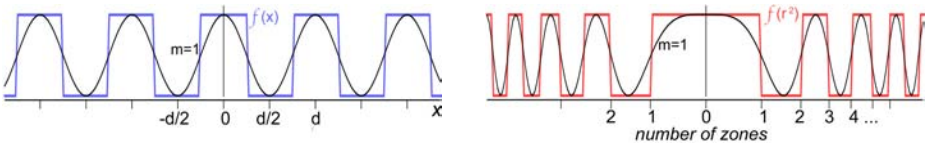

(a) *Grating* **(b)** *Zone plate*

Figure 2.11: *Sketch of a* **a)** *regular grating and* **b)** *a zone plate in terms of Fourier components. Only the first order term of the diffracted energy is shown.*

Thus, only a fraction of the incident light is transmitted by a zone plate, which can be calculated. To do so the transmission of a regular periodical grating is considered first (Fig. 2.11 a).
For the calculation of the transmission for opaque and transparent zones of equal size, $q = \frac{\#\text{ opaque zones}}{\#\text{ zones}} = 0.5$, Fourier expansion can be aplied,

$$f(x) = \sum_{m=-\infty}^{\infty} a_m \mathrm{e}^{\frac{i2\pi mx}{d}} = \sum_{m=-\infty}^{\infty} a_m \cos\left(\frac{2\pi mx}{d}\right) \tag{2.35}$$

$$\text{with } a_m = \frac{1}{d}\int_{-d/2}^{d/2} f(x)\mathrm{e}^{-2\pi imx/d}\,\mathrm{d}x = \frac{2}{d}\int_0^{d/4} \cos\left(\frac{2\pi mx}{d}\right)\mathrm{d}x = \frac{\sin(\frac{m\pi}{2})}{m\pi}. \tag{2.36}$$

The coefficients a_m are the amplitudes of the transmission, which are zero in every even diffraction order due to the sine term.
In the same way, the transmission of a zone plate can be computed. In this case, the periodicity depends on the radius of the zone plate, i.e., $\frac{r^2}{\lambda f}$ instead of $\frac{x}{d/2}$,

$$f(\frac{r^2}{\lambda f}) = \sum_{m=-\infty}^{\infty} a_m \cos\left(\frac{m\pi r^2}{\lambda f}\right) \overset{u=\frac{\pi r^2}{\lambda f}}{\rightarrow} f(u) \sum_{m=-\infty}^{\infty} a_m \cos(mu). \tag{2.37}$$

The periodical circular grating sets the limits for the a_m coefficients, since $f(u) = 1$ for $0 \leqslant u \leqslant \frac{\pi}{2}$ and 0 else, see Fig. 2.11 b, leading to the same result as the calculation of the amplitudes for the regular grating,

$$a_m = \frac{1}{2\pi}\int_{-\pi}^{\pi} f(u)\cos(mu)\,\mathrm{d}u = \frac{1}{\pi}\int_0^{\pi/2} \cos(mu)\,\mathrm{d}u = \frac{\sin(\frac{m\pi}{2})}{m\pi}. \tag{2.38}$$

Now, the transmitted intensity for the respective diffraction orders m can be obtained from Equ. (2.11).

$$I_m = |a_m|^2 I_0 \quad \Rightarrow \eta_m = \frac{I_m}{I_0} = \begin{cases} 0.25 & m = 0 \\ \frac{1}{(m\pi)^2} & m \text{ odd} \\ 0 & m \text{ even} \end{cases} . \tag{2.39}$$

That means, in the first order focal point of a zone plate, $\frac{1}{\pi^2} \simeq 10\%$ of the incident light is transmitted.
The resolution of a zone plate is determined via the numerical aperture, which is defined by

$$NA = \frac{f_n}{f} , \tag{2.40}$$

as can be seen in Fig 2.10. Firstly, the thickness of the outermost zone is calculated:

$$\begin{aligned} \Delta r_n &= r_n - r_{n-1} && (2.41) \\ \Leftrightarrow r_{n-1} &= r_n - \Delta r_n \\ \rightarrow r_{n-1}^2 &= r_n^2 - 2 r_n \Delta r_n - \Delta r_n^2 \\ &\simeq r_n^2 - 2 r_n \Delta r_n . && (2.42) \end{aligned}$$

Taking the difference of the outermost zones using the zone plate equation, Equ. (2.33), yields

$$\begin{aligned} r_n^2 - r_{n-1}^2 &= n f \lambda - (n-1) f \lambda = f \lambda && (2.43) \\ \overset{\text{Equ. (2.42)}}{\Longrightarrow} \Delta r_n &= \frac{f \lambda}{2 r_n} . && (2.44) \end{aligned}$$

With this, Equ. (2.40) reads

$$NA = \frac{\lambda}{2 \Delta r_n} . \tag{2.45}$$

Using the Rayleigh criterion, $\delta_R = 0.61 \frac{\lambda}{NA}$, the resolution limit of a zone plate is

$$\delta_R = 1.22 \Delta r_n . \tag{2.46}$$

Consequently, the highest possible resolution achieved in the first order focus of a zone plate is only determined by its geometrical properties.

2.3.2 X-Ray Microscopes

Using zone plates, it is possible to focus x-rays like visible light with refractive lenses in conventional microscopy. Two instrumentational setups exist: the transmission x-ray microscope (TXM), which work with full-field illumination, and the scanning transmission x-ray micrsocope (STXM) which work in scanning mode.
In Fig. 2.12 a sketch of a TXM is depicted. A condenser optical element (zone plate or mirror) illuminates the sample. At synchrotron facilities, TXMs do not need a monochro-

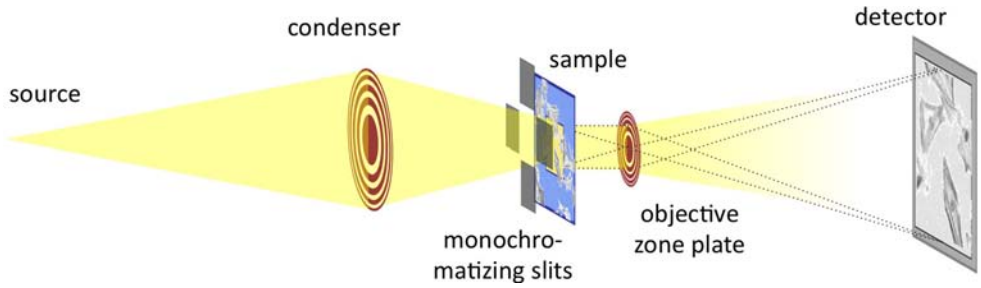

Figure 2.12: *Sketch of the principle of a full-field TXM. Further information is given in the text.*

mator, because the condenser zone plate and the slit work as monochromatizing objects. Therefore, they can also be operated at bending magnets using incoherent radiation, see section 3.2.1. For every energy a distinct focal spot exits. The condenser is positioned, such that the first order focus of the desired energy is in the sample plane. The slit blocks unwanted radiation from higher orders and a central stop (not drawn in Fig. 2.12) filters out the zeroth order. Via a micro zone plate, the sample is imaged onto the detector, usually a CCD camera (charged coupled device). The resolution depends on Δr_n, as noted in Equ. (2.46). As the sample is placed in the focal spot of the condenser, the photon flux is very high, and only short exposure times are needed. Furthermore, since the imaging zone plate is situated between sample and detector, higher spatial resolution is achieved than with a STXM.
The principle of an STXM is shown in Fig. 2.13. In contrast to the TXM, the imaging optics

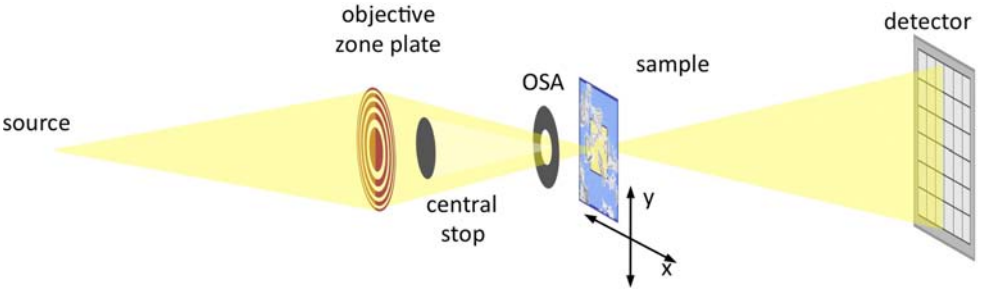

Figure 2.13: *Scheme of a STXM. The detector only detects the transmitted intensities of the focal spot, which is raster scanned over the sample.*

here is located in front of the sample. The incident radiation is focussed in first order onto the sample and the zeroth order is blocked by a central stop (not shown in Fig. 2.13). The spot size determines the resolution of the image and is, of course, also determined by Δr_n. To record an image, the focal spot is raster-scanned over the image area, which is either achieved by moving the sample stage or the zone plate. The transmitted intensity is detected, e.g., with a CCD or a photon counter. For the x-rays being focussed precisely into

one spot, the radiation needs to be coherent and monochromatic, so a STXM usually is operated at an undulator, see section 3.2.1.
The advantage of a STXM is that it can also be used as a nanoprobe. That means, a spectrum of a region of interest can be recorded by tuning the energy with the monochromator and adjusting the zone plate at one spot. Furthermore, the spectrum does not necessarily have to be an absorption spectrum, but can also be a fluorescence spectrum, if a suitable detector is placed in front of the sample. With this detector, it is also possible to record a fluorescence image of the sample. Since an image has to be scanned, it is clear that the time for image acquisition is much longer than for the full-field TXM. Due to the combination of micro zone plate and central stop in front of the sample, the radiation dose is much lower than in a TXM, usually in the range of 10 %.

3 Instrumentation

For the measurements, instrumentation both based on in-house x-ray sources and synchrotron beamlines was used. While synchrotron radiation is bright enough to be used for spectroscopy and microscopy, the target material of a plasma has to be chosen appropriately for the instrumental purpose. Plasmas producing broadband radiation are used for spectroscopy, whereas plasmas with narrow line emission are best suited for microscopy experiments. In the last years, laser driven plasma sources for soft x-radiation have been developed [59, 98, 143]. It has been demonstrated that applications such as x-ray microscopy [73] or spectroscopy [206], which were previously restricted to synchrotron experiments could be realized. Apart from plasma sources, also other table top setups operating with high harmonic generation [169, 222] or x-ray lasers [210] generate x-radiation of high brilliance.
Due to their small size, laser plasmas are attractive compact x-ray (and EUV, extreme ultraviolet) sources. In this chapter, firstly the plasma driven x-ray sources will be explained, followed by the basic principle of a synchrotron storage ring. Thereafter, the end-stations according to their applications, spectroscopy, x-ray microscopy and x-ray spectromicroscopy are presented.

3.1 Laboratory Based Instruments

3.1.1 Laser-Driven Plasmas

The in-house x-ray sources used for the experiments reported here were all driven by laser generated plasmas. The basic principle is to focus a laser beam of high intensity onto a target. Depending on the target material and the laser intensity, x-ray radiation over a wide spectral range can be produced.
The lasers used here generate ns-pulses and medium intensities of $I < 10^{15} \frac{\mathrm{W}}{\mathrm{cm}^2}$. During the laser pulse, the atoms in the target are ionized creating a plasma, either by multi-photon interaction, tunneling or field ionization, depending on the intensity I, respectively electrical field E, in the focal spot $E = \sqrt{\frac{I}{c\epsilon_0}}$, with c the speed of light and ϵ_0 the vacuum permittivity. Additionally, the plasma is heated, if the particles absorb photon energy via inelastic collisions (*inverse Bremsstrahlung*). Due to the heating process, the plasma expands rapidly resulting into a steep gradient of the electron density n_e. The laser pulse can only enter the areas with electron densities below the critical electron density n_c. If $n_e > n_c$, it is totally reflected. The critical electron density n_c is a characteristic property of

a plasma. It can be derived from the plasma frequency ω_p, which is obtained by describing the plasma as a fluid, $\omega_p = \left(\frac{e^2 n_e}{\epsilon_0 m_e}\right)^{1/2}$, with the charge and mass of an electron e and m_e:

$$n_c = \frac{\epsilon_0 m \omega_p^2}{e^2}. \tag{3.1}$$

Since a plasma is close to thermal equilibrium, most of the energy of a plasma is distributed evenly, owing to the processes in the plasma leading to an emission similar to a black-body radiation with some distinct emission lines, as illustrated in Fig. 3.1. The spectrum of a

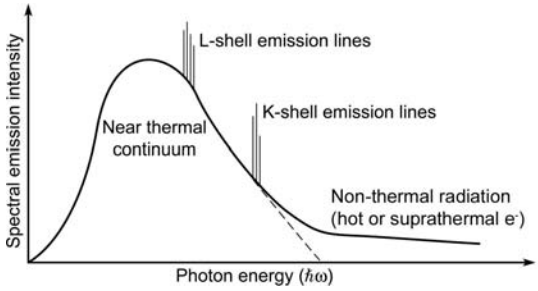

Figure 3.1: *Radiation intensity of a plasma. The continuum black body radiation originates from interactions between free electrons and ions, the line emissions are due to bound electron transitions in the atoms, adapted from Attwood [8], p.192, Fig. 6.1.*

plasma is described by three components:

Two processes generating continuous radiation (*black body radiation*):

Bremsstrahlung: electrons in the plasma radiate during deceleration or deflection.

Recombination: electrons recombine with the ionized atoms of the target material.

Line emission: electron transitions in atoms or molecules. The line emission is correlated to the intrinsic property of the plasma element and allows for measurement of its temperature and density.

For the compact laser driven instruments applied here, a Krypton (Kr) gas puff target and a methanol liquid jet target were used. The advantage of gaseous and liquid targets is that no debris can influence the quality of the target as it is constantly renewed and thus allows for a high repetition rate.

3.1.2 Spectrometer

The instrumental setup of the NEXAFS-spectrometer is described in detail by C. Peth [141, 143, 144]. A schematic of the setup is depicted in Fig. 3.2a. Kr was used as a gas puff target material, because of its broad band emission spectrum in the spectral region of the water window, shown in Fig. 3.2b.
As can be seen from Fig. 3.2b, the Kr gas emits broadband radiation, which stems from the black body radiation spectrum and densely packed spectral lines. At 2.8 nm, the emission is limited by a titanium membrane (thickness d = 200 nm, Ti $L_{II,III}$-edges at 460.2 eV and 453.8 eV) that filters out higher wavelengths. The spectrum was recorded with a pinhole

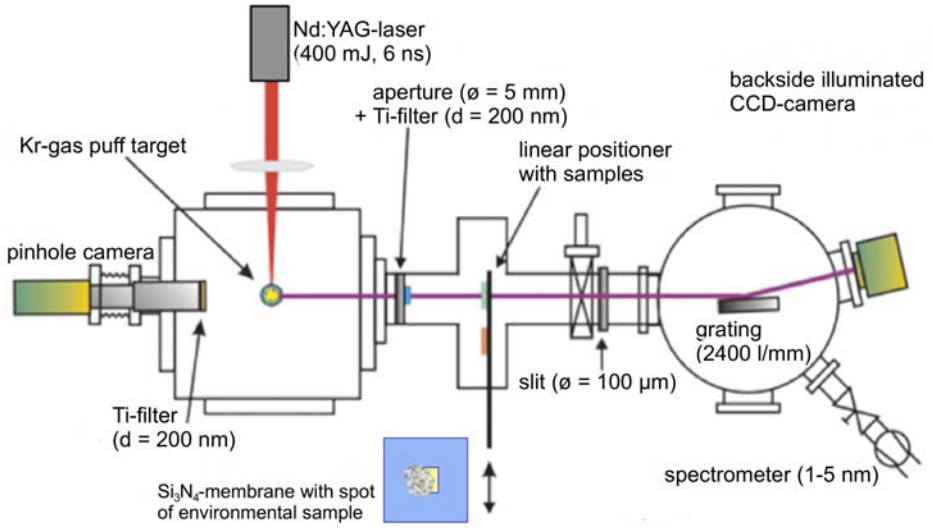

(a) *Compact laser driven plasma source spectrometer*

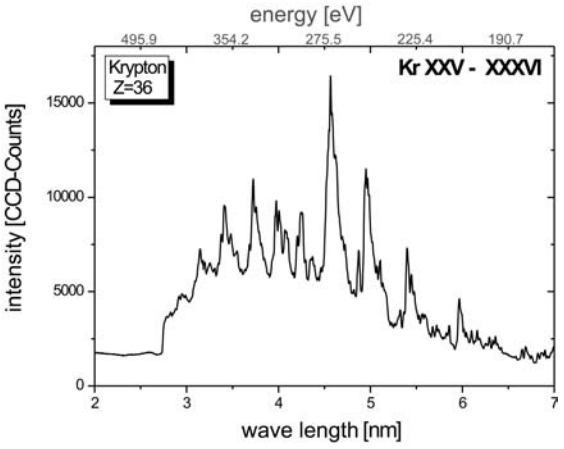

(b) *Broadband radiation of Kr gas target*

Figure 3.2: **a)** *Spectrum of the Kr gas target, which was used for the spectroscopy experiments.* **b)** *Sketch of the instrumental setup of the laser-plasma XUV source used for recording the NEXAFS-spectra. The instrument has been developed at the Laser-Laboratorium in Göttingen and is described in detail in the dissertation of C. Peth [141], from which both images are adapted (modified).*

camera by averaging over 50 pulses at a gas pressure of 25 bar with a laser pulse length of 7 ns and energy of 800 mJ.

The major components of the spectrometer (Fig. 3.2a), source, object holder and spectrometer, are flanged together. The distance between the plasma source and the sample is about 220 mm followed by a 5 mm opening between the source and the sample stage, also in vacuum. The distance between the sample and the entrance slit of the spectrometer is about 425 mm. The source is a pulsed Kr gas puff target (gas pressure 25 bar) in a vacuum chamber ($\sim 10^{-4}$ mbar), on which a Nd:YAG laser beam is focused to a diameter of ~ 60 µm (peak density $4\times10^{12}\ \frac{\mathrm{W}}{\mathrm{cm}^2}$). That way, a broadband radiation is emitted, Kr XXV-Kr XXXVI,

which also includes the spectral range of the water window, 280-530 eV. That means, the spectrum results from the emission lines of the transitions of 24- to 30-times ionized Kr located very close together energetically, covering a broad range. The gas is injected through a conical nozzle generating a supersonic gas jet of high density. To filter out unwanted visible light and scattered laser light, a titanium membrane (thickness 200 nm) is positioned between the plasma source and the sample stage. Due to this limitation of the emitted spectrum, higher order contamination is not a problem, which could be an issue at a beamline of a storage ring. The source radiates into 4π, therefore the sample is fully illuminated. However, the width of the detector of the spectrometer and the entrance slit (100 µm) limit the acceptance, thus only the transmitted intensity of a sample region of (100 µm × 2.3 mm) is detected.
Apart from the entrance slit, the XUV spectrometer consists of an aberration corrected flat-field grating (2400 $\frac{\text{lines}}{\text{mm}}$) working in reflection, and a thinned backside illuminated CCD camera (Roper Scienific, 2048 pxl × 512 pxl, pixel size 13 µm). Grating angle and distance were adjusted to the CCD such that the recorded spectra are in the range between 250 eV and 800 eV. It has been tested that the resulting spectra are independent of the position of the illuminated area on the window of the Si_3N_4-membrane, because the irradiated area is large enough to average out inhomogeneities of the sample. Therefore, only one measurement per sample was used for the analysis.
The reference signal I_0 is recorded separately, but due to the high stability of the plasma source (deviation of spectral intensities < 5 % in previous experiments [135, 141], this is not a drawback. The signal was automatically converted to optical density ($oD = -\ln \frac{I}{I_0}$) using the previously recorded I_0. Preceding each measurement the incoming signal on the CCD was checked for sufficient flux.
For spectral calibration, nitrogen served as target gas, whose spectral lines are known from literature [47]. The determined resolving power of the spectrometer is $\frac{\lambda}{\Delta\lambda} = \frac{\mathrm{E}}{\Delta\mathrm{E}} \approx 200$ at 446 eV. To achieve a high signal-to-noise ratio, more than 1000 pulses were accumulated for one measurement, with a repetition rate of 1 Hz. The photon count on the sample, which is fully illuminated as mentioned before, is 1.5×10^8 photons per pulse in the spectral bandwidth of 206 eV - 454 eV.

3.1.3 Compact Transmission X-Ray Microscope

The second instrument using a compact source was the transmission x-ray microscope (cTXM) developed by the group of Hans Hertz at the Royal Technical University (KTH) in Stockholm. The cTXM is operated with a liquid methanol jet, depicted in Fig 3.3a, together with the line emission spectrum of the methanol target (Fig 3.3b). The nomenclature is to be understood in the following way: O-He-α means, that the oxygen atom is helium-like with only two remaining electrons. The α-emission line results from the transition between L- and K-shell. C-Ly-α corresponds to the 1s - 2p transition of C VI.
The choice in target material involves a different emission spectrum; in contrast to the Kr gas target, the liquid methanol jet emits a line spectrum, which is ideally suited for x-ray microscopy. The plasma has a high spatial stability (25 µm at FWHM) [157] and a narrow spectral bandwidth of $\frac{\Delta\lambda}{\lambda} = 2 \times 10^{-3}$ at $\lambda = 3.37$ nm ($\hat{=}$ 368 eV). A detailed description of the cTXM is found in Takman et al. [191], Hertz et al. [74] and Bertilson [21]. A Nd:YAG laser

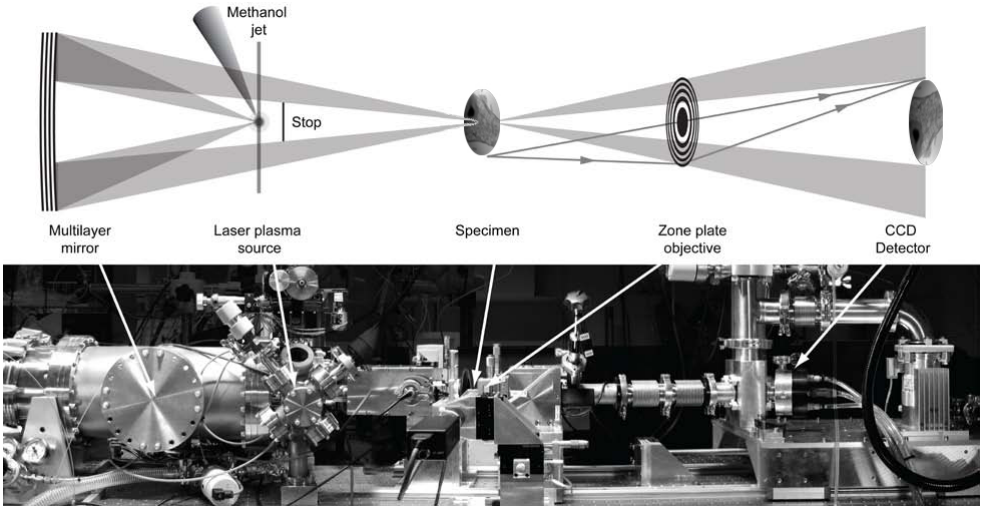

(a) *Setup of the compact TXM*

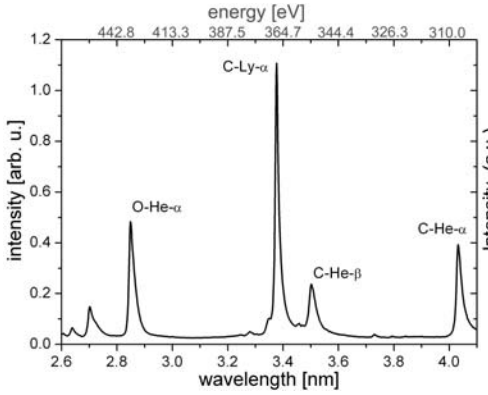

(b) *Line spectrum of the liquid methanol jet*

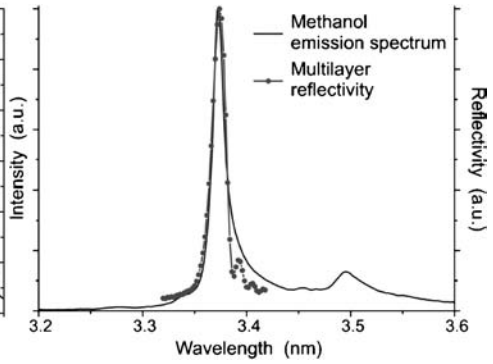

(c) *Reflectivity of the condenser mirror*

Figure 3.3: a) *Sketch and photo of the instrumental setup of the compact TXM constructed and built at the KTH in Stockholm, acquired from Hertz et al. [74], modified. More information is given in the text.* **b)** *Spectrum of the liquid methanol target, used for the cTXM, taken from Vogt et al. [206], modified.* **c)** *Reflectivity of the condensing multilayer mirror plotted together with the emission spectrum of the methanol liquid jet [184].*

(100 Hz, 3 ns) was used to generate the plasma by focussing it onto the target (focal spot size: 10 μm). This results into pulse energies of 130 mJ, corresponding to a focal intensity of $2.5 \times 10^{13} \frac{\mathrm{W}}{\mathrm{cm}^2}$. The generated x-radiation has a density of $\sim 5 \times 10^{11} \frac{\text{photons}}{\text{pulse}\cdot\text{sterad}\cdot\text{line}}$.
A Cr/Sc (chromium/scandium) multilayer mirror (3.37 nm spacing, reflectivity $R = 3.5\,\%$) images the source onto the sample, with a numerical aperture of 0.064, see Equ. (2.45). The mirror is also functioning as monochromatizing object, selecting only one line of the

methanol spectrum, see Fig. 3.3c [184]. Scattered light from the laser and other visual light are filtered out using a Ti window of 300 nm thickness. A nickel zone plate with $\Delta r_n = 25$ nm and first order efficiency of 8.5 % [22, 80] is used to image the sample on the detector. The signal is detected by a backside illuminated CCD camera (2048 pxl × 2048 pxl, pixel-size $13 \times 13\,\mathrm{nm}^2$, efficiency $\eta \sim 55\,\%$, Princeton Instruments). The field of view is a circle with a diameter of 20 µm.
Via a kinematic mount, the samples are inserted into the microscope. At the sample stage, a He atmosphere is established because of the lower absorption of x-rays in He compared to air. This allows for quick sample change and comfortable handling of wet samples. As the source is much weaker than a synchrotron, exposure times in the range of several seconds to minutes are necessary. Apart from the measurements carried out in the course of this work, this instrument can also be used for stereo microscopic and tomographic experiments [21, 67].

3.2 Synchrotron Radiation Experiments

3.2.1 Synchrotron Radiation

Experiments requiring high brilliance x-ray radiation of high flux are conducted at synchrotron radiation facilities. A short summary of the generation of synchrotron radiation is given here, based on the books of Attwood [8], Khan [104] and Bunker [36].
In a synchrotron, x-radiation is generated by accelerated charged particles, in the following the outline will restrict to electrons. By a booster synchrotron the electrons are accelerated to a distinct energy, afterwards these are inserted into a storage ring, where they are held on a circular, or more detailed a closed polygon, path. The speed $\mathbf{v}$ of the electrons is close to light speed c. The emitted radiation of these relativistic electrons is confined into a small cone and tilted forwards due to light dilatation and length contraction. The acceleration of the electrons occurs, when their path is bent, achieved by magnetic insertion devices.
The simplest form of these devices is a bending magnet (BM). A BM usually consists of a dipole magnet. An electron with charge e and mass m in a magnetic field $\mathbf{B}$ is deflected into a circular path, due to the Lorentz force

$$\gamma m \frac{\mathrm{d}\mathbf{v}}{\mathrm{d}t} = -e\mathbf{v} \times \mathbf{B}, \tag{3.2}$$

with the Lorentz factor $\gamma = \frac{c}{\sqrt{c^2 - v^2}} = \frac{1}{\sqrt{1-\beta^2}} = \frac{E_e}{mc^2}$ ($\beta = \frac{v}{c}$, E_e the energy of the electron). For a storage ring, γ is of the order of several thousands, and $\mathbf{B} \sim 1$ T. The Larmor formula gives the power P of the radiation emitted by an electron deflected by a BM:

$$P = \frac{\mu_0 e^2 \gamma^6}{6\pi c} \left(\mathbf{a}^2 - \left| \frac{\mathbf{v} \times \mathbf{a}}{c} \right|^2 \right), \tag{3.3}$$

with μ_0 the magnetic susceptibility of free space and acceleration $\mathbf{a}$ of the electron. The radiation cone has an angular width of $\theta \simeq \frac{1}{2\gamma}$ using small angle approximation. An important parameter for characterizing BM radiation is the critical photon energy E_c,

which only depends on the electron energy and the applied magnetic field (with m the electron mass),

$$E_c = \frac{3e\hbar B\gamma^2}{2m} \overset{E_c \text{ in keV}}{=} 0.665 \cdot E_e^2[\text{GeV}]\, B[\text{T}]\,. \tag{3.4}$$

For E_c half of the emitted energy is radiated with higher energy photons, the other half with photons of lower energy. The spectral brightness of a BM is shown in Fig. 3.4.

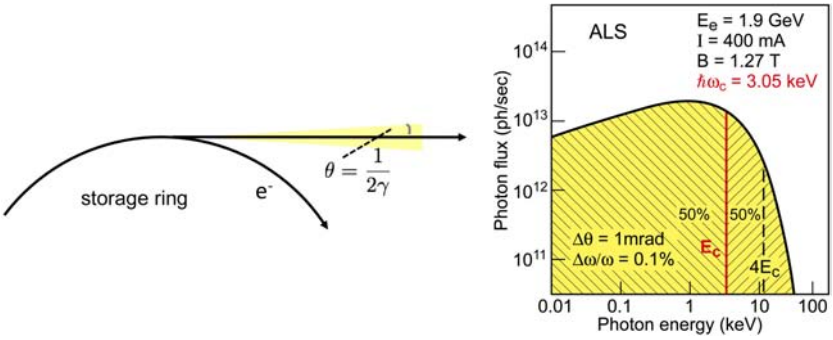

Figure 3.4: *Radiation cone, and spectral brightness generated by a BM versus the photon energy; the critical energy is indicated, too. Exemplarily, the parameters of a BM of the Advanced Light Source (ALS) in Berkeley, USA, are shown (image on the right adapted from Attwood [9]).*

In the straight sections of a storage ring between the BMs, insertion devices (ID), either undulators or wigglers are installed. These consist of alternating magnetic devices, with period λ_u, that cause an oscillation in the path of the electron, see Fig. 3.5. Changing the

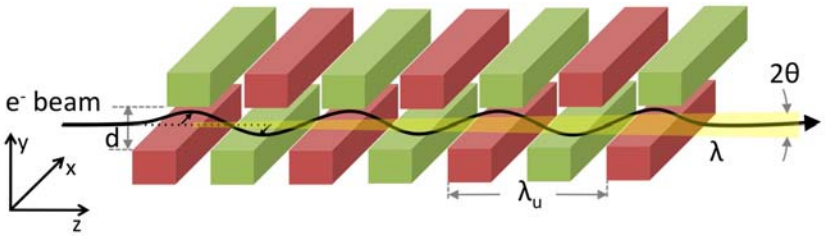

Figure 3.5: *Sketch of the basic principle of undulators and wigglers. The periodic magnetic field forces the electron beam on an oscillatory path. By changing the gap width d, the magnetic field B is changed, too.*

gap d between the magnets changes the strength of the magnetic field, because $d \propto \frac{1}{B}$. The emitted radiation is highly collimated in a narrow angular cone with $\theta \simeq \frac{1}{\gamma\sqrt{N}}$. Due to constructive interference of the radiated photons, the amplitude of the emitted wave is N times the amplitude of one undulation. Thus, the gain in intensity is N^2-times the

intensity of a single magentic dipole.
The principle of undulators and wigglers is the same, but they are operated differently. The deflection parameter K is important to describe the radiation emitted by an ID:

$$K = \frac{eB\lambda_u}{2\pi mc} = 0.9337 \cdot B[\mathrm{T}]\,\lambda_u[\mathrm{cm}]\,. \tag{3.5}$$

The smaller the gap d (Fig. 3.5) is chosen, the stronger is the resulting magnetic field B and the more the electrons deviate.
In the frame of the relativistic electron beam, the period of the ID becomes $\lambda'_p = \frac{\lambda_p}{\gamma}$. Transferring to the lab frame and taking Doppler shift into account yields the wavelength and energy of the radiation emitted by the ID:

$$\lambda_{ID} = \frac{1}{n}\frac{\lambda_u}{2\gamma^2}\left(1 + \frac{K^2}{2} + \gamma^2\theta^2\right) \quad \text{and} \quad E_{ID} = n\frac{2\gamma^2}{\lambda_u}\frac{hc}{1+\frac{K^2}{2}+\gamma^2\theta^2}\,, \tag{3.6}$$

where n is the order of the radiation.
For undulators, K is chosen to be $\simeq 1$, leading to $\lambda_{ID} \approx \frac{\lambda_u}{\gamma^2}$ and $E_{ID} \approx \frac{2hc\gamma^2}{\lambda_u}$. This means that the emitted radiation is confined into a peak of typically about 100 eV width. To span a larger spectral width, higher orders (harmonics) of the radiation are used. Additionally, the peak can be broadened by tapering the undulator, i.e., to setting different gap sizes at the two ends.

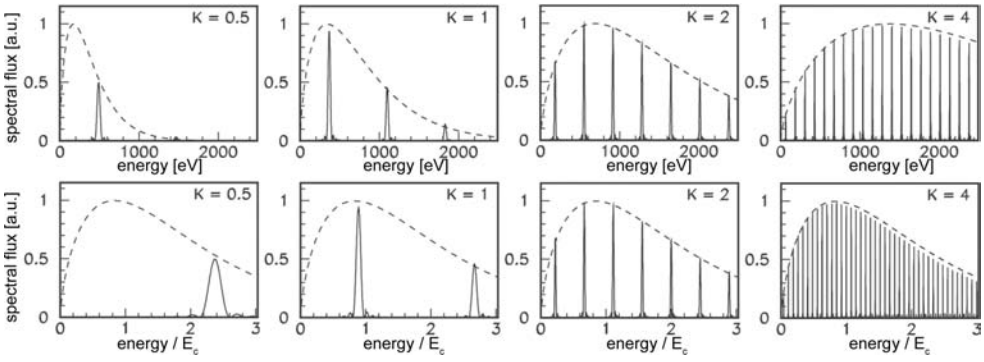

Figure 3.6: *Photon flux of an undulator versus the photon energy (upper row) and normalized by the critical energy (lower row). The transition from undulator to wiggler is established by increasing the deflection parameter K, adapted from Khan [104], Fig. 9.*

In contrast to undulators, the deflection in wigglers is quite large with $K \gg 1$. This results in broader higher harmonics, which eventually merge. The emitted radiation is similar to BM radiation, but the advantage of a wiggler is that it has a $2N$ times higher intensity. Additionally, the radiation of a wiggler can be circularly polarized. In Fig. 3.6, the spectral brightness of undulator and wiggler radiation is depicted and the transition of undulator to

wiggler radiation depending on the deflection parameter K is illustrated. As the principle is the same, the radiated power of one electron traversing an undulator and a wiggler is

$$P = \frac{\pi e^2 \gamma^2 c K^2}{3\epsilon_0 \lambda_u^2}, \tag{3.7}$$

summing over all harmonics. Thus, for a given beam current the radiated power of a wiggler and an undulator is the same, but the spectral distribution and size of central cone is different. In practical units, the total power for a given beam of current I with N undulator periods is

$$P_{total}[\mathrm{W}] = 7.26 \frac{E^2[\mathrm{GeV}^2]\, I[\mathrm{A}]\, K^2 N}{\lambda_u^2[\mathrm{cm}^2]}. \tag{3.8}$$

3.2.2 Scanning Transmission X-Ray Microscopes (STXM)

3.2.2.1 The STXM at BESSY II

In Fig. 3.7, a photo of this STXM with retracted detector vessel is shown. The beamline (1), sample stage (2), position of the zone plate (3), VLM (4) and detector vessel (5) are indicated.

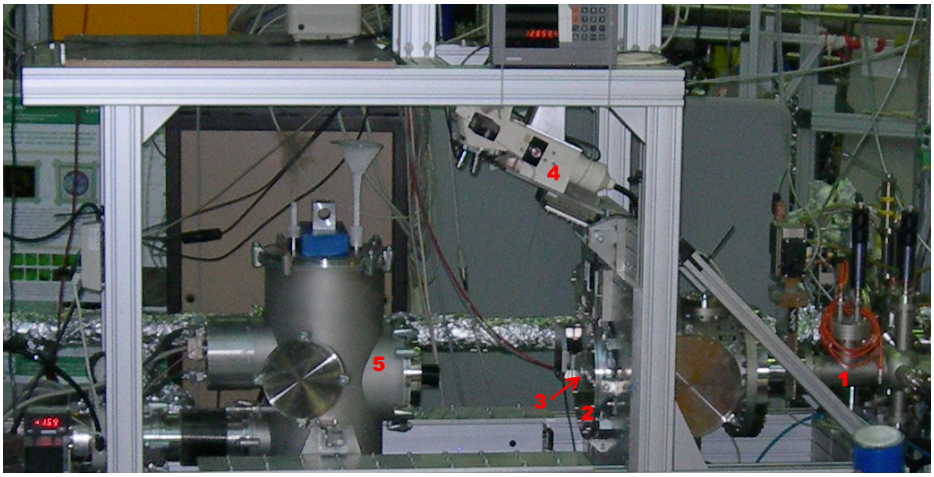

Figure 3.7: *Photo of the STXM at BESSY II. The beam (1) enters from the right. The sample stage (2) and the zone plate position (3) are indicated. In the actual position, the VLM (4) is pulled up and the detector vessel (5) is retracted for sample change.*

The setup of this STXM is described in detail in Wiesemann [211] and Wiesemann et al. [213], a sketch is depicted in Fig. 3.8.
The STXM is operated at beamline 13.2 at BESSY II, which uses a U41 undulator (λ_u = 41mm, $N = 81$). BESSY II is a 1.7 GeV storage ring and K is tunable in the range $0.5 - 2.58$, giving E_{ID} in the range 154 eV - 589 eV (Equ. (3.6)) for the first harmonic, which spans the

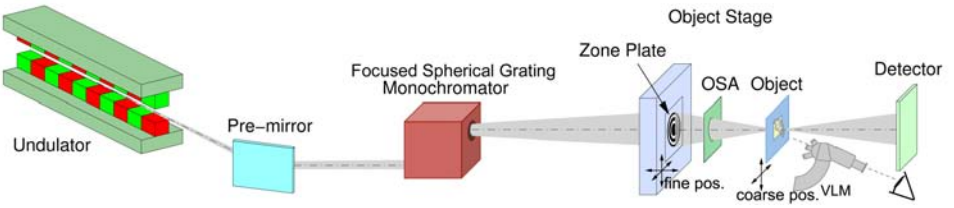

(a) *Schematic setup of the STXM at BESSY II*

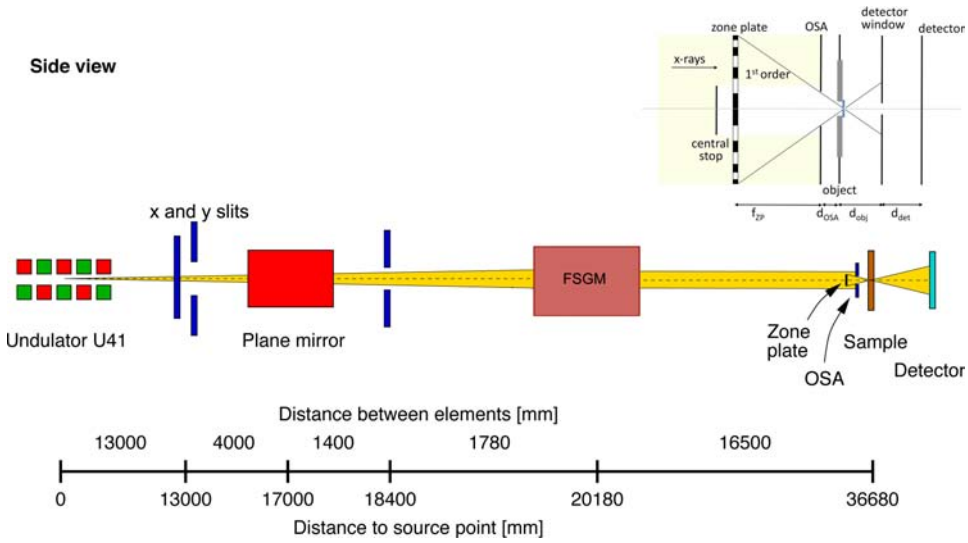

(b) *Diagram with distances with inset of the microscope optics (not to scale)*

Figure 3.8: a) *Schematic view of the STXM setup, adapted from Wiesemann [211], p.22 (modified), and* **b)** *diagram with distances at the U41-monochromator beamline at BESSY II, adapted from Wiesemann [211], p.47, the schematic inset shows the relevant distances; more details are found in the text.*

whole range of the water window, see Fig. 2.3.
The focused spherical grating monochromator (FSGM) [71] is used for reduction of the radiation bandwidth and for a coherent illumination of the micro-zone plate.
Coherent illumination is essential for the zone plate to create the desired diffraction limited small spot. The highest achievable resolution, i.e., the smallest size object Δl that can be imaged, depends on the smallest zone width Δr_N of the zone plate, $\Delta l = 1.22\,\Delta r_N$ ($\Delta r_N = 50$ nm with a number of zones $N = 1000$ at the STXM). The zone plate, is moved by a piezo scanning device in x and y direction across the sample, threby fine positioning the x-ray spot with an accuracy of a few nanometers across the object. In the direction of the beam, the zone plate is moved to achieve a focal spot on the sample. For 283 eV, $f_{ZP} = 2.283$ mm, see inset in Fig. 3.8b. The diameter of the OSA is 80 µm, the distance between OSA and the object d_{OSA} position is 600 µm. The maximum area that can be

raster-scanned by the piezo is $90 \times 90\,\mu m^2$. The gap between the detector window and the object plane was set to $d_{obj} = 1.6\,mm$ for the experiments.
The object can be positioned coarsely by using stepper motors, covering an area of several mm^2. The pixel size determines the magnification, while the field of view depends on the number of pixels. To choose beforehand regions of interest, a visible light microscope is used.
A pn-CCD camera behind the object acts as a configured detector. It is cooled manually by filling the detector vessel with liquid nitrogen. The detector records the transmitted intensity of the incident beam passing through the specimen. Sample mounting is done by retracting the detector vessel. To obtain spectromicroscopic data of the samples, stacks of images were recorded by tuning the energy monochromator around the C K-edge (280 eV - 300 eV), with a stepsize of 0.2 eV. Being a chromatic element, the zone plate was repositioned for every energy step. The dwell time for the images was in the range of 2 ms -12 ms.
The STXM is controlled by two computers: one for running the positioning, i.e., piezo stage, stepper motors, and zone plate, and recording images and spectra; the second one for reading out the pn-CCD, moving the detector vessel and the VLM. The control software runs on RT-Linux.

3.2.2.2 The X1-A1 Microscope at the NSLS

Apart from the STXM at BESSY II, also the STXM at beamline X1-A1 at the NSLS (National Synchrotron Light Source (Brookhaven National Lab, Stony Brook, USA) was used for the experiments, the beam energy is 2.8 GeV. For the X1-A1, detailed information is found in the literature [93, 94, 189] and references therein.
A schematic overview of the X1-A beamline is shown in Fig. 3.9. The names *outboard* and *inboard* refer to the branches of X1-A that has been employed for the microscope. The experiments reported here were carried out with the outboard STXM.
The undulator ($\lambda_u = 8.0\,cm$, 35 periods [149]) to which the beamline is connected, emits between 228 eV and 893 eV ($0.17 < K < 2.47$) providing suitable conditions for soft x-ray microscopy. A grating monochromator (SGM) is used to adjust the beam to the right energy and coherent radiation. The zone plate has an outer zone width of $\Delta r = 30\,nm$ and is fixed in x- and y-direction. Only for focussing the spot on the sample, it is moved in z-direction. Sample positioning and scanning is performed solely at the sample stage. Stepper motors are used for coarse positioning and on-the-fly scans with a travel range of $25 \times 25\,mm^2$ at a minimum step size of about 100 nm. Fine positioning for high resolution imaging is controlled by a piezo system, with a maximum range of $100 \times 100\,\mu m^2$ and a resolution of 1 nm. Conveniently, the sample stage of this microscope has an automatic positioning system using laser interferometry that also corrects eventual drifts during the recording of image stacks [117].
The sample is not in vacuum and for better results a helium environment can be established. The dwell times for the experiments performed at the X1-A1 was 1 ms.

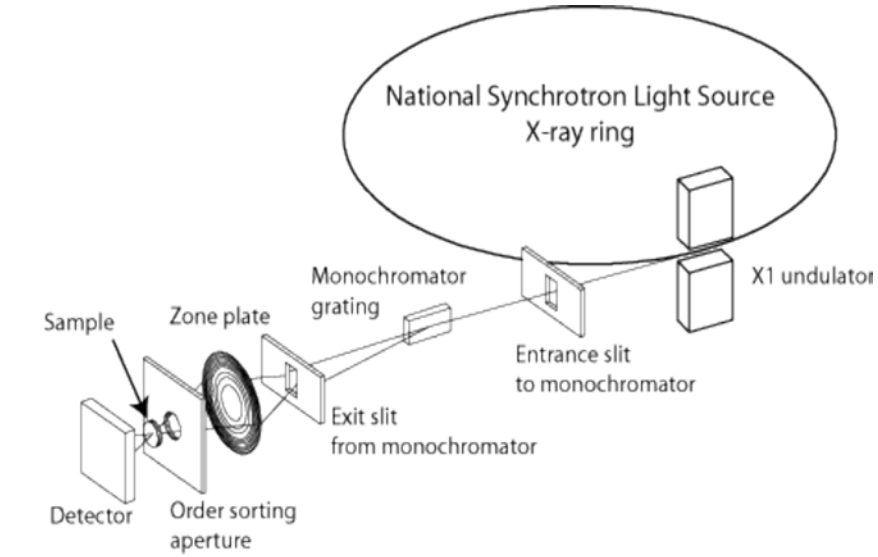

(a) *Schematic*

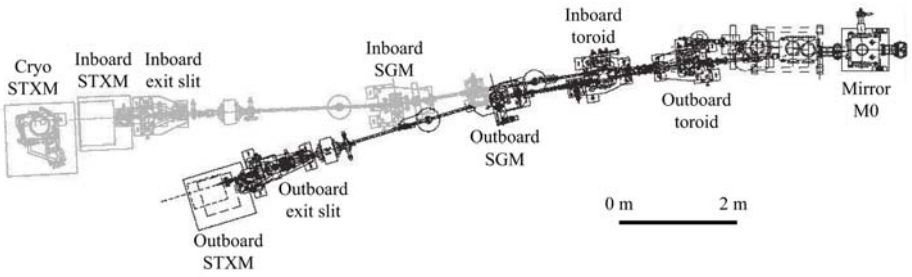

(b) *Scaled diagram*

Figure 3.9: a) *Schematic view of the X1-A1 microscope at the NSLS, adapted from SUNY and NSLS [189].* **b)** *Scaled diagram of the X1-A beamline, adapted from Winn et al. [215] (modified), the experiments were carried out at the outboard STXM. More details are found in the text.*

4 Natural Organic Matter (NOM)

4.1 Introduction

Humic substances (HS) make up a major part of the natural organic matter (NOM). They are found not only in soils, but also in water, e.g., rivers, lakes, oceans and their corresponding sediments, and organic deposits, e.g., peat, brown coals and shale [63]. These refractory organic substances (ROS) originate from biodegradation of plant remnants by microbes and bacteria. Thus, HS are large amorphous compounds of organic polymers of high molecular weights [55, 183] - either described as huge molecules [103] or as supramolecular associations of functional groups [190].
The term *humic substances* implies three subgroups: fulvic acids (FAs), humic acids (HAs), and humins. In a first approach, their classification scheme depends on the color of the substance and the solubility at different pH-values. HAs have a dark brown color and are only soluble at low pH values, usually < 3. FAs have a light brown color and are soluble at all pH-values. Humins, almost black, are insoluble and also the least characterized fraction [183]. HAs and FAs are usually extracted from soils using extraction procedures described by the International Humic Substances Society (IHSS).
In general, FAs contain more functional groups, e.g., carboxylic, carbonylic, hydroxylic or phenolic groups. HAs have a more aromatic character and an H/C ratio that is about 1.5 times smaller. They are also more reactive than FAs. A difference must also be made between the HS of aquatic and terrestrial origin. Aquatic especially marine HS show a more aliphatic character and the particle sizes are much smaller [60, 106].
Due to their size, their many functional groups and their ubiquity, HS belong to the most important organic substances in soils. They provide nutrition for plants and microbes, not only as source for carbon, but also by mineralizing sulfur, nitrogen and phosphor [54]. HS contribute to the fertility of soils, since they are able to form chelate complexes with single- or multi-valent cations like metal ions [18, 60]. They thus play a major role in transport processes, for instance for molecules that would otherwise be immobilized, thereby influencing their bioavailability. Apart from that, HS also help to detoxify soils by binding, e.g., aluminum or arsenic, and inhibiting their reactivity. HS are redox-reactive and support the cationic exchange of soils [200]. Furthermore, HS have an impact on the hydrologic balance in many environmental compounds.
In ecosystems, HS hence have fundamental functions. The heterogeneous nature of HS makes it difficult to exactly characterize them structurally; however, it is of key importance to find reliable ways to measure their attributes. NEXAFS spectroscopy

has been established as a useful tool for the characterization of chemical compounds [28, 43, 54, 116, 164, 174, 187, 204]. Such spectroscopic investigations are most often carried out at synchrotron facilities. Due to the high amount of information obtainable by such experiments, a high demand exits for measuring time at these set-ups. Sometimes this may lead to rather long waiting times before the measurements can be performed.
To elucidate, if the samples under investigation are suited for NEXAFS, it would be desirable, if a set-up existed that would allow preliminary measurements. That way, appropriate sample preparation techniques, the sample holder equipment, and the sample storage could be tested or improved. This approach would drastically reduce the amount of time required at the storage rings leading to a much higher sample throughput and thus to a reduction of waiting time.
Apart from potential improvements of the preparation of synchrotron experiments, a table top spectrometer could have other possible fields of application. If such an instrument was for instance incorporated into a soil science laboratory, kinetic measurements would be feasible. Experiments investigating the interactions of model compounds like distinct proteins [137], leaching experiments, or the change of extracted substances depending on extraction time or solvent would be realizable within a short measuring time. With an instrument in the home institution, experiments would be quickly repeatable adding to statistical context, too, which is important, e.g., to test heterogeneity in the field.
Spectrometers operating with laser plasmas are attractive due to their small size, high spatial stability and high brightness and/or high flux. In this chapter, the application of a table top instrument built by C. Peth [141] to study environmental samples is shown. In previous experiments with this instrument, polymers were studied and the outcome was related to synchrotron measurements [135]. Here, the ability of the compact NEXAFS spectrometer to characterize different heterogeneous samples is demonstrated [166]. In the course of this, an empirical analysis to quantitatively assess such complex heterogeneous systems like HS was developed. A second experiment shows the influence of different extraction techniques on a HA.

4.2 Spectroscopic Measurements of Different Fractions of NOM

At first, NEXAFS was used to characterize small, well-known molecules [62, 92, 187] and their orientation and bond lengths. Soon, more complex samples from polymer science were subject to NEXAFS studies [2, 105, 204]. Over the recent years more and more complex heterogeneous samples from biomolecular [20, 26, 77, 102] or environmental [31, 43, 44, 129, 174] origin were investigated. Especially natural organic matter and soils [164, 179] or particulate matter, fine dust particles originating from combustion [29, 182], were subject to such studies. Among other, valuable information about the chemical composition, functional groups, and also their change due to photolysis or temperature could be gained.

4.2.1 Reference Data and Analysis Approach

In this section, the analysis method shall be explained exemplarily using the spectra of a polyimide foil (PI) and a commercially available HA (Sigma Aldrich). This approach is then used to characterize four different environmental samples.

4.2.1.1 Analysis of the Spectra

The data was directly transformed into optical density using $oD = \ln\left(\frac{I_0}{I}\right)$ and the signal of the Si_3N_4-membrane was subtracted. For demonstration, the raw data and the calculated oD for the reference humic acid, see section 4.2.1.3, are displayed in Fig. 4.1.

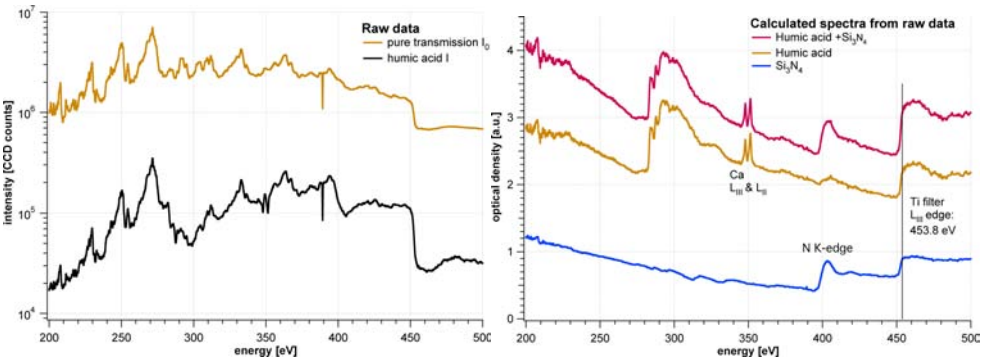

(a) *Raw data of humic acid* **(b)** *Calculated optical densities*

Figure 4.1: a) *Measured intensities with and without a sample, here the reference humic acid.* **b)** *Calculated spectra directly from the raw data and corrected for the signal of the Si_3N_4-membrane.*

Before fitting, the spectra were smoothed using a standard algorithm (Golay-Sawitzki). A linear pre-edge background was subtracted from each spectrum, representing the decay, usually observed in x-ray absorption spectra [187] and defining the zero line. Because in the analysis solely the relations of the peaks within one spectrum are regarded, renormalization was done by setting the highest point to 1, facilitating the qualitative comparison between the spectra. The analysis of the NEXAFS spectra was carried out using SpecFit, an IDL-program (Interactive Data Language) developed within the group of J. Thieme [66].
To find a fit for the spectrum of a heterogeneous sample of mainly unknown chemical composition, two different approaches were combined.
First, the positions of the peaks within one spectrum were exactly localized from the minima of the second derivative of the spectrum, with respect to the energy, as is shown in Fig. 4.2c for the PI and in Fig. 4.4c for the HA. This procedure was chosen, because the second derivative is more sensitive to changes in the spectrum than determining zero crossings from the first derivative. Second, advantage was taken of the fact that published NEXAFS-spectra of many chemical compounds from polymer research, biomolecular, and environmental sciences already exist [30, 46, 50, 76, 77, 91, 92, 105, 123, 172, 176, 178, 179]. The spectra were compared to the positions gained from the derivatives and allocated to the expected peaks from transitions to unoccupied orbitals such as $\sigma^*_{\text{C-N}}$, $\sigma^*_{\text{C-S}}$ or phenolic $\pi^*_{\text{C=C}}$. These peaks were not noticeable from the spectrum or its derivatives in the first place, but could be found via the most probable positions from the literature [29, 31, 46, 50, 76, 102, 159] as starting points for the fitting algorithm, as is depicted in the plots of the reference data shown below.

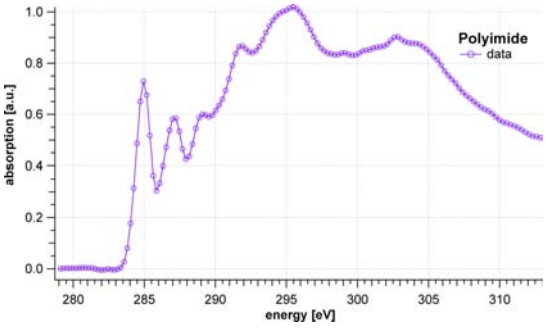

(a) *PI spectrum*

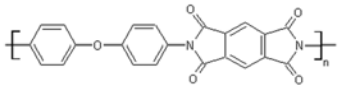

(b) *Structural formula*

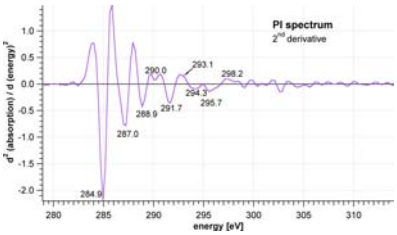

(c) *Second derivative*

Figure 4.2: a) *Spectrum of the PI foil at the C K-edge,* **b)** *the structural formula, and* **c)** *the second derivative of the spectrum.*

Because of their asymmetrical shape, the peaks cannot be fitted exactly with a Gaussian curve [50]. Often, NEXAFS spectra are fitted using Gaussian curves for the peaks and an arc tangent function to simulate the absorption edge. As seen from NEXAFS spectra of small well-understood molecules [10, 46, 91, 92], shifts of peak positions and absorption edges occur, depending on, e.g., the chemical environment, the substrate or the state of aggregation. Furthermore, the functional groups and other subgroups in such large compositions are regarded as independent units. Each of these units has its ionization point at another energy, as known from the literature [62, 91, 92, 170, 187]. Thus, due to a mix of chemistries leading to chemical shifts of the core level, the arc tangent for large and complex molecules like environmental samples would be very broad, thereby dominating the fit of the spectra and submerging the Gaussian curves, cf. Fig. 4.3 (arrows). In addition, it is not trivial to determine the exact location of the arc tangent [187]. To account for this and for the asymmetry of the peaks, a combination of Gaussian, Lorentzian and arc tangent curve for every resonance was used.

Handling the complexity of the sampled data, constraining assumptions had to be made concerning the parameters of the three curves that were assigned to every peak in order to achieve consistent results. The ratio of the Gaussian to the Lorentzian curve was set to 0.6; the latter accounts for the widening of the peaks originating from intrinsic properties of the instrument. The width of the arc tangent was set to 0.8 eV. The values of the two parameters, the ratio and the arc tangent width were determined from the best fit. The relative height of the arc tangent was set to be 0.1, which was estimated via the ratio of attenuation lengths of polymers at 280 eV and 300 eV [48].

For the estimation of the elemental compositions derived from the peak assignments, the following assumptions were made. From the C 1s orbital, an electron is excited to a higher unoccupied molecular orbital, to the continuum or to an atomic orbital within the C atom. After the excitation, the atom relaxes into its original state, until it is again excited by another photon. That way, the bonding environment is probed resulting into

the characteristic peaks in the spectra. The heights and widths of these resonance peaks are proportional to the number of transitions in the sample and therefore allow an approximation of elemental composition of the sample. A similar approach works for NEXAFS spectra of sulfur and has also been applied to XPS (x-ray photoelectron spectroscopy) data [32]. For the analysis, it was hence assumed that the area under a Gaussian curve assigned to a resonance is proportional to the frequency of occurrence of this binding form of the studied element [44, 85, 182, 216]. This made it possible to approximate the composition of the covalently bound elements.
To do so, the areas of the peaks were added up and the sum was set to 100 % in the sample. For the PI and the HA, these values are collated in Tab. 4.1 and 4.3. By summing up the respective percentages of the transitions to the single (σ^*) and double (π^*) bond orbitals of the same kind, an estimate of the elemental composition in the organic part of the studied sample was achieved. Peaks, which were assigned to more than one transition, were counted in equal parts to the relative component, e.g., of the area under the PI peak at 287.36 eV ($1s \rightarrow \sigma^*_{\text{C-H}}$, 3s), 50 % was added to the amount of C, 50 % to the amount of H. Since the spectral features not only comprise of contributions of the transitions noted in the second column in Tab. 4.2 or 4.4, only the most probable transitions, according to literature are used for assigning the peaks. The values for the elemental compositions should thus be considered as maximum content. In particular, the amounts of N and S are affected, since they are estimated from the assigned $\sigma^*_{\text{C-N}}$ and $\sigma^*_{\text{C-S}}$ resonances. In detail,

$$p(\text{X}) = \sum p_1 \left(1s \rightarrow \pi^*_{\text{C=X}}\right) + \sum p_2 \left(1s \rightarrow \sigma^*_{\text{C-X}}\right) + \left[\sum p_3 \left(1s \rightarrow \text{AO}\right)\right]_{\text{C}}, \tag{4.1}$$

where p(X) is the resulting proportion of component X, e.g., Tab. 4.1 and $p_{1,2,3}$ is the respective percentaged amount of the areas under the assigned peaks, as listed in the last column in Tab. 4.2; AO refers to atomic orbital.
For the calculations, the peaks of the potassium $L_{\text{II,III}}$-edges have not been taken into account. At energies above 300 eV, the transitions to $\sigma^*_{\text{C=C}}$ and $\sigma^*_{\text{C=O}}$ are located. However, the contribution of the double bound compounds has already been accounted for from the π^* orbitals, thus, they were left out of the estimation, too.
Often, NEXAFS spectra are evaluated by fitting the peaks with Gaussian (and Lorentzian) curves and using one broad global arc tangent function for the absorption edge [50, 85, 123]. To demonstrate the advantage of the present approach, this procedure was used to evaluate the PI foil. The comparison of the results (see Tab. 4.1) shows that the estimation of the elemental composition is less accurate. This is mainly due to the resonances around 290 eV now being significantly smaller (arrows at 1s→ $\sigma^*_{\text{C-N}}$ and $\sigma^*_{\text{C-C}}$ in Fig. 4.3).

4.2.1.2 Polyimide

Polyimides are synthetic polymers, consisting of well-defined building blocks. The main constituent, the imide group, is part of every PI, but the moieties of the different PIs vary. As pointed out in e.g., [26, 187], the NEXAFS spectra of chains do not differ a lot from the spectra of their building blocks. The PI used here was PMDA/ODA, PI 2545 from HD Microsystems with a thickness of 200 nm, depicted in Fig. 4.2b. Due to the well-defined

structure, the elemental composition could be calculated, using

$$p(\mathrm{X}) = \frac{A_\mathrm{X}}{\sum_x A_x}, \tag{4.2}$$

with the atomic weight A_x. The result is shown in Tab. 4.1 at the end of the section. The recorded spectrum of the PI foil used here, is quite well comparable to NEXAFS spectra of other PIs [105, 159, 188] recorded with synchrotron radiation. The very prominent resonances of the aromatic rings at 284.9 eV (benzene) and 286.9 eV (phenol), the peak of the carboxyl group (288.9 eV) and the peaks of the transition to the σ*-orbitals around 292 eV and 295 eV are characteristic for these polymers.

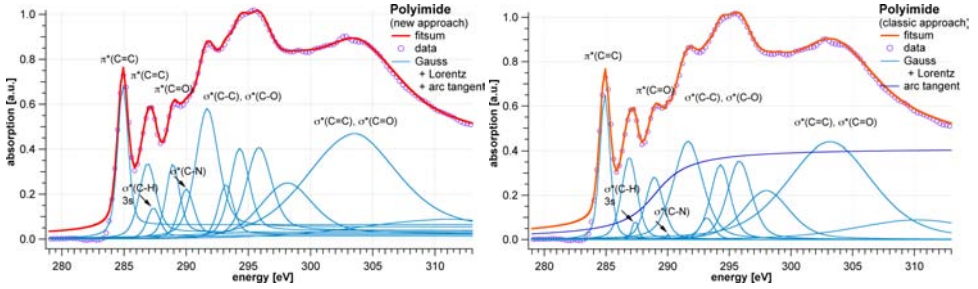

(a) *New analysis approach* **(b)** *'Classic' approach*

Figure 4.3: *Spectrum of the PI foil at the C K-edge:* **a)** *with evaluation curves as used for the experiments presented here,* **b)** *fitted assuming one global absorption edge. The assignment of the peaks with increasing energy results from comparison with published results and the differentiation of the measured data, and is presented in Tab. 4.2.*

The analysis of the spectrum is illustrated in Fig. 4.3. Here, both approaches are shown; the *new* one with an absorption edge for every peak (Fig. 4.3a), assuming a valence band for every orbital, and the *classic* approach with one broad absorption edge (Fig. 4.3b). The peak assignments and the corresponding areas under the Gaussian curves of Fig. 4.3a are presented in Tab. 4.2.

Table 4.1: *Elemental composition of the analyzed reference sample PI foil, shown in Fig. 4.3.*

sample	method		composition [%]			
			C	H	O	N
PI foil	calculated		69.1	2.6	20.9	7.3
	NEXAFS + SpecFit	see Fig. 4.3a	67.3	1.3	26.8	4.7
		see Fig. 4.3b	70.3	0.5	29.1	0.2

Using the empirical Equ. (4.1), the elemental composition was obtained for both curve

assignment approaches. For the values gained from the evaluation with SpecFit from the NEXAFS data, the percentages in elemental composition were calculated by setting the sum of the five main contributors to 100 %. Comparison with the elemental composition computed with Equ. (4.2), shows that the assignment of several small absorption edges yields better results than the approach with one absorption edge.

Table 4.2: *Energy positions and assignments of features in the C 1s NEXAFS spectrum of PI in Fig. 4.3a. The last two features have not been taken into account to calculate the elemental composition, shown in Tab. 4.1.*

sample	position [eV]	1s → (orbital)	main character	area under Gauss [%]
	284.9	$\pi^*_{C=C}$	aromatic	10.2
	286.9	$\pi^*_{C=C}$	phenolic	8.0
	287.4	σ^*_{C-H}, 3s	carbohydrates	2.5
	288.9	$\pi^*_{C=O}$	carbonyl, carboxyl	6.4
PI foil	290.0	σ^*_{C-N}	imide	4.7
	291.7	σ^*_{C-C}	aromatic	18.6
	293.2	σ^*_{C-C}		5.1
	294.3	σ^*_{C-O}	carbonyl , carboxyl	11.1
	295.8	σ^*_{C-C}, 4p		14.8
	298.0	σ^*_{C-O}, σ^*_{C-C}		18.6
	303.2	$\sigma^*_{C=C}$		
	310.3	$\sigma^*_{C=C}$, $\sigma^*_{C=O}$		

4.2.1.3 Reference Humic Acid

The information gained from the PI spectrum was helpful to characterize the second reference sample, a well investigated HA [125, 146, 155, 173], a widely used standard sample, purchased from Sigma Aldrich. The spectrum is displayed in Fig. 4.4a, with the assignments of the peaks depicted in more detail together with a suggestion for the structural formula of a HA in Fig. 4.4b. The relation of the peak heights within the spectrum is characteristic for this sample, as the comparison with HA in the following paragraph and from literature [178, 179] demonstrates. The inset shows the second derivative of the absorption spectrum with respect to the energy.
The minima of the derivative were used to determine the locations of most of the peaks in the spectrum of the HA, as mentioned before. The results, i.e., the estimation of the elemental composition (Tab. 4.3) of the analysis of the spectrum and the assignment of the peaks is shown in Tab. 4.4. As mentioned before, the resonances of the K $L_{II,III}$-edges and the $\sigma^*_{C=C,O}$ were not taken into account. Here, and also in Tab. 4.6, the energies of the peaks of the K $L_{II,III}$-edges differ from the values for the absorption edges tabulated in textbooks. This is due to the potassium being bound which results into chemical shifts of the energy of the absorption edges and is observed in other studies, too [164, 165].

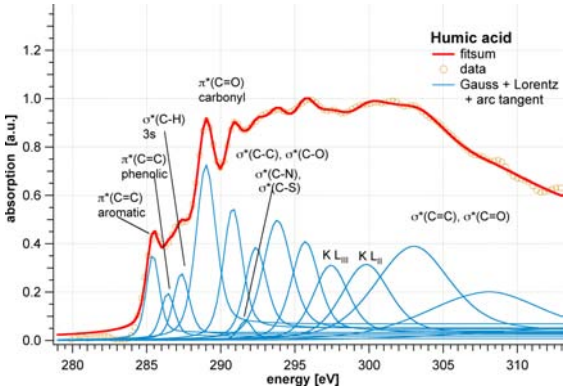

(a) *Reference HA*

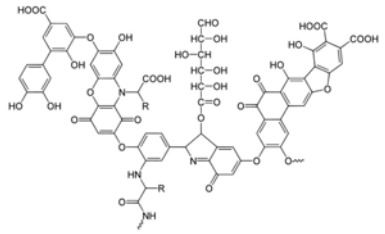

(b) *Structural formula*

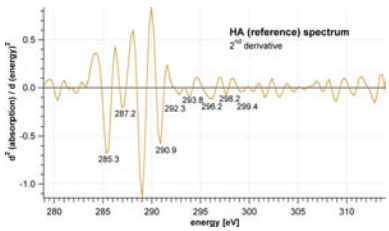

(c) *Second derivative*

Figure 4.4: a) *Spectrum of the reference HA at the C K-edge, the potassium (K) $L_{II,III}$-edges are denoted, too;* **b)** *the structural formula of a model HA, as suggested by Stevenson [183] and* **c)** *the second derivative of the spectrum.*

The approximation of the elemental compositions, shown in Tab. 4.3 used here yields values close to the analytical data, directly taken from the supply company Sigma Aldrich. For comparison, elemental composition data from the literature is given, too. Monteil-Rivera et al. [125] determined the elemental composition with an elemental analyzer (CONS) and with x-ray photoelectron spectroscopy (XPS). Sierra et al. [173] used

Table 4.3: *Elemental composition of the analyzed reference HA, shown in Fig. 4.4a. For the values gained from the evaluation with SpecFit from the NEXAFS data, the percentages in elemental composition have been calculated by setting the sum of the five main contributors to 100 %.*

sample	method		composition [%]				
			C	H	O	N	S
HA (Sigma)	analytical	Sigma-Aldrich	54.7	4.4	36.3	0.8	3.8
	CONS	Monteil-Rivera	64.0	n.n	30.6	1.0	4.4
	XPS	et al. [125]	68.7	n.n	25.9	1.1	4.3
	CP/MAS ^{13}C NMR	Sierra et al. [173]	69.4	2.7	21.9	n.n	6.1
	NEXAFS + SpecFit		56.3	3.1	36.0	1.8	

solid state CP/MAS ^{13}C-NMR spectroscopy (CP = cross polarization, MAS = magic angle spinning) for the chemical analysis of this HA sample.

Table 4.4: *Energy positions and assignments of features in the C 1s NEXAFS spectrum of the reference HA in Fig. 4.4a. The last five features have not been taken into account to calculate the elemental composition in Tab. 4.3, see text.*

sample	position [eV]	1s → (orbital)	main character	area under Gauss [%]
	285.4	$\pi^*_{C=C}$	quinones, aromatic	6.5
	286.4	$\pi^*_{C=C}$	phenolic	3.8
	287.3	σ^*_{C-H}, 3s	carbohydrates	6.1
	289.0	$\pi^*_{C=O}$	carbonyl, carboxyl	20.3
	290.8	Ryd, 4p, 3p		14.54
HA	291.7	σ^*_{C-N}, σ^*_{C-S}, σ^*_{C-H}		1.6
(Sigma)	292.3	σ^*_{C-C}, σ^*_{C-O}		11.3
	293.8	σ^*_{C-O}, σ^*_{C-C}		20.1
	295.7	σ^*_{C-C}, Ryd		15.9
	297.4	K L_{III}	potassium	
	299.7	K L_{II}	potassium	
	302.8	$\sigma^*_{C=C}$		
	307.7	$\sigma^*_{C=C}$, $\sigma^*_{C=O}$		
	313.0	$\sigma^*_{C=C}$, $\sigma^*_{C=O}$		

In Fig. 4.5, it is illustrated how difficult it would be to conclude the composition of a heterogeneous environmental sample from linear combination of standards. The lower six plots are spectra of organic polymers that contain components, which could also be found in an environmental sample. The data were obtained from Hitchcock [76], Jacobsen et al. [95] and Dhez et al. [51]. In addition, the average of these six spectra was taken (red plot). Comparing this average with the spectrum of the reference HA reveals many similarities. As carbon has the ability to catenate, the choice of appropriate standards would be a challenge on its own. Thus, without enormous computational efforts it is not possible to calculate the spectra of large heterogeneous organic compounds recursively, since they do not have a well defined structure like a crystal for instance.

4.2.2 Environmental Samples

With the results obtained from the reference samples, four environmental samples of unknown composition could be analyzed. These samples were

- Two HAs from a gleyic chernozem from an Ah horizon (German taxonomy: Schwarzerde, from Rosdorf near Göttingen, Germany, [4, 161]) extracted
  - · by Na-pyrophosphate solution (pH = 7.0), referred to as HA1, or
  - · by sodium hydroxide solution, referred to as HA2, respectively.

A chernozem is a black soil rich in organic matter and due to that very fertile; the Ah horizon is located few centimeters below the surface; gleyic refers to influence of groundwater.

- An aquatic FA from lake Hohloh in the Black Forrest obtained by sorption on a resin (XAD), according to the procedure of the IHSS (International Humic Substances Society).

- A size fraction of a luvisol soil with a low content in organic matter in general (again from the Göttingen area). Luvisols have a high clay content and are most common in flat regions or forests.

The spectra of the measurements are depicted in Fig. 4.6. The estimation of the chemical composition is shown in Tab. 4.5. For comparison to the reference sample spectra, the analysis of the peak assignment of the luvisol soil is shown in Tab. 4.6. The spectra in Fig. 4.6a and 4.6b stem from the HAs of the identical gleyic chernozem, but were extracted with different methods.

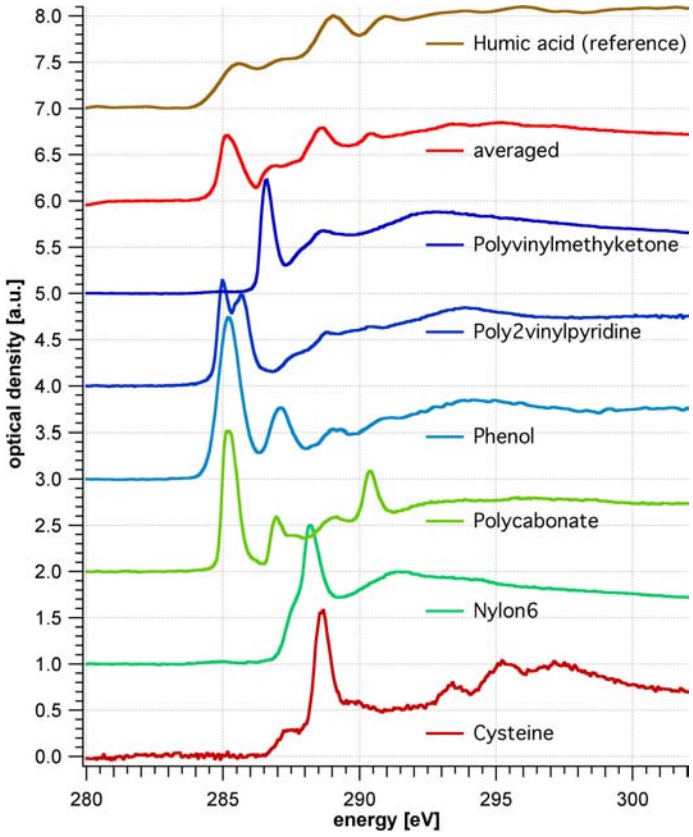

Figure 4.5: *Spectra of six organic compounds and their average. For comparison the spectrum of the reference HA is plotted, too. The purpose is to illustrate the difficulties to determine the structure of a heterogeneous sample by linear combination of standards.*

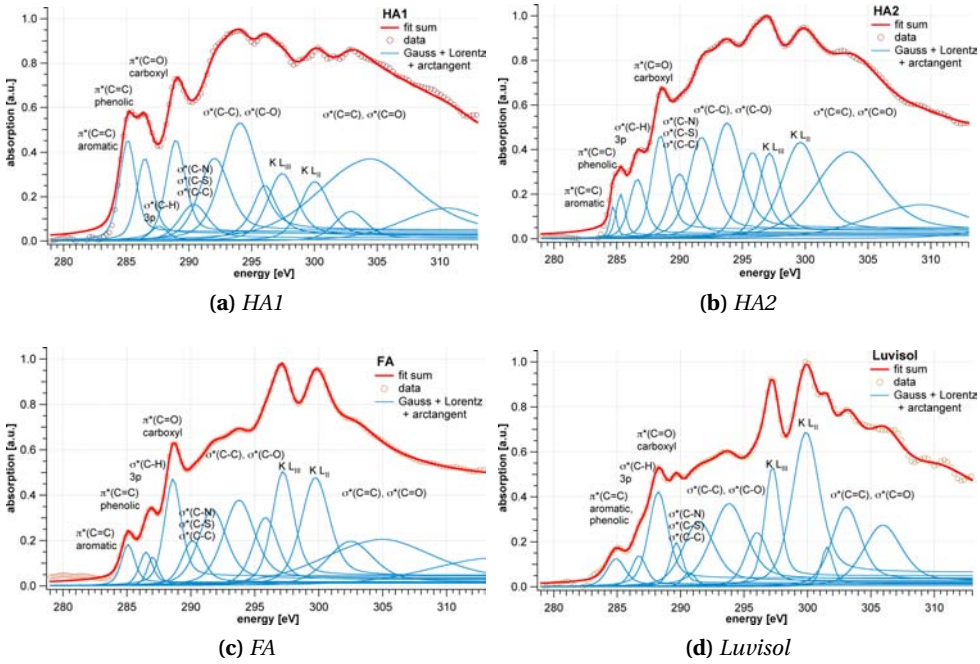

(a) *HA1* **(b)** *HA2*

(c) *FA* **(d)** *Luvisol*

Figure 4.6: *Result of NEXAFS spectroscopy on four different samples:* **a)** *HA1 (extracted with NaOH from a gleyic chernozem soil sample),* **b)** *HA2 (extracted with NaOH from same chernozem soil sample),* **c)** *FA of aquatic origin, and* **d)** *unfractionated luvisol soil. The resulting elemental compositions are listed in Tab. 4.5.*

From the NEXAFS experiment the effect of these different methods becomes clear. HA1 exhibits a strong absorption around 285 eV - 286 eV, where the benzene and phenolic peaks are located - the area under the two Gaussian curves is 22.8 %. The strong C signal masks the two potassium peaks resulting from the L_{III} and L_{II} absorption edges.
HA2 shows a high aromatic and phenolic content, together 14.1 %, but the ratio of carbonyl/carboxyl to these C=C binding groups is more in favor of the COO(H)-groups than in the first sample in Fig. 4.4a; with a value of 11.3 %, the peak around 288.5 eV is much higher than the the ones at 285 eV and 286 eV. The spectral features of the HA1 resemble the reference HA in Fig. 4.4a more closely.
The spectrum of the sample depicted in Fig. 4.6c yielded the results expected from a FA [32, 63], in particular the lower C content compared to the O content, observable from the smaller peaks around 285 eV - 286 eV (9.3 %) and the high $\pi^*{}_{C=O}$ resonance at 288.1 eV (17.0 %). Comparing the results in Fig. 4.4a, 4.6a and 4.6b, i.e., samples HA, HA1 and HA2, to the FA, the content of carboxylic groups is highest for the latter. This coincides with chemical analysis [183]. In general, FAs of aqueous origin contain relatively less C than samples extracted from soils, which means that more O and other atoms are incorporated in the FA molecules, as has been proved by other authors with several other methods.

The FA has also been studied using XPS [32]. The peak assignments and also the way of calculating the elemental composition are in good accordance to the results reported here. To show that whole soil samples without being extracted or processed by other preparation

Table 4.5: *Elemental composition of the analyzed environmental samples, two HAs, one FA, and a soil, shown in Fig. 4.6. The percentages in elemental composition have been calculated by setting the sum of the five main contributors to 100 %.*

	sample	composition [%]				
		C	H	O	N	S
environ-	HA1	60.1	1.7	33.5	4.7	
mental	HA2	56.1	1.5	35.3	7.0	
samples	FA	54.9	1.5	37.7	6.0	
	Luvisol	51.9	2.4	40.1	5.7	

techniques can be investigated, too, the Ah-horizon of a luvisol under agricultural use was chosen; the corresponding NEXAFS spectrum is presented in Fig. 4.6d. This type of soil contains a high amount of clay minerals, and other inorganic materials. The overall content of organic carbon is around 2.5 % in the studied soil layer [4]. Here, the $\pi^*_{C=O}$ peak (from carbonate) in the NEXAFS-spectrum is prominent and the aromatic peak appears to be the lowest of all four samples. It is assumed that this high peak is due to liming of the soil, a common practice to increase its fertility. Owing to the low carbon content and higher content of illitic materials of the luvisol, the resonances of the K $L_{II,III}$-edges are particularly high in this spectrum.
The spectra shown in this section are well comparable to those achieved with synchrotron radiation [42, 164, 178, 179], as they exhibit the expected peaks at the characteristic positions. This consistency could provide the possibility to perform test experiments with samples, which are later studied in more detail with synchrotron light. In addition, they could give an impulse on the broader spread of the application of NEXAFS spectroscopy. Nonetheless, due to the setup of the instruments the recorded spectra only give information about the averaged sample and of course the source does not reach the brilliance of a synchrotron. Spatial resolution as for instance provided by spectromicroscopy cannot be expected. Furthermore, the grating does not allow for a spectral resolution better than 0.2 eV in the energy range that was used for the experiments here.

4.3 Impact of Different Extraction Techniques

The second series of HS samples characterized the influence of the extraction method and the solvent on the humic fraction. As mentioned in section 4.1, the HS can bind metal ions. They play an important role in reducing Fe(III) to the more reactive Fe(II). For this to happen, HS can be in an oxidized or in a reduced state [60, 185]. Since the sample preparation for the measurements was on air, the natural state for the HS was oxidized. Re-

Table 4.6: *Energy positions and assignments of features in the C 1s NEXAFS spectrum of the luvisol soil, shown in Fig. 4.6d. The last five features have not been taken into account to calculate the elemental composition in table 4.5, see text.*

sample	position [eV]	1s → (orbital)	main character	area under Gauss [%]
	284.9	$\pi^*_{C=C}$	quinones, aromatic, phenol	5.3
	286.7	$\pi^*_{C=C}$, 3s, σ^*_{C-H}	aliphatic C, carbohydrates phenol	4.7
	288.7	$\pi^*_{C=O}$	carbonyl, carboxyl	18.9
	289.7	3p, σ^*_{C-C}, σ^*_{C-H}	alkyl C	5.7
luvisol	290.7	σ^*_{C-N}, σ^*_{C-S}		1.8
	291.4	σ^*_{C-C}, Ryd		21.1
	293.8	σ^*_{C-C}, σ^*_{C-C}		30.1
	296.0	σ^*_{C-C}, σ^*_{C-O}		12.4
	297.2	K L_{III}	potassium	
	299.9	K L_{II}	potassium	
	301.5	$\sigma^*_{C=C}$		
	303.0	$\sigma^*_{C=O}$		
	305.9	$\sigma^*_{C=C}$, $\sigma^*_{C=O}$		

duced HS can even reduce Fe(III) in crystallized form, naturally found in soils as hematite or goethite [15]. That way, the bioavailability of iron increases for micro-organisms and bacteria [14].

For illustration, the difference in NEXAFS spectra of an oxidized and a reduced HA is shown in Fig. 4.7. These spectra were taken from a stack recorded at BESSY II, because the program to record spectra was not implemented at that time. The imaged area is therefore not relevant and not shown. Unfortunately, the spectra are very noisy and therefore only qualitative statements are made.

Quinone, phenolic and carboxylic groups are the functional groups that are mainly involved in redox processes of HS. In the reduced state, the peak of the phenolic groups is much smaller. The peak of the quinone groups is located close to the aromatic peak, see Tab. 4.4. With a stepsize of 0.2 eV both can hardly be distinguished, but the contribution of the quinone is smaller, because in peak at 285 eV is more narrow. However, the carboxylic peak decreased, too, which can be concluded from the ratio of the aromatic to the carboxylic peak. For the oxidized state it is 0.5, for the reduced 0.6.

By observing the change of these peaks, conclusions can be drawn about the involvement of HS in electron shuttling processes, redox reactions or complexation of metal ions.

Bauer [14] investigated the amounts and ways of metal binding, especially Fe, to HS. To do so, different procedures were used to successively extract the Fe ions from the reference HA, already studied in section 4.2.1.3. Among the commercially available HS, the widely used

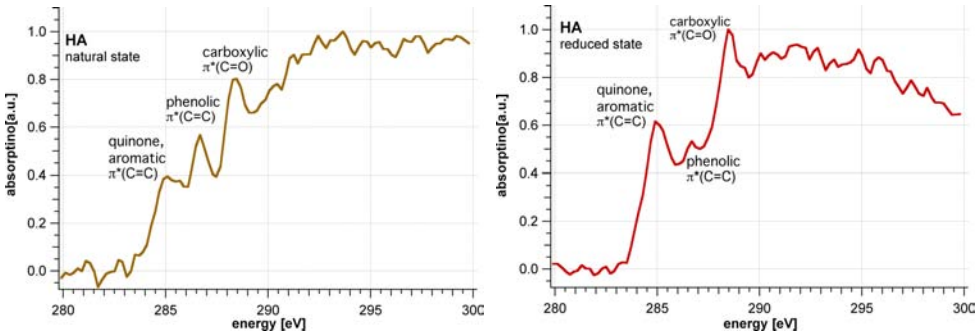

(a) *Oxidized HA* **(b)** *Reduced HA*

Figure 4.7: *Spectra from dry HA in* **a)** *oxidized or natural state and* **b)** *reduced state, recorded with the STXM at BESSY II with a stepsize of 0.2 eV.*

Aldrich HA possesses a rather high Fe content (several weight-%) as stated in the certificate of the HA analysis from Aldrich with exact concentrations varying from batch to batch) [14]. After each extraction, the amount of Fe was measured using size exclusion chromatography. The different extraction steps are described briefly below, together with the results of the NEXAFS spectroscopy, which monitor the changes in the functional groups. The effect of the extraction steps on the HA is analyzed to demonstrate the feasibility in the NEXAFS spectra, recorded with a laboratory source.
The experiments in correlation with the spectra reported here were all carried out using phosphate buffer (see next paragraph). Therefore, the NEXAFS spectra were first recorded with samples from the (extracted) HA samples suspended in this buffer. For comparison and to investigate of the effect of the solvent, the HA samples were suspended in ultrapure water, too.

Extraction process and sample preparation The processes are explained in more detail elsewhere [14], and therefore are only briefly summarized here. In the first extraction step, sodium acetate (1M $Na(CH_3COO)$ solution, pH = 5) was used to gain the Fe ions that were only weakly bound by the HA. For the second and third step, hydrogen chloride (HCl) was used. First, 0.5M HCl for Fe bound in weak complexes, then 6M HCl for stronger complexed Fe. In the last step, the strongly bound Fe ions were removed using dithionite-citrate-bicarbonate (DCB, 0.3M Na-citrate, 1M $NaHCO_3$, 12 mg Na_2SO_4). In each step the extracted HA precipitated as a pellet that was resuspended and treated further. For the sample preparation for the NEXAFS spectrometer, dry samples were used. They were resuspended in ultrapure water (Millipore) or phosphate buffer (50mM, pH = 7, KH_2PO_4 and $Na_2HPO_4{\cdot}2H_2O$, analytical grade, Aldrich) and droplets of 2 µl were put on Si_3N_4, where they dried, as described before.

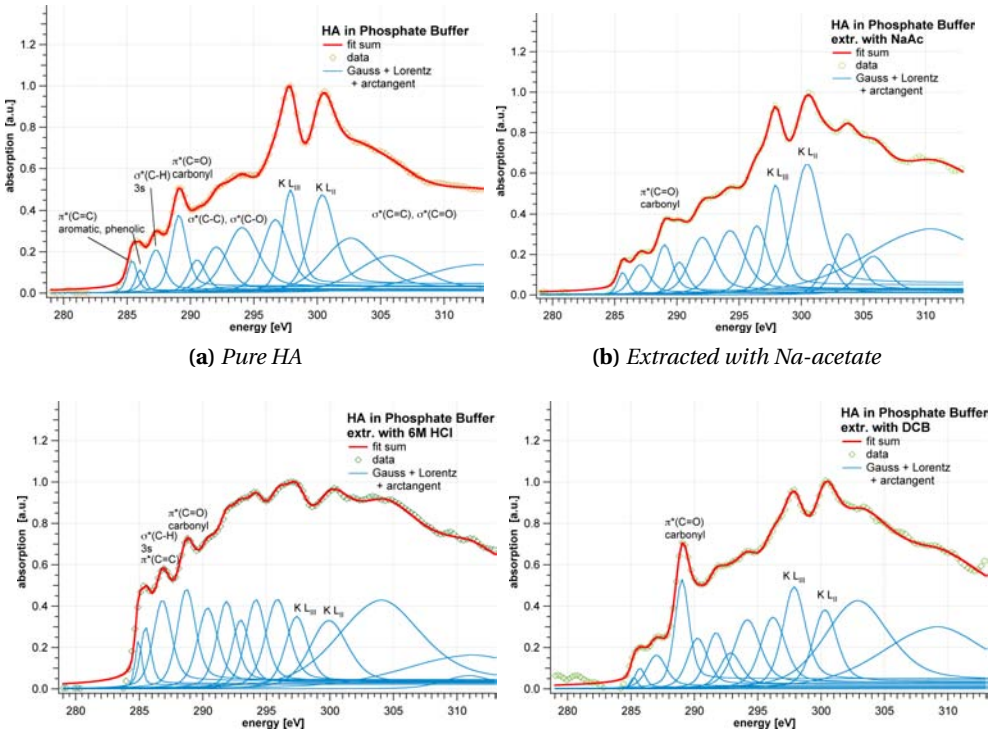

(a) *Pure HA* **(b)** *Extracted with Na-acetate*

(c) *Extracted with HCl* **(d)** *Extracted with DCB*

Figure 4.8: *Result of NEXAFS spectroscopy on HA (Sigma) successively extracted and suspended in phosphate buffer before sample preparation:* **a)** *pure HA,* **b)** *HA after extraction with Na(CH_3COO), **c)** HA after extraction with 0.5M HCl and 6M HCl, and* **d)** *after extraction with DCB.*

4.3.1 HA in Phosphate Buffer

The results of the experiment of the HA in phosphate buffer are depicted in Fig. 4.8. In all spectra, the peaks of the K $L_{III,II}$ are very prominent, due to the K in the buffer. Although the buffer had a neutral pH value (pH = 7) like the ultrapure water, it influences the chemical binding environment, which is observed by comparison of Fig. 4.4a and 4.8a. The resonance at 290.5 eV, where contributions from transitions to $\sigma^*_{C\text{-}C}$, but also to $\sigma^*_{C\text{-}N,S,F,P}$ are located, is smaller for the HA in phosphate buffer. The ratio of $\pi^*_{C=C}$ (aromatic, 285 eV) to $\pi^*_{C=O}$ (carboxylic, 289 eV) is the same for both solvents, $\pi^*_{C=C}/\pi^*_{C=O} = 0.49$.
The effect of the different steps to extract Fe is clearly visible in the NEXAFS spectra. After extraction with Na(CH_3COO), the K $L_{III,II}$ peaks are even more prominent, the ratio $\pi^*_{C=C}/\pi^*_{C=O}$ is a little lower (0.45). The spectrum is shown in Fig. 4.8b. The peaks of transitions to π^* orbitals have decreased in comparison to the transitions to σ^* orbitals at energies above 290 eV. Na(CH_3COO) is also used to extract loosely bound carbonate [79]. The carbonate peak is also located around 289 eV.

After the extraction step with HCl, the HA was strongly protonated. This led to further decreasing of the π^* resonances, but the ratio $\pi^*_{C=C}/\pi^*_{C=O}$ is now 0.66, as depicted in Fig. 4.8c. The increased amount of C-H bonds among others contributes to the resonance at 290.5 eV. Using HCl, non-exchangeable K was also extracted, therefore the K $L_{III,II}$ is much lower after this extraction step.
The last extraction step, using DCB, removed very strongly bound Fe, which could be mainly bound to carboxyl groups [42]. After the extraction of the Fe, the citrate remained in the HA which is observed in the high peaks at 289 eV and the ratio $\pi^*_{C=C}/\pi^*_{C=O}$ being reduced to 0.28.

4.3.2 HA in H_2O

The NEXAFS spectra of the extracted HA, resuspended in ultrapure water before sample preparation, are displayed in Fig. 4.9. The sample with the HA after extraction with $Na(CH_3COO)$ was destroyed during the pumping or the measuring process in the spec-

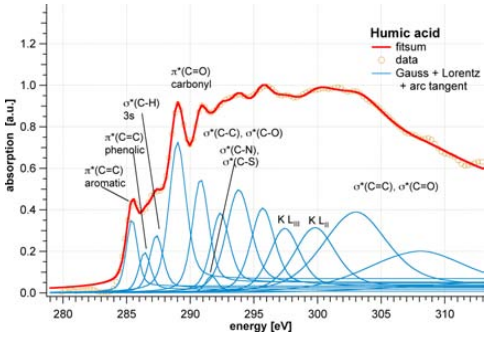

(a) *Pure HA*

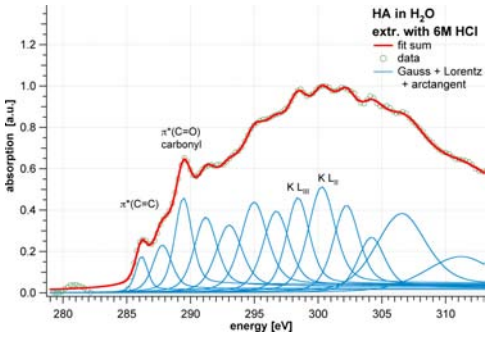

(b) *Extracted with HCl*

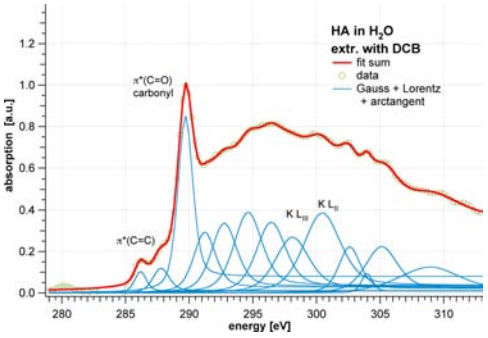

(c) *Extracted with DCB*

Figure 4.9: *NEXAFS spectra of HA (Sigma) successively extracted and suspended in H_2O before sample preparation:* **a)** *pure HA,* **b)** *HA after extraction with 0.5M HCl and 6M HCl, and* **c)** *after extraction with DCB.*

trometer; therefore, no plot of the spectrum is shown.
In the spectra of the HA in the original form and after the other two extraction steps, of course, the K $L_{III,II}$ peaks are less prominent and only visible if the spectra are thoroughly analyzed. If the spectra of the HA after extraction with HCl are compared (Fig. 4.8c and 4.9), one notices that the peak at 290.5 eV is smaller for the sample with H_2O, too. This is also seen when the non-extracted HA are compared. But here, the ratio $\pi^*_{C=C}/\pi^*_{C=O} = 0.39$ is lower than it is, when phosphate buffer is used. In the last spectrum, recorded after the extraction with DCB, the $\pi^*_{C=O}$ peak stemming from the citrate is very prominent, which is also seen in a ratio $\pi^*_{C=C}/\pi^*$ of 0.16.

4.4 Recapitulation

Using a lab-based instrument with a compact x-ray source, NEXAFS spectra of heterogeneous environmental samples have been recorded and a new approach of data analysis was developed. The spectra of the extracted HAs and FA are in good agreement with data of similar samples obtained at synchrotrons reported in the literature [42, 164, 179]. It was even possible to record a spectrum of a whole soil sample, without further extraction or preparation. Yielding reliable and reproducible results, such table top instruments, could thus serve as a complementary technique to test and prepare synchrotron-based NEXAFS experiments, if not sometimes as an alternative, if it is not necessary to record very detailed spectra. The analysis uses a new approach to fit the NEXAFS spectra, by introducing a *valence band* for every peak represented as arc tangent for every resonance, thereby taking the heterogeneity of the samples into account. From the analysis quantitative statements about the elemental composition and even the relative amount of the binding types were made. It should be noted, however, that this approach was only tested for organic samples with a C fraction much higher than the fraction of the other elements. This should be taken into account, if other samples are analyzed by this empirical method.
The different sequential extraction procedures to remove the bound and complexed Fe from the HA also leads to changes in the HA. This is observed in the variation of the $\pi^*_{C=C}/\pi^*_{C=O}$ ratio. With increasing number of extractions, the number of π^* resonances seems to decrease, compared to the changes in the spectral signature at energies above 290 eV. These alterations are possibly due to bulk structural changes.
The use of different solvents has an effect on the HA [45], which is observed in the spectra, too, although the samples are dry when mounted. In the phosphate buffer samples not only the strong K $L_{III,II}$ peaks are noticeable, but also the weaker resonances at 290.5 eV and around 289 eV, where the carboxyl and carbonate peaks are found, showing that the choice of the solvent influences the chemical composition of the sample. This should be taken into account, when analyzing soil samples or other specimens that need to be extracted, and when comparing experiments using different solvents.
In addition to the experiments presented here, there is still potential to increase the scope of application of the NEXAFS technique. The setup allows for surface specific measurements, since it is possible to study the samples in reflection mode, too [143]. In that mode, the formation of organic coatings on mineral substrates could be directly observed. Additionally, other elements like potassium are detectable and it should be possible to gain

more information on their chemical environment.
The preparation of the samples for the measurement is described as straightforward and noninvasive, but only for dry samples. In spite of that, it is also manageable to study wet or anoxic samples, if a small droplet or amount of the sample is enclosed between two Si_3N_4-membranes and then sealed with lacquer or glue, thereby building a small wet chamber. In addition, the spectral range of the target gas Kr extends between 260 eV and 800 eV. That way it would also be possible to study the Ca signature of soil samples, or the interaction of ROS and mineral particles in general. Furthermore, by applying other filters or sample holders, information about the N K-edge and Fe $L_{II,III}$-edges could be gained.
Currently the number of compact laser driven x-ray sources for spectrometers (and microscopes) is small but increasing. Due to this and instrumental developments, a higher throughput of interesting samples directly in the laboratory of an institute can be envisioned – at the moment with accumulated times of approximately five samples per hour. The experiments presented here demonstrate clearly what experiments with compact x-ray sources are already feasible and how to proceed with the resulting data.

5 Carbon Nanotubes (CNTs) and Soil

The aim of the experiments described in this chapter is threefold. Firstly, carbon nanotubes (CNTs) are studied using x-ray spectromicroscopy to understand their properties in wet and dry state. Secondly, their interaction with environmental samples is observed, and thirdly, CNTs are idealy suited to test an alternative analysis algorithm of image stacks, because of their unique chemical structure.

5.1 CNTs

Since their discovery in 1991 [90], the techniques to produce CNTs in sizable quantities have been improved continuously. Currently, several thousand tons of CNTs are produced per year, so the investigation of their interaction with the environment, either being introduced willingly, e.g., for remediation of soils [218] or unintendedly after disposal, is of key importance.
CNTs belong to the fullerenes, their atomic structure comprises of C atoms, each tetrahedrally bound to three other C atoms (sp^2-hybridization), resulting in a honeycomb-like pattern of their walls (Fig. 5.1). Apart from their structure, the unique properties of CNTs

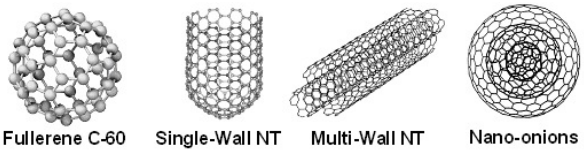

Figure 5.1: *Overview of elements of the fullerene family, adapted from HZDR [88].*

also stem from their enormous aspect ratio, with a diameter in the nm-range, but a length up to several mm. For the work described here multi-walled CNTs with an outer diameter of 10 nm - 30 nm and a length distribution of 0.5 µm - 2 µm were used [162]. The properties of these still relatively new materials promise a large variety of applications, of which some are already realized. Depending on their design, CNTs can be functionalized showing metallic or semiconducting properties [27, 99]. Combining suitably designed CNTs with the right materials can optimize these, e.g., the addition of CNTs to concrete makes the building material lighter and more flexible [130], alloys of steel and CNTs are extremely hard and rustproof [153]. In medicine and pharmacology, CNTs are currently tested for drug design and delivery [147]. In biophysics, CNTs are also used to simulate Brownian motion of polymers [56]. Furthermore, studies regarding site specific soil remediation aided by the application of CNTs are discussed [64, 145, 209].

Among other techniques, spectroscopy is used for these investigations, however mostly only as bulk measurements. Methods to image these nano-sized particles are often based on electron or atomic force microscopy. By these techniques, the CNTs cannot always be investigated under ambient conditions, a crucial necessity for gaining information about the interaction between CNTs and other particles or about the long-term behavior of CNTs within the environment.
In this first part, the CNTs are studied thoroughly in dry and wet state and their alteration with time is monitored. Furthermore, their ability to absorb heavy metals is described using x-ray spectromicroscopy.

5.1.1 Pristine and Modified CNTs

Samples Two different types of samples were investigated. The CNTs were purchased from IoLiTec (Denzlingen, Germany) with a purity of 95%. These are the reference CNTs, in the following called rCNTs. A modification procedure, performed by [162], was achieved by heating the rCNTs in a mixture of HNO_3 and H_2SO_4 (volume fraction 3:1) to 100°C under reflux for three hours and ultrasonication for 42 hours (at 60 - 70°C). The modification functionalized the rCNTs with carboxylic groups, simulating possible environmental influences [219]. The modified CNTs will be referred to as mCNTs in the following. The rCNTs and mCNTs were kept as 1 %-standard solutions (Millipore water, weight fraction) in glass vessels (Eppendorf, Germany).
A difference in dispersion behavior could already be observed from looking at the glass vessels after shaking, see Fig. 5.2, which will be discussed further below. A sketch of the ba-

Figure 5.2: *Photograph of the mCNTs (left) and rCNTs (right) after short shaking, showing the better dispersing property of the mCNTs. The rCNTs have already started to sink.*

sic principle of the sample preparation is depicted in Fig. 5.3a, together with an illustration of the mounted sample in Fig. 5.3b. Preparation of the dry samples was straightforward: a 1 µl - 2 µl droplet of the sample solution was deposited on a Si_3N_4-membrane (thickness 100 nm, purchased from Silson Ltd., Northampton, UK). After the water had evaporated, leaving the solid matter behind, the membrane was mounted on a sample holder and inserted into the microscope. For the aqueous samples, a droplet of sample solution was deposited on a Si_3N_4-membrane and covered with a second membrane. The interspace

was sealed with glue, preventing exsiccation. That way a stable wet chamber was build, with a water layer thickness of about 1 µm - 2 µm.

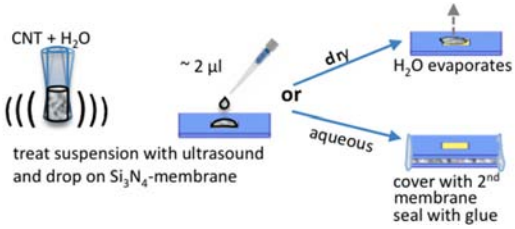

(a) *Sample preparation*

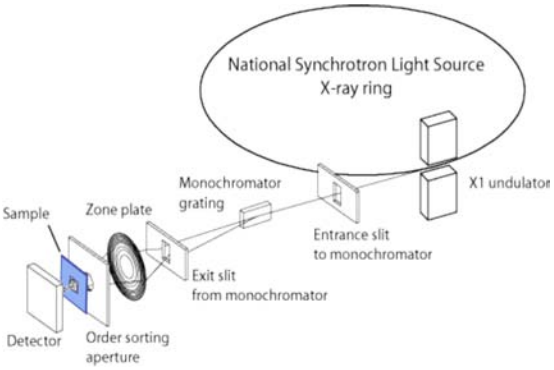

(b) *STXM setup*

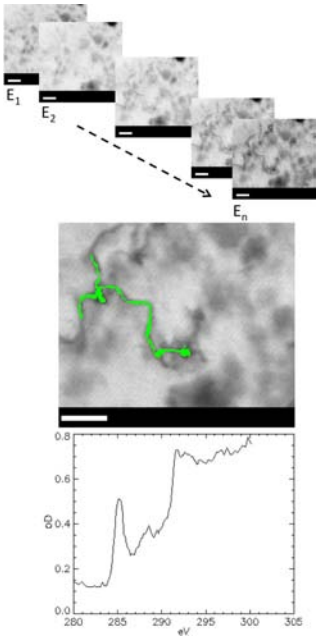

(c) *Acquiring an image stack*

Figure 5.3: *Basic principle of a spectromicroscopic experiment.* **a)** *Before the preparation, the sample is treated with ultrasound. After the larger particles had time to settle, a dropet of the supernatant is deposited on a Si_3N_4-membrane. For dry samples, the water has to evaporate before mounting the sample, for aqueous samples a wet chamber is built as explained in the text.* **b)** *Schematic view of the STXM setup and the position of the mounted sample at the NSLS at BNL.* **c)** *Acquisition of a stack of images. From top to bottom: after alignment of the images, a region of interest (ROI) is chosen (ROI in green, I_0 not shown), which gives a NEXAFS spectrum. The scale bar indicates 1 µm.*

Analysis For the evaluation of the image stacks the program *stack_analyze* in combination with *pca_gui*, both written by C. Jacobsen and his group [93, 118], was used. The images of a stack are aligned, and the signal I of regions of interest (ROIs) and the signal I_0 of regions without sample are determined by adding up the signal per pixel within the chosen areas. The absorption spectra are plotted as a function of optical density oD ($oD = -\ln \frac{I}{I_0}$), as sketched in Fig. 5.3c.
Because some the data acquired with the STXM at BESSY II were noisy, the data sets obtained there were smoothed using binomial smoothing with a box width of 1, and normalized by setting the highest point to 1. For illustration, in Fig. 5.4c and Fig. 5.5b, the original spectra are plotted, too. Due to that and the fact that the data is synchronized

as *pgm*-files, calibration bars are only shown for the measurements carried out with the X1-A1 at the NSLS, more detail is found in the appendix A.

5.1.1.1 Experiments at BESSY II

The first measurements were performed using the STXM at BESSY II. At first, the pristine rCNTs were studied (Fig. 5.4). Comparison of the images of the rCNTs obtained with a REM (Fig. 5.4a) and the STXM (Fig. 5.4b) shows that bundles of the rCNTs and even single tubes are resolvable. In the stack area, no differences in the spectra were observed. The two prominent spectral resonances are characteristic for CNTs, and have been reported before [12, 58, 193, 223]. The peak at 285.3 eV, stems from the transition 1s $\rightarrow \pi^*_{C=C}$ in aromatic rings, the resonance at 291.5 eV is the corresponding transition 1s $\rightarrow \sigma^*_{C\text{-}C}$. Characteristic values and important resonances for this and the following CNT-spectra are gathered in Tab. 5.1. The splitting observed from the σ^*-peak and also weaker in the π^*-peak can be attributed to the coiling of the structure in the CNTs [193].

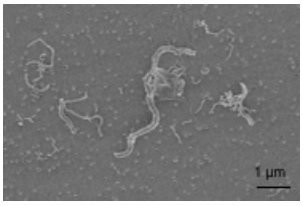

(a) *rCNTs, dry, REM*

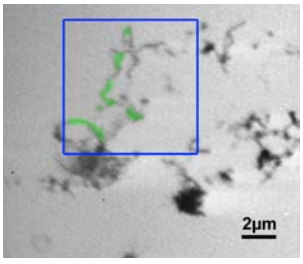

(b) *rCNTs, dry*

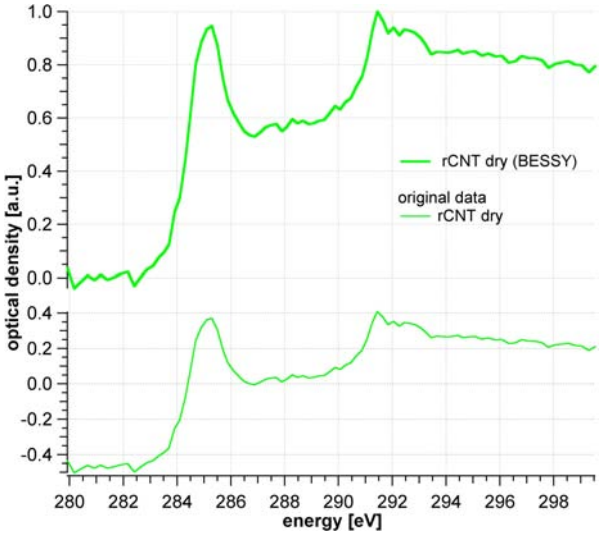

(c) *Spectrum of rCNTs*

Figure 5.4: a) *Image of dry rCNTs, recorded with a raster electron microscope (REM), adapted from Schierz and Zaenker [162].* **b)** *Image of rCNTs dried on Si_3N_4-membrane (pixel size 50 nm, 3 ms dwell time, 300 eV), the blue frame indicates the stack area.* **c)** *Corresponding plot of the rCNTs, in smoothed and normalized and in original form.*

The rCNTs were then studied in the wet state, enclosed between two Si_3N_4-membranes, shown in Fig. 5.5. Here, thick clusters are observable due to van der Waals forces acting on the hydrophobic rCNTs. The thick cluster (ochre plot in Fig. 5.5b) has a significantly different spectral signature, than the smaller rCNT-bundles.
The peak at 285 eV is visible in both spectra, but it is clear that the rCNTs in the clustering has a strong effect on the spectra of rCNTs. Inside the cluster, distinct features are hard to

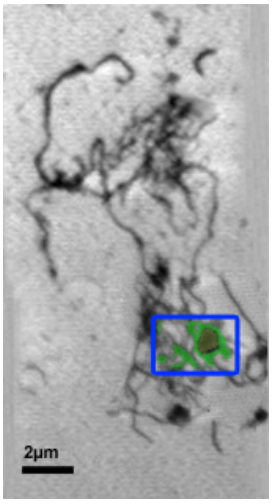

(a) *rCNTs, aqueous*

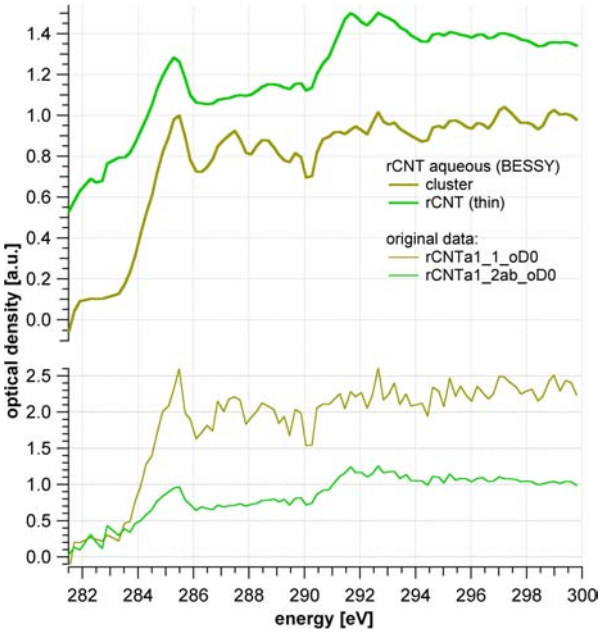

(b) *Plot of ROIs*

Figure 5.5: a) *Image of rCNTs in wet state, merged from x-ray micrographs (smallest pixel size 50 nm, 12-18 ms dwell time, 300 eV).* **b)** *Plot in corresponding colors of regions inside the rCNT-cluster and the thin outer sections, shifted for clarity.*

assign in the NEXAFS spectrum, apart from the absorption step and the $\pi^*_{C=C}$ peak, which, besides, is shifted to a slightly higher energy 285.5 eV. The thinner rCNT bundles (green plot in Fig. 5.4b) exhibit a spectrum, similar to the dry rCNTs in Fig. 5.4c. However, the $\sigma^*_{C\text{-}C}$ resonance around 291.5 eV is smaller, and the ratio $\pi^*_{C=C}$:$\sigma^*_{C\text{-}C}$ is only 0.76 (0.94 in Fig. 5.4c). Additionally, a small shoulder is visible at 290.6 eV. To sum up this first approach, the water forces the rCNTs to cluster and influences the double bonds.
The mCNTs were studied under the same conditions as the rCNTs. The results of the dry mCNTs are depicted in Fig. 5.6. The micrographs recorded with a REM (Fig. 5.6a) and the STXM (Fig. 5.6b) illustrate how strongly the modification process damages the CNTs. Only very few tubes are discernible, most of the mCNTs are reduced to small pieces. It is also visible that different parts have different spectral signatures, as seen from the plots of the regions of interest (ROIs) in Fig. 5.6b and 5.6c. In the thin parts, a very strong peak at the transition energy of 1s→ $\pi^*_{C=O}$ (288.3 eV) is visible. This peak overlaps with the resonance 1s → $\sigma^*_{C\text{-}H}$ (287.5 eV) that originates from local defects in the CNT-structure. For the very dark clusters, this peak is not observed. Other noticeable features also indicate damage of the CNTs due to the modification procedure. The ratio $\pi^*_{C=C}$:$\sigma^*_{C\text{-}C}$ varies between 0.8 (red plot) and 0.49 (purple plot), the $\pi^*_{C=C}$ resonance is broader than for the dry rCNTs and shifted towards lower energy (285.0 eV). Besides, the $\sigma^*_{C\text{-}C}$ resonance is rather an edge

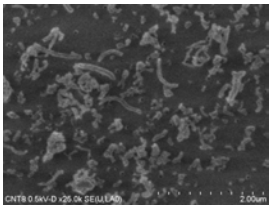

(a) *mCNTs, dry, REM*

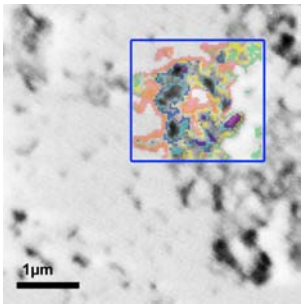

(b) *mCNTs, dry*

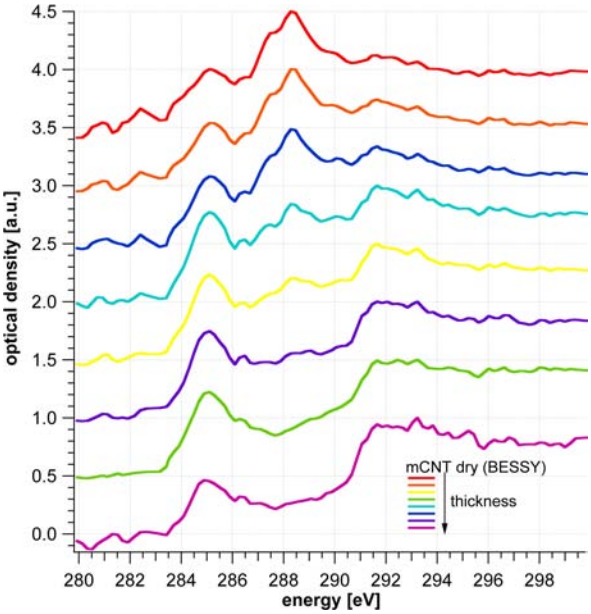

(c) *ROI spectra of mCNTs*

Figure 5.6: a) *Image of dry mCNTs, recorded with a raster electron microscope (REM), by courtesy of H. Zaenker.* **b)** *Image of mCNTs in dry state (pixel size 50 nm, ms dwell time, 300 eV), stack area with color-coded ROIs.* **c)** *Plot in corresponding colors of ROIs, shifted for clarity.*

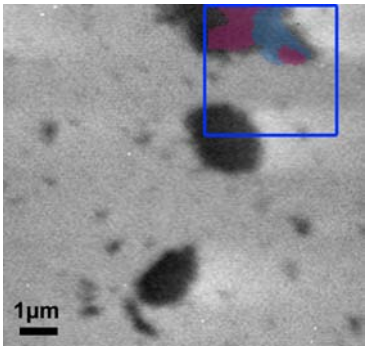

(a) *mCNTs, aqueous*

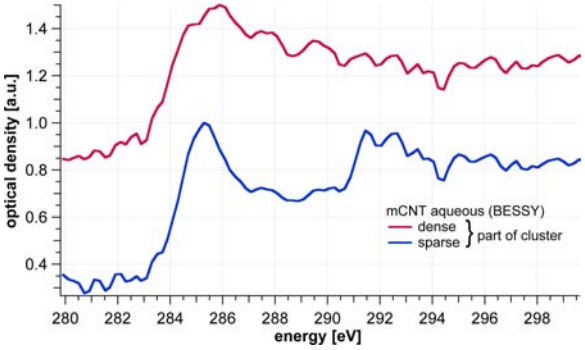

(b) *Plot of ROIs*

Figure 5.7: a) *Image of mCNTs in wet state (smallest pixel size 50 nm, 6 ms dwell time, 300 eV).* **b)** *Plot in corresponding colors of regions inside the mCNT-cluster and the thin outer sections, shifted for clarity.*

than a pronounced peak. The high resonance around 288 eV is more prominent for the thin regions and the borders of the clusters.

The results of the mCNTs studied in wet state is shown in Fig. 5.7. The clustering effect is particularly strong in this sample. Only few of the mCNTs are visible outside the clusters in Fig. 5.7a and these do not appear like tubes. The spectrum of the dense part of the cluster (Fig. 5.7b) only exhibits a broad absorption edge jump, but no distinct resonance peaks are recognizable. The spectrum of the thinner part of the cluster possesses characteristic features of a CNT spectrum, but the $\sigma^*_{\text{C-C}}$ peak is less pronounced than for the rCNTs in wet state shown in Fig 5.5. Furthermore, the peaks of the transitions $1s \rightarrow \pi^*_{\text{C=O}}$, $\sigma^*_{\text{C-H}}$ are not present, not even at the borders of the cluster.
Before each sample preparation, the 1 %-standard solutions were shaken. The different dispersion behavior also shows that the rCNTs are more hydrophobic, due to their intact tube structure and. Therefore, they mix less well, as depicted in Fig. 5.2 that was recorded after shaking the CNTs by hand.

5.1.1.2 Experiments at NSLS

To verify the experiments presented above, and to investigate the long time behavior of the rCNTs, the experiments have been repeated using the STXM X1-A1 at the NSLS. The highest resolution achieved with this instrument is 30 nm, but often oversampled images have been recorded with 25 nm per pixel or 12.5 nm per pixel.

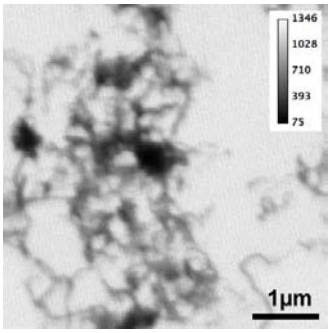

(a) *rCNTs, dry*

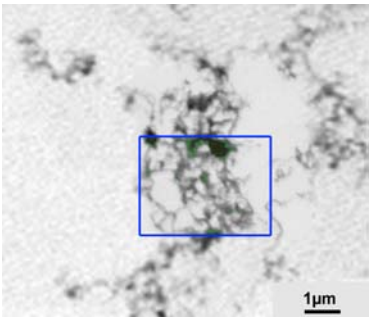

(b) *rCNTs, dry, with ROIs*

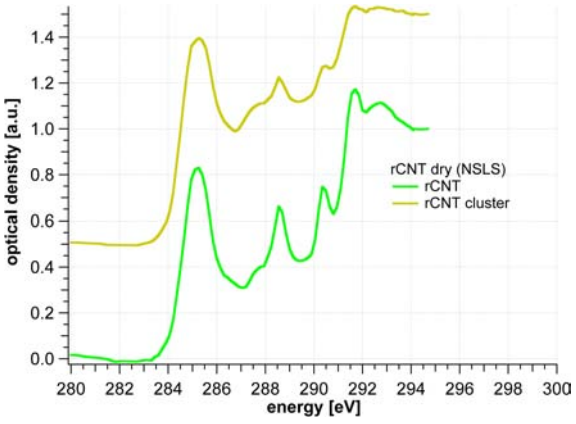

(c) *Plot of ROIs*

Figure 5.8: a) *High resolution x-ray micrograph of dry rCNTs (12.5 nm per pixel) with calibration bar of the photon counts.* **b)** *Composition of x-ray images of rCNTs in dry state (photon energy of 300 eV at NSLS, the highest sampling rate is 12.5 nm per pixel).* **c)** *The NEXAFS spectra, shifted for clarity, are obtained from the ROIs in* **b)** *marked in the corresponding color.*

The detector at the X1-A1 is a photon counter. Therefore, the largest high resolution

image of each sample is displayed with a calibration bar of the photon counts. For the composition images, if present, this was not done, because they are stitchings of multiple images with different sampling rates and taken at different times.
Fig. 5.8a and 5.8b demonstrate that the structure of the rCNTs has not changed. Still, long and flexible tubes are observed. The resonances at 285.3 eV and 291.5 eV are found again, too. Striking, however, are the two new peaks in the specta of the rCNTs. The peak at 290.5 eV was already indicated as a small shoulder in Fig. 5.4c and 5.5b. It is generated by defects in the bond structure of the CNTs [223]. Additionally, at 288.5 eV with a shoulder at 287.5 eV, resonances of the 1s → $\pi^*_{C=C}$, σ^*_{C-H} has emerged, possibly due to oxidation of the rCNTs during their storage. The ratio $\pi^*_{C=C}$:σ^*_{C-C} has changed, too; 0.81 for the cluster and 0.71 for the thinner regions, due to the more pronounced σ^*_{C-C} peak. In the thinner regions the peaks indicating defects and oxidization are less prominent, but on the other hand, in the spectral range between 286 eV and 289 eV there is generally more absorption. This strengthens the assumption made before that the rCNTs, if forced together, influence themselves.

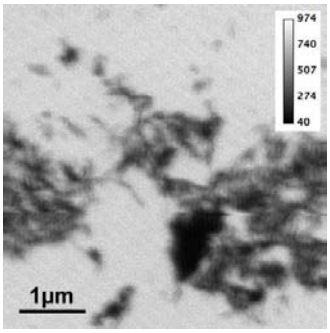

(a) *rCNTs, aqueous*

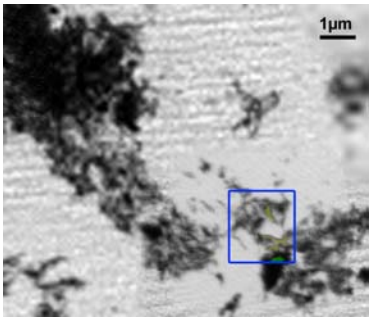

(b) *rCNTs, aqueous, with ROIs*

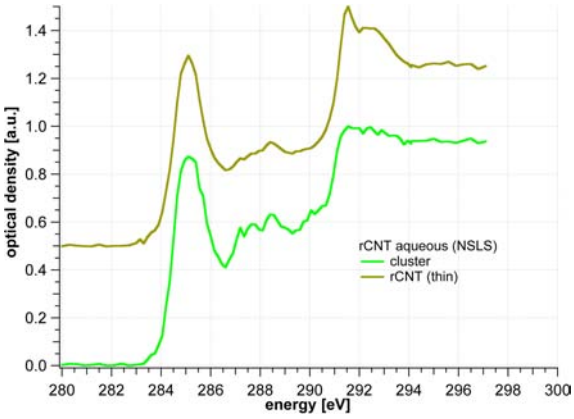

(c) *Plot of ROIs*

Figure 5.9: a) *High resolution x-ray micrograph of aqueous rCNTs (12.5 nm per pixel) with calibration bar of the photon counts.* **b)** *Composition of x-ray images of rCNTs in wet state (photon energy of 300 eV at NSLS, the highest sampling rate is 12.5 nm per pixel).* **c)** *The NEXAFS spectra are obtained from the ROIs in* **b)**, *marked in the same color.*

In wet state, clustering occurs again (Fig. 5.9a and 5.9b), indicating that the rCNTs are still hydrophobic, in spite of possible oxidization and protonation. The spectra in Fig. 5.9c exhibit similar features for thick and thin sample regions, and once more, the damping effect of the water on smaller resonances is found. This could also stem from the fact

that the water partly removes the O- and H-groups from the rCNTs, explaining why the resonances between 286 eV and 289 eV in the thick clusters are stronger than for the thin regions. The shift of the peak position of the $\pi^*_{C=C}$ resonance is to 285.1 eV in water is observed again, too. This time, the spectra of the rCNTs in wet state are much clearer, which could be a benefit of the more advanced technological standard of the X1-A1 microscope. The mCNTs for this experiments were newly prepared to ensure that the appearance of

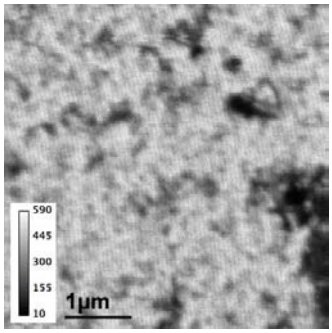

(a) *mCNTs, dry*

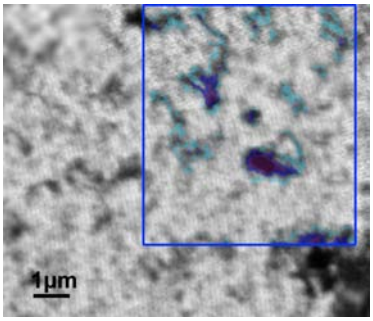

(b) *mCNTs, dry, with ROIs*

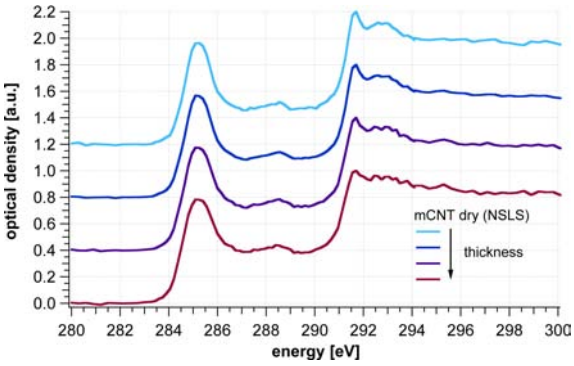

(c) *Plot of ROIs*

Figure 5.10: a) *High resolution x-ray image (12.5 nm/pxl, 300 eV, dwell time 1 ms) of mCNTs in dry state with calibration bar.* **b)** *Composition of x-ray images of the mCNTs (photon energy of 300 eV, smallest pixel size 12.5 nm).* **c)** *The NEXAFS spectra, shifted for clarity, are obtained from the ROIs in the respective image, marked in the same color.*

the resonances originating from the COOH-groups is not due to irregularities during the modification process. The second sample of mCNTs also shows strongly shortened CNTs, as depicted in Fig. 5.10a and 5.10b. In this case, however, no strong resonances at the spectral position of $\pi^*_{C=C}$ or σ^*_{C-H} are visible in the spectra, Fig. 5.10c. Again, a difference in the spectra is observed depending on the thickness of the corresponding ROI, but much weaker. For the thinner ROIs (light blue), the σ^*_{C-C} resonance at 291.5 eV and the following broader one at 292.5 eV are more pronounced, than for the thicker ROIs (purple). The $\pi^*_{C=C}$ peak is located at 285.1 eV and broader for thicker clusters. The ratio $\pi^*_{C=C}$:σ^*_{C-C} is only slightly smaller for thick clusters (0.78) than for the thinner ROIs (0.76), but the absorption level in the spectral range between both peaks is higher of the thick clusters (0.51) than for the thin parts (0.36), compared to the $\pi^*_{C=C}$ resonance.
In wet state, shown in Fig. 5.11a, the mCNTs again cluster, as expected from the experiments at BESSY II in Fig. 5.7a. It is also clearly visible that the mCNTs are not intact tubes any

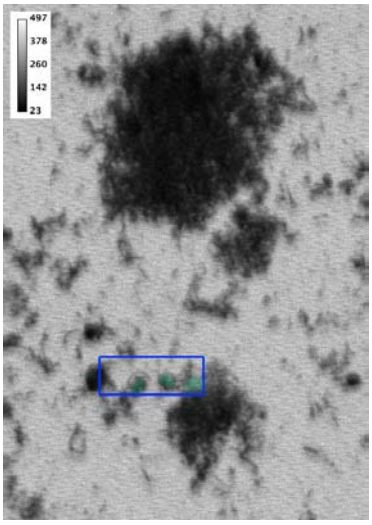

(a) *mCNTs, aqueous*

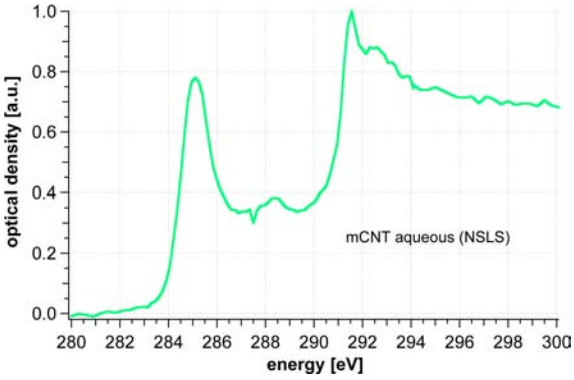

(b) *Plot of ROIs*

Figure 5.11: a) *Composition of x-ray images of mCNTs in wet state (photon energy of 300 eV, highest sampling rate 12.5 nm).* **b)** *The NEXAFS spectra are obtained from the ROIs in the respective images, marked in the same color.*

more. Here, no different spectra for different ROIs were observable (Fig. 5.11b), maybe due to the choice of the stack area, where the present clusters might not be thick enough. Once again, the spectrum shows the characteristic features of the CNTs observed before. The $\pi^*_{C=C}$ peak is located at 285.1 eV.

5.1.1.3 Discussion

In general, the structure of the CNTs did not change over time or whether measured in water or dry. Due to van der Waals forces and the so called hydrophobic effect, which originates from entropic effect within the system water, the hydrophobic CNTs cluster in aqueous environment.
Storage in water, although ultrapure, supposedly lead to defects in the structure, oxidation and protonation of the CNTs, as seen by comparison of Fig. 5.4 and 5.8. In wet state, however, the water seems to dissolve this debris. Furthermore, in aqueous environment the smaller resonances broaden and overlap, such that it seems as if they were not present. At the same time, the absorption between 286 eV and 290 eV is somewhat stronger than for dry CNTs.
Modification of the rCNTs yielded mainly shortened particles. Among the mCNTs only a few intact tubes are observable. The modification procedure was intended to bind COOH-groups to the mCNTs as may occur, if the rCNTs are exposed to environmental influences. According to Zaenker [220], it is not possible that the carboxyl groups detach from the mCNTs after the modification procedure. So it could be assumed that the carboxyl groups are turned towards the water, therefore, at the borders, they are more detectable.
In contrast, if it is assumed that the COOH-groups can detach from the mCNTs, another interpretation is conceivable. In that case, the carboxyl groups would be solved in water and re-attach to the mCNTs during the drying process, leading to a thin film at the borders

of mCNT clusters in Fig. 5.6b and 5.10a,b. This would explain the strong differences in the spectra of Fig. 5.6b. Likewise, the spectra in Fig. 5.10c could be explained by this thin film, covering the intermediate space and influencing the I_0-spectrum. Tests using other I_0 spectra, however, lead to similar results, i.e., no strong resonance around 288 eV. In wet state, detached carboxyl groups would be solved, which would also explain, why no resonance for $\pi^*_{C=O}$ is detected there (Fig. 5.7b and 5.11b).
A third interpretation is found, when comparing the spectra to NEXAFs spectra of amorphous carbon [193] or diamond-like carbon (DLC), which is a special form of amorphous carbon [223], shown in Fig. 5.12.

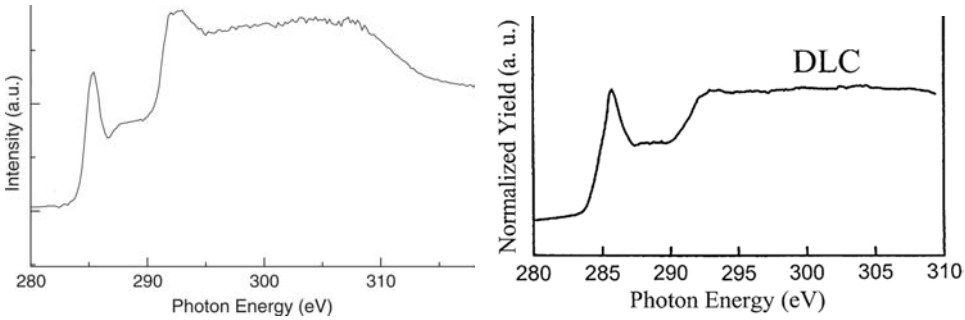

(a) *Amorphous Carbon* **(b)** *Diamond-like Carbon*

Figure 5.12: *NEXAFS spectra of* **a)** *amorphous carbon, adapted from Zhong et al. [223], Fig. 1a and* **b)** *diamond-like carbon (DLC), adapted from Tang et al. [193], Fig. 3.*

In particular, the spectra of the aqueous samples and of the mCNTs possess a similar spectral signature. Owing to changes in the vicinity of the carbon atoms, the chemical bindings in a sample are influenced, followed by an energy shift of the bindings. In a well-ordered sample, like the pristine rCNTs, this effect leads to observable peaks in the NEXAFS spectrum, as seen in Fig. 5.8c. If the changes are more unspecific, like the modification of CNTs or, e.g., amorphous carbon, the energy shifted peaks overlap, leading to a higher level of the absorption between 286 eV and 290 eV altogether, but no noticeable peaks.
For wet samples, the change at the borders of the clusters originates in the hydrophobicity of the CNTs [207]. This leads to the formation of a hydration cage. Due to this, the CNTs cluster, as observed in the measurements, and the C atoms are forced closer together, again with an effect on the chemical bond energies. This theory, however needs proof, as no comparable NEXAFS or XPS studies investigating the hydrophobic effect of CNTs in water could be found.
The experiments demonstrate that bulk measurements alone are not enough to characterize CNTs completely. Combination of spatial and spectral information draw a different picture of the samples than bulk measurements and REM images. A further change of the chemical environment of the CNTs is the binding of heteroatoms. Therefore, in the following section the sorption of the heavy metal uranyl (U VI) is studied and compared to the findings of Schierz and Zaenker [162].

Table 5.1: *Approximate energy positions and assignments of features in the C 1s NEXAFS spectrum. Data adapted from the literature [11, 12, 29, 35, 58, 110, 193, 223].*

position [eV]	1s → (orbital)	main character / origin
<285	$\pi^*_{C=C}$	shoulder, localized defects, compressed helicity
285.2-285.5	$\pi^*_{C=C}$	sp^2-hybridization
286-290		oxygenated surface and defects, hydrogenated C atoms
288.5	σ^*_{C-H}	surface associated defects, O containing functional groups from HNO_3/H_2SO_4 treatment
290.5	σ^*_{C-C}	localized defects, compressed helicity
291.5-291.7	σ^*_{C-C}	corresponding peak to sp^2-hybridized C rings
292.6	σ^*_{C-C}	shoulder, becomes broader with more defects

5.1.2 Effect of Uranyl (U VI)

Among other applications, CNTs could be used to filter heavy metals or toxicants from water, at what they would precipitate due to their hydrophobicity. On the contrary, it is also conceivable that in soils, a *Trojan Horse* effect could take place. In that case, CNTs would facilitate the transport of molecules bound to them. To investigate this, the sorption properties of CNTs need to be analyzed. Schierz and Zaenker [162] studied the sorption of uranyl (U VI) to the mCNTs, recording sorption isotherms to gain the amount of bound U VI. Here, these samples were also studied in dry and wet state with x-ray spectromicroscopy to see whether correlations between spectra and structural appearance are observed.

5.1.2.1 Sample Preparation

The samples were mCNTs loaded with 10 % respectively 40 % U VI, in the following called u10mCNTs and u40mCNTs. The percentages refer to equilibrium surface loading in $\frac{mg}{g}$ and was calculated as the difference between the equilibrium concentrations of the U VI solutions without, and with the mCNTs after centrifugation. For the sorption, U VI solutions of different contents ($10^{-7-5} \times 10^{-4}$M) were added to solutions of 1 $\frac{g}{l}$ mCNTs. The samples were then equilibrated for 48 hours and after that centrifuged for 1 hour at 170 000×g [162]. Since the samples were studied using the STXM at BESSY II, the sample preparation was analogous to the description in section 5.1.1.

5.1.2.2 Results

The recorded images and spectra of the dry u10mCNTs are depicted in Fig. 5.13. As clearly visible, even less intact tubes than in Fig. 5.6 and 5.10 are in the sample. Again different spectra for ROIs of different thicknesses are observed. The influence of U VI sorption is seen in two attributes. The transition peak for $\pi^*_{C=C}$ at 285.1 eV is very broad, but the ratio $\pi^*_{C=C}$:σ^*_{C-C} is still between 0.78 and 0.83. In the spectral region between 286 eV and

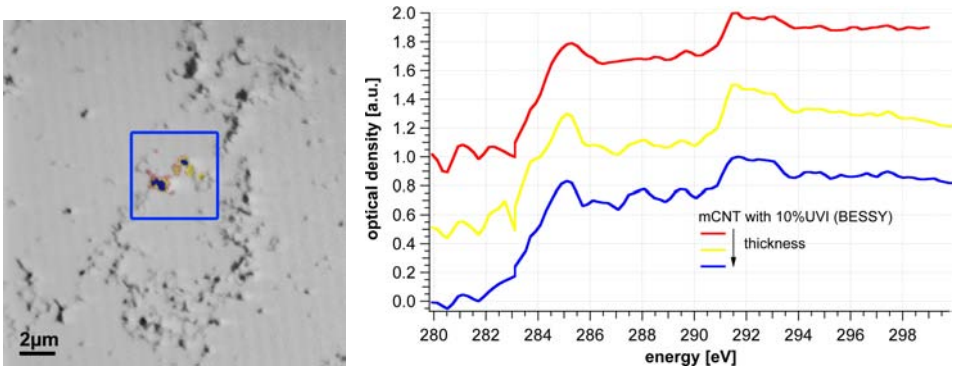

(a) *mCNTs with 10% U VI, dry* **(b)** *Plot of ROIs*

Figure 5.13: a) *Image of mCNTs loaded with 10% U VI in dry state (pixel size 50 nm, 6 ms dwell time, 300 eV), with framed stack area and color-coded ROIs.* **b)** *Plot in corresponding colors of the ROIs, shifted for clarity.*

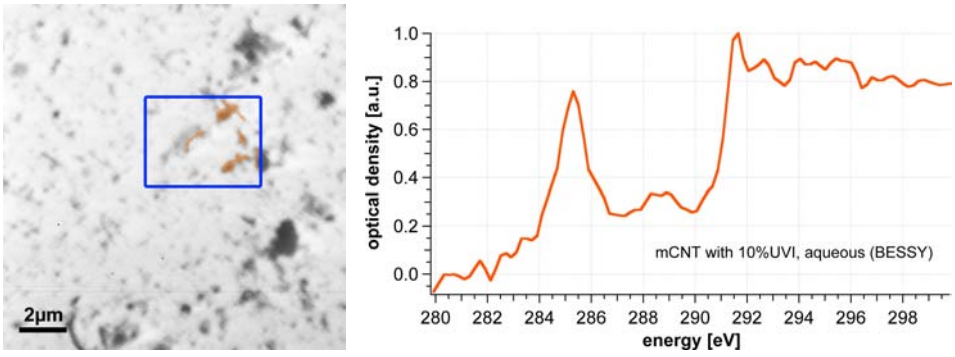

(a) *mCNTs with 10% U VI, aqu.* **(b)** *Plot of ROIs*

Figure 5.14: a) *Image of mCNTs loaded with 10% U VI in wet state (pixel size 100 nm, 6 ms dwell time, 300 eV).* **b)** *Plot of the u10mCNTs; the spectra of different ROIs all returned similar spectra.*

290 eV, however, strong absorption is recorded, even for the thin ROI marked in red.
In aqueous state, depicted in Fig. 5.14a, the u10mCNT form clusters, but it seems they are less dense than in Fig. 5.7a and 5.11a. A peak at 288.5 eV in Fig. 5.13b and Fig. 5.14b is visible, indicating that carboxyl groups are actually bound to the u10mCNTs and bind the U VI. Curiously, the $\pi^*_{C=C}$ peak is located at 285.3 eV.
For the u40mCNTs depicted in Fig. 5.15, the particulate character dominates even more. Here, no correlation between spectra and thickness of the ROIs is observed, rather, the different spectra in the ROIs 1, 2 and 3 seem to have no correlation apart from the location of the resonances $\pi^*_{C=C}$ (285.1 eV) and σ^*_{C-C} (291.5 eV and 292.5 eV), but even their shape differs strongly. Strong absorption at 288.5 eV is also observed, but the size these

resonances varies from $\pi^*_{C=C}$:σ^*_{C-C} 1.15 for ROI 3 to 0.61 for ROI 1.

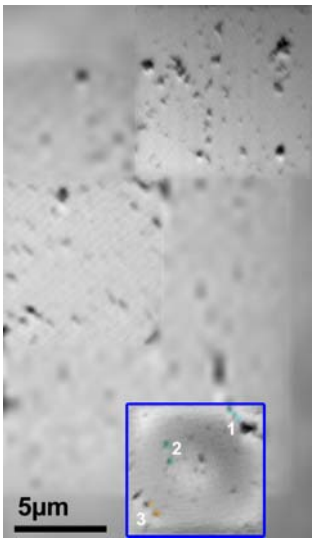

(a) *mCNTs with 40% U VI, dry*

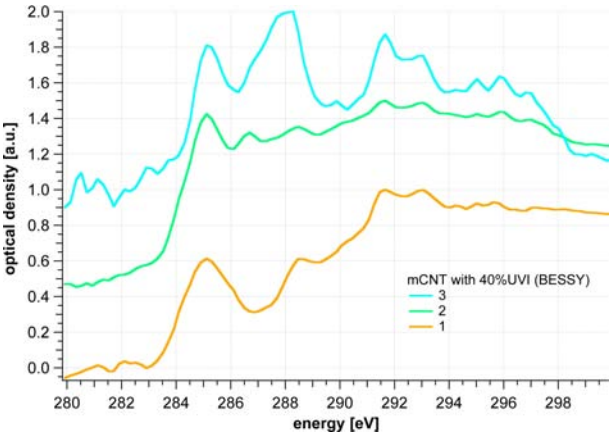

(b) *Plot of ROIs*

Figure 5.15: a) *Image of mCNTs loaded with 40% U VI in dry state (pixel size 50 nm, 6 ms dwell time, 300 eV), with framed of stack area and color-coded ROIs,* **b)** *plot in corresponding colors of ROIs, shifted for clarity.*

In the last experiment, the u40mCNTs were studied in aqueous environment. Clustering is visible, but maybe due to the strong particulate character and the chemical changes, also some smaller particles are visible in Fig. 5.16a. The spectrum in Fig. 5.16b shows similar

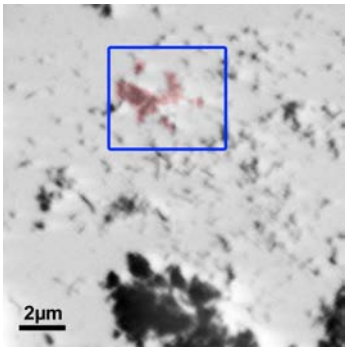

(a) *mCNTs with 40% U VI, aqu.*

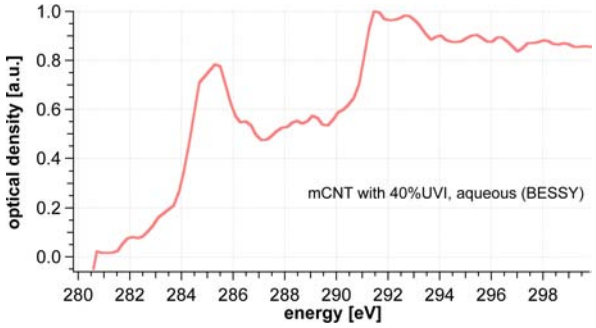

(b) *Plot of ROIs*

Figure 5.16: a) *Image of mCNTs loaded with 40% U VI in wet state (pixel size 100 nm, 6 ms dwell time, 300 eV),* **b)** *plot of the mCNT. No regions of different spectra were detected.*

characteristics as the spectra of the other wet state samples in Fig. 5.7b, 5.11b, 5.14b and also the rCNTs in Fig. 5.4c and 5.8c, but the intermediate spectral region (286 eV - 290 eV)

has a sightly stronger absorption, indicating more defects in the structure and only a very small resonance is found at 288.5 eV.

5.1.2.3 Discussion

The sorption of U VI to the mCNTs was verified recording sorption isotherms [162]. The strong influence on the mCNTs, however, becomes clear using x-ray spectromicroscopy as a method with spectral and spatial resolution. Especially at high concentrations of U VI, the effect on the mCNTs seems to be different depending on size, thickness and amount of attached functional groups. In wet state, the major peaks of the transitions to the $\pi^*_{C=C}$ and σ^*_{C-C} orbitals dominate again, strengthening the assumption that absorption from other transitions is leveled out, see section 5.1.1.3.
Whether these CNTs are a good means for the filtering of water needs more studies, as it is clear that they behave differently in dry and in wet state. Comparing these measurements to the ones with the pristine rCNTs and mCNTs, one can conclude that functionalization of the CNTs is achieved, although some of the interacting sites may not necessarily be carboxyl groups. They could aswell be due to defects in the structure of the CNTs resulting from the modification procedure.
Thus, the scenario of CNTs acting as transport facilitators in soils for heavy metals is at least conceivable. Currently, the use or harm due to binding of toxicants to CNTs in water or soil is not particularly relevant, because of the small amounts of nanomaterials in the environment. Nevertheless, the investigation between the interaction of CNTs and soil particles is therefore an important issue and is discussed in section 5.2.

5.2 CNTs and Interaction with Soils

What happens if CNTs are brought into contact with other substances - is it possible to distinguish them from matter of high carbon content? With the increasing use and production of these newly designed materials, the ecological aspect comes into account, too, and reliable ways to study and characterize the interaction between CNTs and other substances have to be found.
Although several experiments concerning the effect of CNTs on tissue and cells [111, 177] have been published, only few attend to the effects on soils and humic substances [138, 158]. Pristine CNTs are mainly chemically inert, which prevents them from being biodegraded; therefore, it is important to analyze their (long-term) effects on the environment.
X-ray spectromicroscopy has been applied to CNTs before [11, 12, 58, 110, 193, 223], but only under special laboratory conditions, such as high temperatures or high vacuum. For the experiments reported in the following [167], the multi-walled CNTs studied in section 5.1 (outer diameter of 10 nm - 30 nm and a length distribution of 0.5 μm - 2 μm) [162] were used and studied under ambient conditions.

5.2.1 Materials and Methods

Samples Preparation of the samples was analogous to the description in section 5.1.1. A gleyic chernozem from an A_h horizon (German taxonomy: Schwarzerde, from Rosdorf near Göttingen, Germany) [4, 161] was used as soil sample. It has been studied with x-ray spectromicroscopy [63, 123] and other methods before [96]. Humic substances (HS) were extracted from the chernozem using Na-pyrophosphate (pH = 7.0). For the samples comprising of CNTs and chernozem or HS of chernozem respectively, a solution of 90 % water, 9 % chernozem or HS and 1 % CNTs (volume fractions of 1 % standard solutions) was established in a glass vessel. Before further preparation, all sample solutions were ultrasonicated for several minutes. The pH-vaue of all sample solutions was 7.

Analysis and instrumentation The preliminary imaging experiments were conducted using the STXM at BESSY II. For the main part of the experiments images and stacks were recorded with the X1-A1 microscope at NSLS. The analysis, i.e., alignment and selection of the ROIs, was again done using the programs *stack_analyze* and *pca_gui*, which were actually written to process the data recorded at X1-A1 [93, 118].

5.2.2 Results

For the comparison to pure samples, only the measurements of the pristine rCNTs and mCNTs recorded at the NSLS are used, see Fig. 5.8, 5.9, 5.10 and 5.11 in section 5.1. At the end of the results section, Tab. 5.2 lists the energy positions for resonances that are important for the transitions observed in the following experiments.

Preliminary experiments As a first step, images of the rCNTs and the mCNTs, added to a 1 % dispersion of montmorillonite clay minerals, were recorded.
The dispersion of rCNTs resp. mCNTs is imaged well above the C 1s absorption edge at 300 eV (Fig. 5.17a resp. 5.17d) and at 280 eV, below this edge (Fig. 5.17b resp. 5.17e). In the ratio of the image intensities $\frac{I_{300\,\mathrm{eV}}}{I_{280\,\mathrm{eV}}}$ (Fig. 5.17c resp. 5.17f), the CNTs and their distribution are clearly discernable. The clay particles do not have an organic component; therefore, the CNTs can be identified in the mixture using elemental mapping as shown in Fig. 5.17. To gain more detailed chemical information, x-ray spectromicroscopy is used in the following.

rCNTs and humic substances Exemplarily, a well characterized chernozem [63, 123, 197] has been used as a soil sample. As a first experiment, the HS fraction of chernozem was mixed with CNTs and imaged in dry conditions, depicted in Fig. 5.18.
In Fig. 5.18a and 5.18b, the dispersed rCNTs are partly discernible owing to their unique morphology. As the inset demonstrates, the visibility is even better, if images taken at the photon energies 285 eV and 288.5 eV are subtracted from each other. Since the HS exhibit a peak of similar height at both energies, it levels out in comparison to CNTs. To identify the suitable energies for this kind of mapping, it is necessary to know the complete spectrum. The NEXAFS spectra of three different groups of ROIs are displayed in Fig. 5.18c. These areas have been selected as they show spectra stemming mainly from rCNTs, HS or interfacial regions, respectively. For comparison, the spectrum of the pure dry rCNTs from

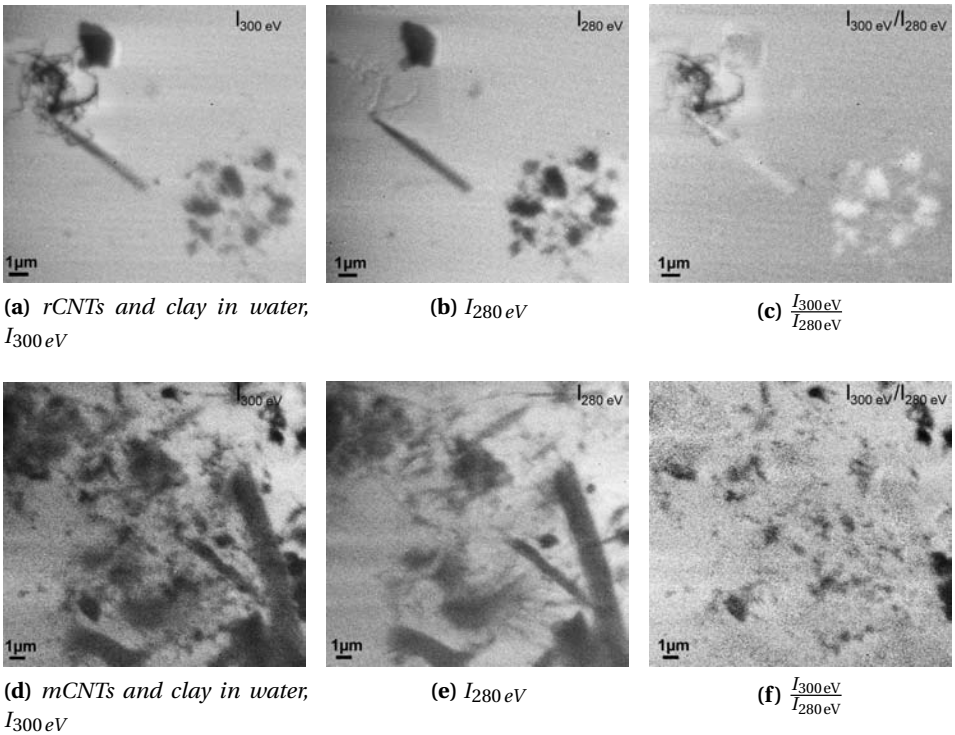

(a) *rCNTs and clay in water,* $I_{300\,eV}$ **(b)** $I_{280\,eV}$ **(c)** $\frac{I_{300\,eV}}{I_{280\,eV}}$

(d) *mCNTs and clay in water,* $I_{300\,eV}$ **(e)** $I_{280\,eV}$ **(f)** $\frac{I_{300\,eV}}{I_{280\,eV}}$

Figure 5.17: *X-ray micrographs of CNTs dispersed with clay in wet state; smallest pixel size 50 nm at BESSY II, dwell time 6 ms.* **a)-c)** *rCNTs with montmorillonite at* **a)** *300 eV,* **b)** *280 eV and* **c)** *the ratio of the intensities of both images.* **d)-e)** *mCNTs with montmorillonite at* **d)** *300 eV,* **e)** *280 eV and* **f)** *the ratio of the intensities of both images.*

Fig. 5.8 is also plotted in the upper graph (dotted line).
In relation to the respective edge jump, the height of the peaks at 285 eV (1s → $\pi^*_{C=C}$) and at 291.5 eV (1s → σ^*_{C-C}) is smaller than for the pure rCNTs. The spectral region between those two energies is on a lower level for the mixed rCNTs. The transition peak 1s → $\pi^*_{C=C}$ is shifted ca. 0.4 eV to lower energies. This difference is well above the resolution of the STXM and therefore no artifact.
The spectrum of the area covered with HS is displayed in the middle graph. It shows the expected transition peaks [164]: aromatic 1s → $\pi^*_{C=C}$ at 285 eV, phenolic 1s → $\pi^*_{C=C}$ at 286.5 eV, carboxylic 1s → $\sigma^*_{C=O}$ at 288.5 eV and a rise resulting from the 1s → $\sigma^*_{C\text{-}C,C\text{-}O}$ transitions starting at 290 eV. The graph at the bottom of Fig. 5.18c displays spectral features of both types of organics. The weighted superposition of the rCNT and the HS graph is also plotted (red line). By simply adding the spectra of both organics in a 1:1 ratio, the spectrum of this interfacial region can be reproduced.

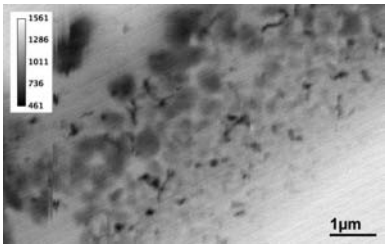

(a) *rCNTs + HS, dry, with ROIs*

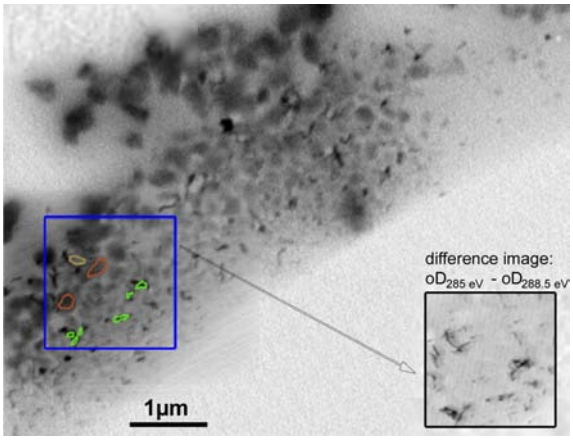

(b) *rCNTs + HS, dry*

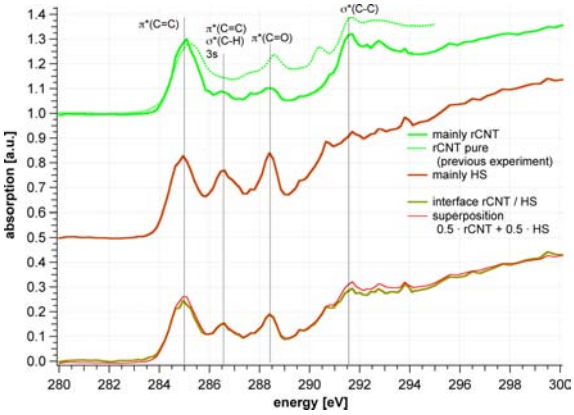

(c) *Plot of ROIs*

Figure 5.18: a) *High resolution image of rCNTs dispersed in the HS of chernozem (12.5 nm pixelsize) with photon counts.* **b)** *Larger image of rCNTs assembled by eight smaller x-ray micrographs. The inset shows the difference in optical density (oD) of the framed area recorded at 285 eV and 288.5 eV (corresponding images are not shown). This area was also used for recording a stack, the ROIs are indicated, too.* **c)** *Spectrum of the ROIs marked in* **a)**, *shifted for clarity. For comparison, the spectrum of the pure dry rCNTs from Fig. 5.8c is plotted, too (green dotted line). Also, the superposition of the rCNTs and the HS is plotted in the lower graph (thin red line).*

CNTs and soil in dry state The experiment of CNTs dispersed in the chernozem soil, opens a broader scope of possible mutual interactions. Again, dry samples were studied first, shown in Fig. 5.18 and Fig. 5.19. The insets in Fig. 5.18a and 5.19a show a color-coded image stack of the areas that were studied with x-ray spectromicroscopy.
For the dispersion of rCNTs and chernozem (Fig. 5.18a), the main components can be discriminated as rCNTs, clays, and organic compounds. Clay minerals are marked in blue/purple, organic rich parts in dark yellow, and the rCNTs in green. The corresponding spectra are shown in Fig. 5.18b using similar colors. The spectrum of the rCNTs is recognizable from the resonances at 285 eV and 291.5 eV and the dip between them.
In the spectrum of the organic soil compounds, the resonance peak at 286 eV is not present. The clay particles can be distinguished by their high peaks at the K $L_{III,II}$ absorption edges. The spectra of the interfaces between rCNTs and the soil particles exhibit features of the rCNTs and the soil. This includes the peaks of the K $L_{II,III}$-edges of the clay, the broad

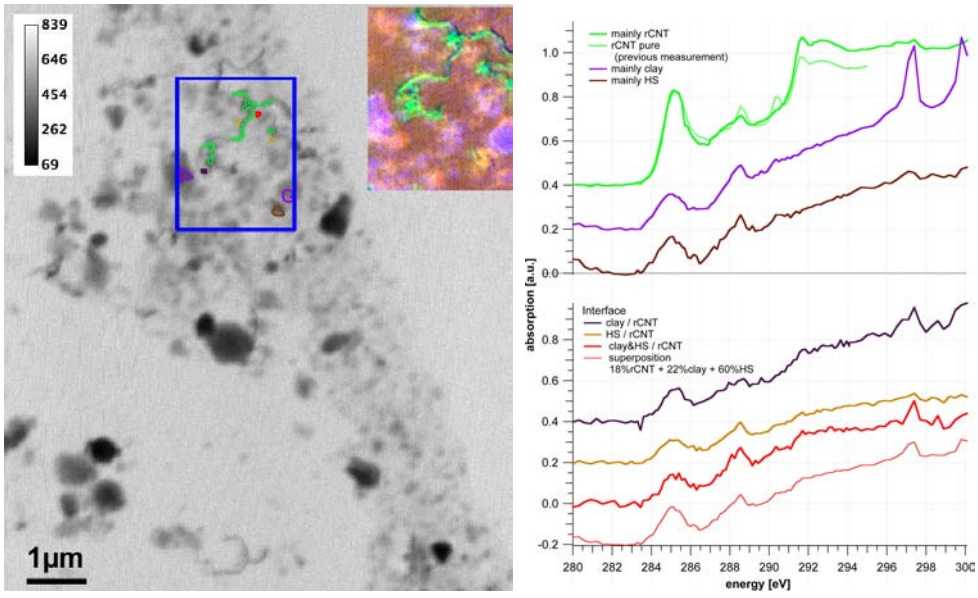

(a) *rCNTs + soil, dry* **(b)** *Plot of ROIs*

Figure 5.18: *X-ray micrographs and NEXAFS spectra of a mixture of rCNTs and soil colloids in dry state recorded using the STXM at beamline X1-A1 at the NSLS (300 eV, smallest pixel size 12.5 nm).* **a)** *Composition of x-ray micrographs of rCNTs and chernozem. The inset displays an RGB-stack of the area used for the image stack. It was obtained from the images taken at 285.5 eV, 288.5 eV and 291.5 eV, normalized with an image at 283 eV. rCNTs appear green, clay particles in purple, areas high in organic carbon in dark yellow.* **b)** *Spectra of the regions marked in* **a)**, *shifted for clarity.*

transition peak at 285 eV of the HS and the rCNTs, the peak of the carbonyl or carboxyl groups (288.8 eV), and the rise at 290 eV of the transitions 1s→ $\sigma^*_{C\text{-}C}$, $\sigma^*_{C\text{-}O}$ stemming from the HS, and the step in the spectra at 291.5 eV, again from the rCNTs.
A weighted superposition of the single components yields a similar spectrum (thin red curve in Fig. 5.18b). For comparison, the spectrum of the pure dry mCNTs (Fig. 5.10c) is plotted as dotted line in Fig. 5.19b, too. In all spectra in Fig. 5.19b, the transition peaks of $\pi^*_{C=O}$ (~ 288 eV) and $\sigma^*_{C\text{-}C}$ (290.4 eV) are prominent. The spectra of the mCNTs and the respective inset in Fig. 5.19a make clear how difficult it is to retrieve the mCNTs here. Due to their small size, they can hardly be distinguished from the organic constituents of the soil. The last plot is again a superposition of the single component spectra, mCNTs, clay and HS.

CNTs and soil in wet state The studies of the same dispersion of CNTs and soil in a wet state is shown in Fig. 5.20 and Fig 5.21.
The rCNTs in Fig. 5.20a again form clusters. The spectra of the rCNTs taken from the thicker part of the cluster do not show a pronounced peak at 291.5 eV and a subsequent decrease

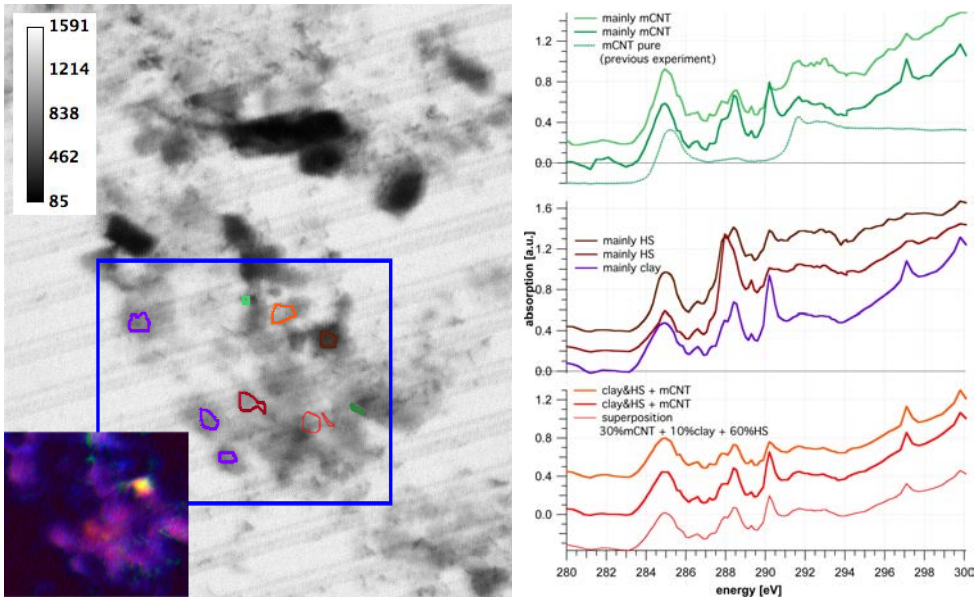

(a) *mCNTs + soil, dry* **(b)** *Plot of ROIs*

Figure 5.19: *X-ray micrographs and NEXAFS spectra of a mixture of mCNTs and soil colloids in dry state (300 eV, 12.5 nm pixel size).* **a)** *The mCNTs dispersed in chernozem. The RGB-stack in the inset was obtained from the images taken at 285.5 eV, 288.5 eV and 290.5 eV, normalized with an image at 283 eV. It illustrates how difficult it is to retrieve the mCNTs, due to their small size.* **b)** *NEXAFS spectra of the ROIs, shifted for clarity.*

at higher energies, but rather level off in a plateau. Two main spectra of the soil particles could be verified, referred to as HS1 and HS2 in the spectra. The RGB-stack in Fig. 5.20b shows the rCNTs in green, HS1 in blue and HS2 in magenta. Interfaces between rCNTs and chernozem colloids show different NEXAFS spectra (lower graph in Fig. 5.20d), and can no longer be approximated by a superposition of the interacting rCNTs and soil colloids (red graph plot).

In case of the mCNTs, it was not possible to record a stack and gain spectroscopic information in aqueous composition, because during the experiment the very small mCNTs could not be retrieved among the soil particles.

In the analysis process subsequent to the actual experiment, when comparing images below and above the C K-edge (arrows in Fig. 5.21c), some mCNTs were identified. Such images and their difference are displayed in Fig. 5.21. Especially the difference image makes clear how small the mCNTs are after the chemical modification. Due to this small size they more readily interact and mix better with the soil particles than the rCNTs.

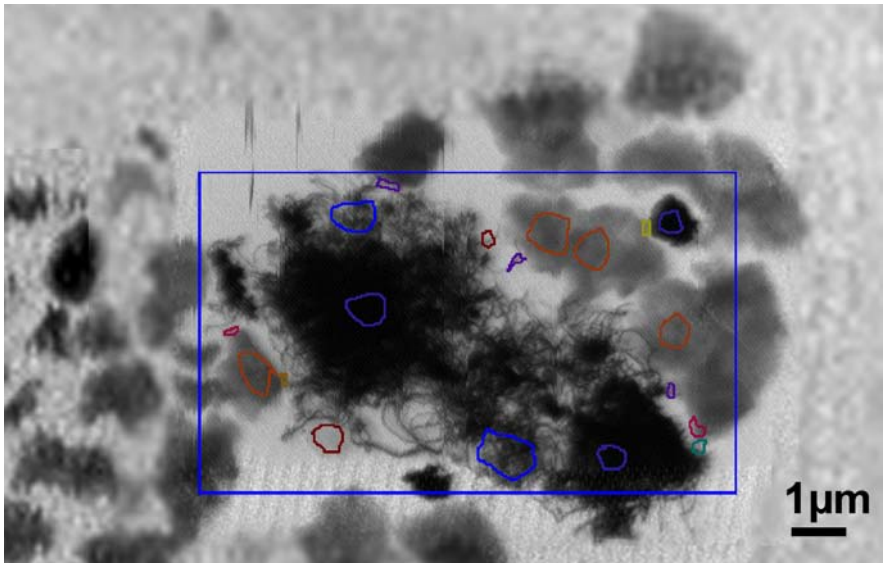

(a) *rCNTs + soil, aqueous*

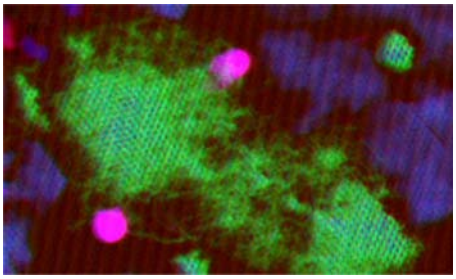

(b) *rCNTs + soil, aqueous, with ROIs*

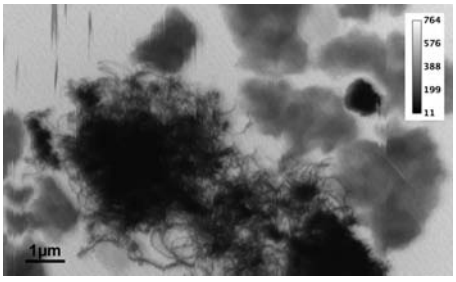

(c) *rCNTs + soil, aqueous, with ROIs*

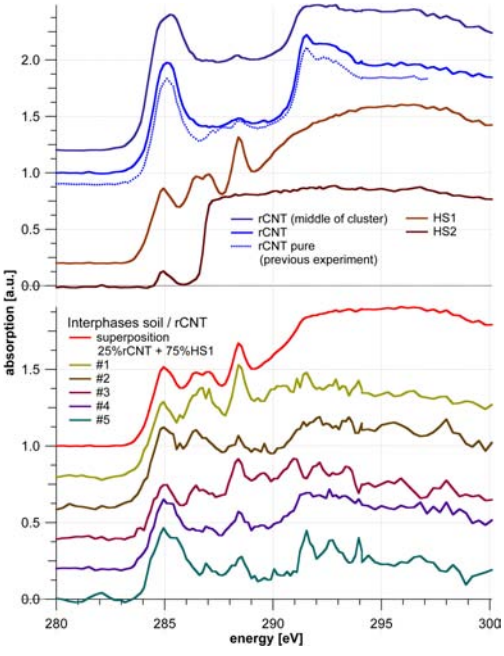

(d) *Plot of ROIs*

Figure 5.20: *rCNTs and soil in aqueous state.* **a)** *Collage of x-ray micrographs of rCNTs and chernozem with the ROIs displayed.* **b)** *RGB-color stack of the stack area is shown that helps to identify the different ROIs; rCNTs appear green, the soil particles have mainly two different spectra and appear in blue (HS1) and magenta (HS2).* **c)** *High resolution micrograph (12.5 nm per pixel) with a calibration bar of the photon counts.* **d)** *Spectra of the ROIs marked in* **a)**, *shifted for clarity.*

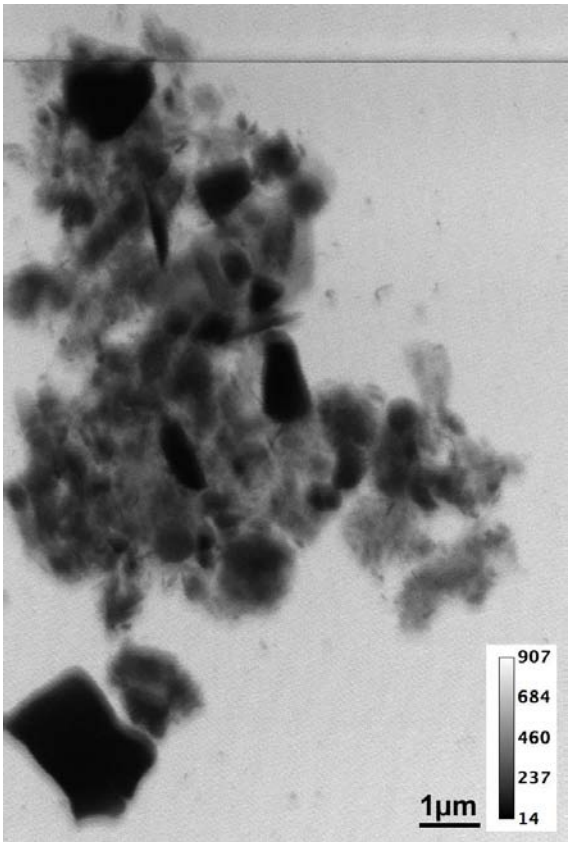

(a) *mCNT + soil, aqu.,* $I_{300\text{eV}}$

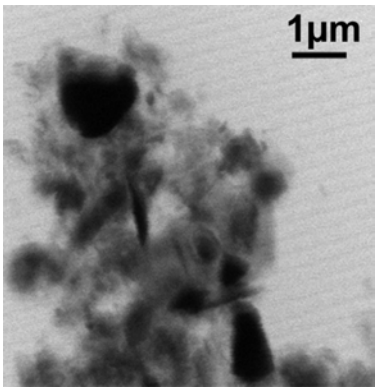

(b) $I_{280\text{eV}}$

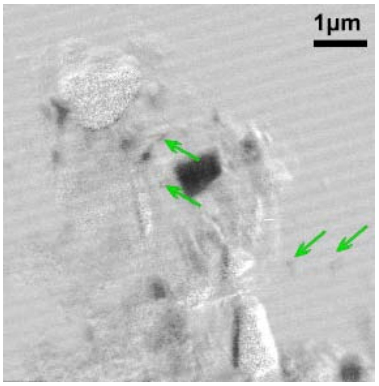

(c) $\frac{I_{300\text{eV}}}{I_{300\text{eV}}}$

Figure 5.21: *Elemental mapping of the mCNTs and soil in aqueous state.* **a)**-**c)** *mCNTs dispersed in chernozem at* **a)** *285 eV,* **b)** *280 eV and* **c)** *the difference of both images (12.5 nm pixel size). Green arrows mark mCNTs, which are better visible in* **a)**, *but from this image alone it can not be distinguished from a soil colloid.*

5.2.2.1 Discussion

CNTs in a dry state have been the subject of many studies, however, little has been done so far with aqueous samples, as these are much more difficult to investigate. This is due to the more elaborate sample preparation, movement of the particles within the dispersion and the inability of the most techniques to look into an aqueous medium. Using a STXM, CNTs are retrievable in aqueous dispersions even with other colloidal substances.
The experiments with pure rCNTs and mCNTs reported in section 5.1 show that the modification process has not only functionalized, but also significantly shortened the rCNTs. But the characteristic peaks at 285 eV and 291.5 eV peaks allowed for distinguishing the CNTs from the soil particles, because they are characteristic for these CNT samples.

The experiment with rCNTs and HS (Fig. 5.18) demonstrates that the rCNTs are discernible from organic soil particles . Additionally, they show that the rCNTs tend to mix with the HS, owing to their size in the same range as the HS soil colloids. But even more important, the HS stabilize the rCNTs [40, 86, 162], leading to better mixing than for rCNTs dispersed in the colloidal fraction of the chernozem. Comparison with the spectra of the pure rCNTs shows that the signature has not changed severely. This implies that the rCNTs and the HS do not seem to interact chemically at the interface in dry state any more. A closer look reveals that the NEXAFS spectrum of the rCNTs dispersed in HS exhibits differences in the spectral region between 285 eV and 291 eV, too. These differences might however be due to the limits in spatial resolution, since also HS particles with sizes smaller than 30 nm, the resolution limit of the zone plate, occur in the sample and interfaces are not always distinguishable. Thus, it is possible to calculate the spectra at the interfaces as superpositions of the characteristic spectra of HS and rCNTs at this stage, as shown in the last plot in Fig. 5.18c.
The dry dispersions of rCNTs and soil in dry state in Fig. 5.18 also show only few chemical interactions between the soil colloids and the rCNTs. Thus, the superposition of the spectra of the single components yields a similar spectrum as the one measured at the interfaces. In the x-ray micrographs, it can be observed how well the rCNTs mix with the soil particles, even coiling around them. The spectrum of the organic compounds does not resemble the one plotted in Fig. 5.18c which could be a result of the extraction process. Again, it is possible to reconstruct the spectrum at the interfaces of rCNTs with soil particles by a superposition of the single spectra.
The dry sample of mCNTs and soil yields spectra with a very outstanding peak at 290.4 eV, depicted in Fig. 5.19. At this energy, the transition 1s $\rightarrow \sigma^*_{\text{C-H}}$ for aliphatic compounds is located, indicating how the particles might interact. Although the modification does no longer appear in the spectra of the pure mCNTs, it obviously influences their interactions with the soil particles. Consequently, the mCNTs mix much stronger with the soil than the rCNTs. The spectra of the mCNTs hint that the mCNTs bind to the soil particles via carboxyl or carbonyl groups due to aforementioned 1s$\rightarrow \pi^*_{\text{C=O}}$ and via C-C bonds, which can be concluded form the peak at 290.4 eV (1s$\rightarrow \sigma^*_{\text{C-C}}$, non-aromatic), see Tab. 5.2.
It is also noticeable that the aromatic peak at 285 eV is shifted to lower energies, in comparison to the pure dry mCNTs. Due to their small size, it is difficult to distinguish the mCNTs in the x-ray micrographs. Therefore, pure spectra of the mCNTs could not be detected, because their spectrum overlaps with the spectrum of the nearby soil colloids. The spectra of mainly mCNTs, HS clay and their superposition do not differ significantly, apart from the heights of the peaks, but the same peaks are present in all spectra in Fig. 5.19b. Without high resolution spatial information, it would therefore not be possible to detect the mCNTs in such condition. The results of this experiment show that not only do the mCNTs interact with the soil particles, but they seem to affect the chemical environment of the whole sample. Of course, such high fractions of CNTs in soil are not realistic, but waste on the other hand does not spread homogeneously either.
In the experiment of rCNTs and soil in wet state the clustering is observed again (Fig. 5.20a), but the rCNTs are attached to the organic soil colloids. Since HS only make up about 4 % of chernozem is comprised of HS [161], a stabilization effect as in Fig. 5.18 is not observed. The fact that the spectra of the soil are different in aqueous and in dry state has already

been reported [63]. No clay particles are observed close to the cluster. In the middle of these clusters, the spectrum (Fig. 5.20d) has a smaller peak at 291.5 eV and the peak at 285 eV is broader. This has also been observed for the pristine rCNTs in Fig. 5.9. At 280 eV, the cluster is completely transparent which argues against saturation as the reason for the slightly different spectrum inside dense clusters. Rather, the rCNTs forced closely together influence each other.
In water, the rCNTs seem to interact even chemically with the soil particles, which becomes clear when looking at the spectra of the interfacial ROIs. One possible explanation could be that the surrounding water changes the chemical situation for the components in the sample, e.g., by diffusion of ions or small particles. Now, simple superposition of the spectra of the single components does not reproduce the spectra of these regions. The mCNTs depicted in Fig. 5.21a and 5.21b are only visible using elemental mapping (Fig. 5.21c), because they are integrated into organic soil particles. For a detailed conclusion, more elaborate measurements are necessary.

Table 5.2: *Approximate energy positions and assignments of features in the C 1s NEXAFS spectrum. Data adapted from the literature [11, 29, 31, 42, 44, 58, 123].*

position [eV]	1s → (orbital)	main character
284.5 - 285.5	$\pi^*_{C=C}$	quinones, aromatic
285 - 285.3	$\pi^*_{C=C}$	CNTs (sp^2-hybridization)
286 - 286.8	$\pi^*_{C=C}$	phenolic, ketonic
~ 287	σ^*_{C-H}, 3p	carbohydrates, alkyl
288 - 288.5	$\pi^*_{C=O}$	carbonyl (peptide bonds), ketonic
288-289	$\pi^*_{C=O}$	carboxyl, carbonate
~ 289.5	σ^*_{C-H}, 4p	O-alkyl
289 - 290.5	σ^*_{C-X}	X: N, S, F, P
> 291		peaks in general broader, more overlap
291.5	σ^*_{C-C}	CNTs
292 - 293	σ^*_{C-C}	aliphatic
293-295	σ^*_{C-C} σ^*_{C-O}	aromatic, phenolic, carboxyl, carbonyl
297.4	K L_{III}	potassium
299.7	K L_{II}	potassium

5.2.3 Recapitulation

The results confirm that x-ray spectromicroscopy makes it possible to identify and retrieve CNTs dispersed in dry as well as aqueous soil samples. It was difficult to compare the findings with other experimental results, because no other studies of CNTs in wet state and/or in contact with soil matter, using x-ray spectromicroscopy, could be found in the

literature.
Weathered or functionalized CNTs maybe shortened, degraded, or modified in other ways – therefore, they cannot be identified unambiguously by their morphology alone or from spectra of bulk measurements. Modifications might be intentional chemical alterations, but can also be the result of time and environment, as was also shown. With x-ray spectromicroscopy, the CNTs could not only be imaged by means of elemental mapping, but interfacial reactions could as well be analyzed by NEXAFS spectroscopy. Not surprising, the experiments showed that the interaction between CNTs and the environment becomes more complex with increasing complexity of the environmental structures. It could be demonstrated that until a certain point the chemical and physical reactions can be explained by taking into account all involved specimens at the interface, but as soon as water (or another solvent) is added, these simple relations cannot be applied any more. This has been illustrated by calculating the superpositions of the single components involved in the interactions.
As a first step towards the interpretation of the effect of CNTs on naturally occurring soil samples, the sterical and chemical interactions between the CNTs and the soil colloids was shown. Both could be observe with the rCNTs, too, which originally should have been chemically inert.
To further determine these interactions, 3D techniques such as stereo x-ray microscopy proposed by Gleber et al. [68] or x-ray micro-tomography [78, 196] would be useful to study the spatial arrangement of these colloidal samples and to reveal their morphology.

5.3 Alternative Analysis Approach: Constrained Optimization

The analysis of x-ray spectromicroscopic experiments with different substances of similar chemical composition and therefore spectral signature is challenging. *stack_analyze* [94], the program used here, allows for chosing the reference spectrum I_0 and ROIs by hand, alternatively I_0 can be gained by choosing the brightest pixels from the intensity spectrum (number of pixels versus intensity) of the stack, which automatically should yield the spectra of the regions on the Si_3N_4-membrane without sample. The recognition of ROIs is facilitated by using the program *pca_gui* [118]. This program combines two algorithms: Firstly, the spectra and images are decomposed into abstract eigenspectra and eigenimages using principle component analysis (PCA). Secondly, clusters within the data points of the eigenspectra are obtained using cluster analysis (CA). Albeit, I_0 has to be acquired before from *stack_analyze*.
PCA in combination with CA has a disadvantage: The obtained components are orthogonal, which might not be the best way to span the space of the data points and furthermore not the physical representation. False determination of the components leads to wrong results from the CA. In this section, constrained optimization (CO) is tested as an alternative approach to find the components in the stack area. The Lambert-Beer law forms the basis of the CO, and one major benefit is that I_0 is gained for every pixel as background component. This part of the work was done in cooperation with T. Hotz (Institute of Mathematical Stochastics, Georg-August-university Göttingen), who provided the mathematical expertise.

In the following, PCA is shortly explained to get a rough understanding of the algorithm. Afterwards, CO is described together with a new way of image alignment. The test samples used here are the pristine rCNTs, shown in Fig. 5.8, perfectly suited for that purpose because of their unique and uniform spectrum.

5.3.1 Principal Component Analysis (PCA) and Cluster Analysis (CA)

The principles of PCA and CA are described here, based on Lerotic et al. [118], Osanna [136] and Lerotic [117], a detailed documentation of PCA is for example given in Jolliffe [100].
The data set obtained from a stack of images of a spectromicroscopic experiment has two parameters. The intensity I depends on the pixel position (x, y) of the image area and the energy E. If the reference intensity I_0 is defined, the data can also be written in terms of the optical density

$$oD = -\ln\left(\frac{I(x,y,E)}{I_0(x,y,E)}\right) = \mu(E)\,t(x,y)\,, \tag{5.1}$$

according to the Lambert-Beer law, Equ. (2.1). If the pixels are indexed by consecutive numbers $p = 1,\ldots,P$, the energies E_n by $n = 1,\ldots,N$, and $s = 1,\ldots,S$ spectroscopically different components are assumed to be present in the sample the data can be expressed as

$$oD_{np} = \mu_{n1}\,t_{1p} + \mu_{n2}\,t_{2p} + \cdots + \mu_{nS}\,t_{Sp} = \sum_{s=1}^{S} \mu_{ns}\,t_{sp}\,, \tag{5.2}$$

or as the matrix

$$oD_{N\times P} = M_{N\times S}\cdot T_{S\times P}\,. \tag{5.3}$$

If all components were known, a thickness map of the sample area could be drawn. But for most environmental or biomolecular samples this is not the case. The goal of PCA is, to describe the data by a set of abstract components $s = 1,\ldots,N$ and then to reduce the number of spectroscopic components to a subset $s' = 1,\ldots,\overline{S}_{abs}$ that fully describes the data.
Instead of the physical matrices $M_{N\times S}$ and $T_{S\times P}$, it is convenient to express oD in terms of a column matrix $\mathrm{C}_{N\times N}$ and row matrix $\mathrm{R}_{N\times P}$; each column of $\mathrm{C}_{N\times N}$ contains a spectrum (of N points), each row of $\mathrm{R}_{N\times P}$ contains an image (of P pixel positions):

$$oD_{N\times P} = C_{N\times N}\cdot R_{N\times P}\,. \tag{5.4}$$

Obviously, it is easier to calculate the spectrum matrix $C_{N\times N}$, since the number of pixel points P is larger than the number of spectral points N. $C_{N\times N}$ is obtained via the spectral covariance

$$Z_{N\times N} = oD_{N\times P}\cdot oD^{T}_{P\times N}\,. \tag{5.5}$$

With $Z_{N\times N}$, the *eigenspectra*, i.e., the eigenvectors of $C_{N\times N}$ are computed,

$$Z_{N\times N}\cdot C_{N\times N} = C_{N\times S_{abs}}\cdot \Lambda_{N\times N}\,, \tag{5.6}$$

with $\Lambda_{N\times N}$ a diagonal matrix where the elements are the eigenvalues λ_s. This leads to an orthogonalized eigenspectra matrix $C_{N\times N}$ of eigenspectra. The matrix of *eigenimages*

$R_{N\times P}$ is then computed by $R_{N\times P} = C^T_{N\times N} \cdot oD_{N\times P}$.
Sorting the matrix entries with respect to the largest values has the effect that eigenspectra are sorted in decreasing order of the corresponding eigenvalues. Then, the first eigenspectrum is the average of the spectra of all pixels, the first eigenimage shows roughly a map of the sample thickness. Since $C_{N\times N}$ and $R_{N\times P}$ are orthogonal, the second eigenspectrum is the first order correction to the first eigenspectrum, which is the strongest deviation of the first eigenspectrum. The third eigenspectrum is the correction to the second and so on. For the eigenimages, similar relations apply. After a few corrections, the eigenspectra and eigenimages only show statistical noise. A subset of significant components $S_{abs} < N$ can be determined that fully represents the meaningful features of the data, yielding a reduced version of the data matrix,

$$oD^{red}_{N\times P} = C_{N\times S_{abs}} \cdot R_{S_{abs}\times P}\,. \tag{5.7}$$

This reduced data matrix is then analyzed with CA. Groups of pixels with similar spectra are searched in the eigenimage matrix $R_{S_{abs}\times P}$. The aim is to find clusters of data points with minimal distance within but maximal distance between them. As the CA algorithm is used after the PCA, it is not regarded in greater detail here, since the issues that are important for testing a new approach are already found in the PCA.

5.3.2 Constraint Optimization (CO)

For PCA, the eigenspectra have to be orthogonal, therefore, an abstract set of components has to be found and then retransferred to physically meaningful components of M and T. If M and T were orthogonal, then Equ. (5.3) would be 0. But physically, the spectra of the components overlap, e.g., HS and CNTs have a peak at about 285 eV. Apart from that, the required orthogonality of the eigenspectra in the PCA does not make use of the fact, that the physical quantities have to be positive.
Another point is that the reference intensity I_0 has to be determined before and depends on the location in the image area, although it is present in every pixel in the area. The number of components in the subset is chosen by hand and also the number of possible clusters. So, if this choice is wrong, or the eigenspectra are wrong, the CA is used with defective data.
The algorithm for CO uses algorithms based on *box constraints*, here $[\infty, 0]$, and is written in R, a programming language and software environment for statistical computing and graphics (R-Project). A good introduction about solving constrained optimization problems numerically is for instance found in Nocedal and Wright [133]. For physicists, the most common approach to constraint optimization is of course the Lagrange formalism.

5.3.2.1 Data Set

The data are acquired by reading in the recorded stack of images. Fig. 5.22a shows one of the images of the stack, together with the spectra of the two pixels with highest and lowest intensity in Fig. 5.22b. Then the negative logarithm of the intensities is taken as depicted in Fig. 5.23.
Before the CO can be started, the images have to be aligned. Although the X1-A1 possesses a drift control, a drift is still observed in the imaged areas, if the stack images are compared

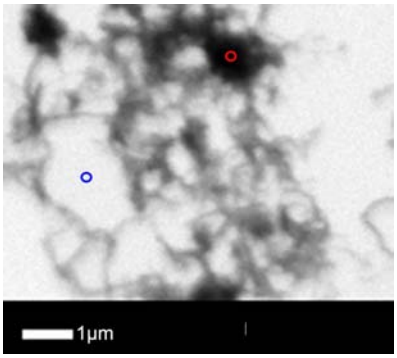

(a) *Sample image at 288.4 eV*

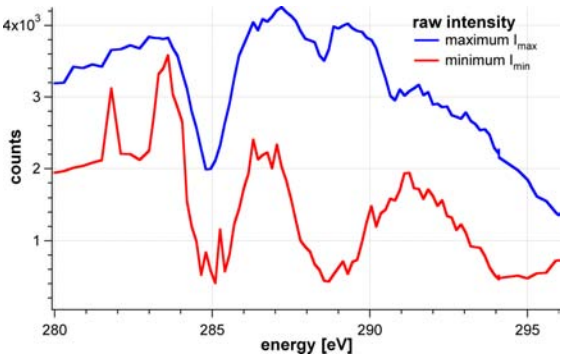

(b) *Spectrum of the raw data*

Figure 5.22: a) *Image of rCNTs at 288.5 eV;* **b)** *spectra of maximal and minimal intensity, corresponding pixels are marked in* **a)** *in blue ($I_{\max}$) and red ($I_{\min}$).*

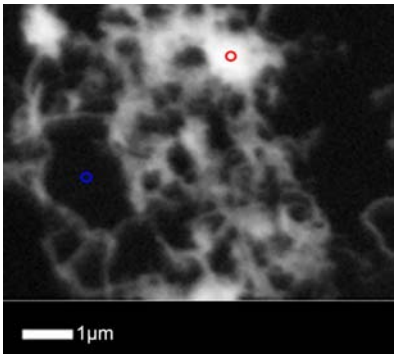

(a) *Sample image at 288.4 eV, displayed in negative logarithm of the intensities*

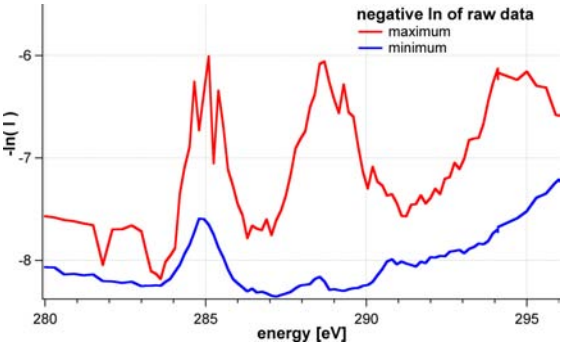

(b) *Spectrum of the raw data as negative logarithm*

Figure 5.23: a) *Image of rCNTs at 288.5 eV (intensities in negative logarithm);* **b)** *negative logarithm of the raw data shown in Fig. 5.22, the corresponding pixels are marked in* **a)** *in blue and red.*

pairwise. Therefore, if one pixel at position $(x, y,)$ is chosen and the intensity is read out for every image, the data will have a high noise level. To correct for this, the images of a stack need to be aligned properly.

In *stack_analyze* the image alignment is achieved either via correlation of all images of a stack with one reference image, which is also picked from the stack, or by correlating every image, apart from the first one, with its precursor. The first way results in a constant variance of $2\sigma^2$; in the second way, the variance increases proportional to he variance of a random walk.

Here, the data is aligned using an algorithm developed by Hotz et al. [81]. This approach is based on the analysis of the cross correlation of any two images. The variance is propor-

tional to $\frac{1}{\sqrt{\text{number of images}}}$. After the alignment, a smaller section of the stack area is chosen to avoid irregularities at the edges. The intensity spectrum from Fig. 5.23b is less noisy now, as can be seen in Fig. 5.24b.
It should be kept in mind that the spectra shown here always originate from only one pixel. Apart from that, only the negative logarithm has been taken, but no reference intensity I_0 has been determined for normalization (alternatively, it could be stated that $I_0 = 1$). This explains, why the spectra are not as smooth as in Fig. 5.8c and not quite resemble the spectrum, either.

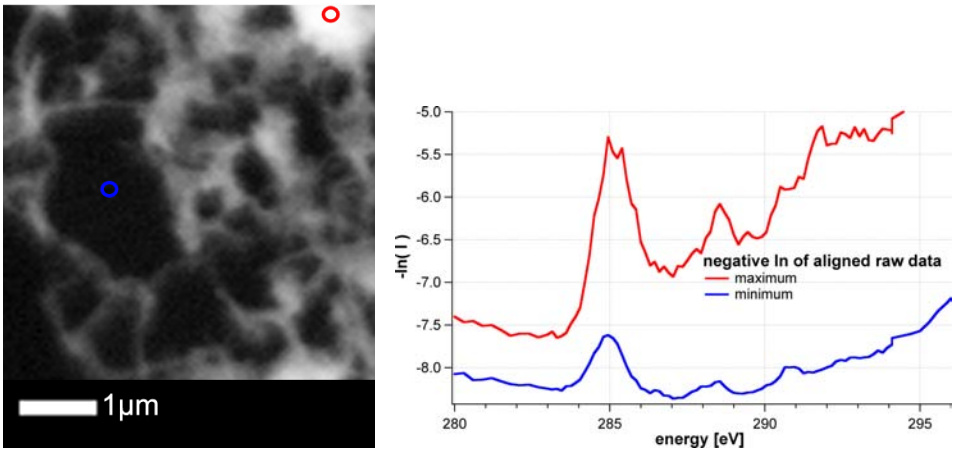

(a) *Sample image at 288.5 eV* **(b)** *Spectrum of the data after alignment*

Figure 5.24: a) *Image of rCNTs at 288.5 eV (intensities in negative logarithm) after alignment and cut to a smaller section;* **b)** *negative logarithm of the data of the aligned images, the corresponding pixels are marked in* **a)** *in blue and red.*

5.3.2.2 CO Approach

The algorithm starts with the well known Lambert-Beer law

$$\begin{aligned} I(x,E) &= I_0(E)\mathrm{e}^{-\mu(E)\,t(x)} \\ &= I_0(E)\mathrm{e}^{-\sum_{k=1}^{K}\mu_k(E)\,t_k(x)}, \end{aligned} \tag{5.8}$$

with $I(x,E)$ the transmitted intensity of a sample at position x in the image area, energy E and I_0 the initial beam intensity. The sample is assumed to be comprised of of $k = 1,\ldots,K$ components with absorption coefficients $\mu_k(E)$ with corresponding thicknesses $t_k(x)$. The data y are expressed as

$$\begin{aligned} y_{i,j} &\approx -\log(I(x_i,E_j)) \\ &= \sum_{k=1}^{K}\mu_k(E_j)\,t_k(x_i) - \log(I_0(E_j)). \end{aligned} \tag{5.9}$$

with the pixel position x_i (pixels numbered consecutively, $i = 1,\dots,n$) and the energy E_j ($j = 1,\dots,m$). The data are then collated in the data matrix $Y = (y_{i,j}) \in \mathbb{R}^{n,m}$. The still unknown terms in Equ. (5.9) are expressed as matrices, too: the absorption coefficients $F = (\mu_k(E_j)) \in \mathbb{R}^{n,K}$, the thicknesses $A = (t_k(x_i)) \in \mathbb{R}^{K,m}$ and the background B

$$B = (-\ln(I_0(E_j))\,\mathbb{1} = b_j\,\mathbb{1} \in \mathbb{R}^m\,, \tag{5.10}$$

hence

$$\Longrightarrow \quad Y \approx AF + b_j\,\mathbb{1}\,. \tag{5.11}$$

From this, a constrained optimization problem is formulated:

$$\begin{aligned} \text{minimize} \quad & \|Y - AF - b_j\,\mathbb{1}\|^2 \\ \text{subject to} \quad & A \geqslant 0 \\ & F \geqslant 0\,. \end{aligned} \tag{5.12}$$

More precisely,

$$\begin{aligned} \text{minimize} \quad & \|Y - AF - b_j\,\mathbb{1}\|^2 - \lambda_A\|A\|^2 - \lambda_F\|F\|^2 \\ \text{subject to} \quad & A \geqslant 0 \\ & F \geqslant 0\,. \end{aligned} \tag{5.13}$$

In first test runs, $K = 2$ components were searched, a logical starting point as only two components - rCNTs and sample free zones - are observed in the image stack. The coefficients λ_A and λ_F were set to $\lambda_{A,F} = 0.01$.
The background signal component b determined by Equ. (5.13) is the signal, which is found in every pixel (Fig. 5.27). The term AF is comprised of the thickness maps A and the absorption coefficients, i.e., the spectra F of the K components.
In Fig. 5.25, component 1 represents the sample-free component, i.e., the component of the background. Thus, it is almost constant. Component 2 shows the spectrum of the rCNTs, which resembles the spectrum observed in Fig. 5.8c.
Looking at the thickness maps of the components, Fig. 5.26, it seems that the background is a little overestimated. Therefore, component 1 acts as a balancing component. This is the reason, why component 1 is not completely constant, but exhibits some small features, e.g., at 285 eV, and why in the thickness map in Fig. 5.28, some structure is still visible.
Analysis of the experiments of the rCNTs in wet state, depicted in Fig. 5.9 lead to a similarly promising result, shown in Fig. 5.27 and Fig. 5.28. A background spectrum (Fig. 5.27a) was computed and two components could be determined; component 1 is again the sample-free image area, component 2 identifies the rCNTs. If Fig. 5.27b is compared to Fig. 5.9c, the similarities in the spectra are striking. However, the problem of overestimating the background arises again. This is observable in component 1, which acts as a compensating component and again is not constant.

5.3.2.3 Conclusion

The approach of analyzing image stacks using the CO could be validated by analyzing the measurements of the dry and wet state rCNTs recorded at the NSLS. The background

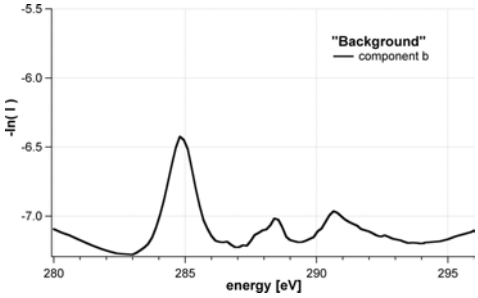

(a) *Background* **(b)** *Absorption spectra of 2 components*

Figure 5.25: *Result of the analysis of the dry rCNTs with the CO method.* **a)** *Plot of the background spectrum.* **b)** *Absorption spectra of component 1 (purple) and 2 (cyan).*

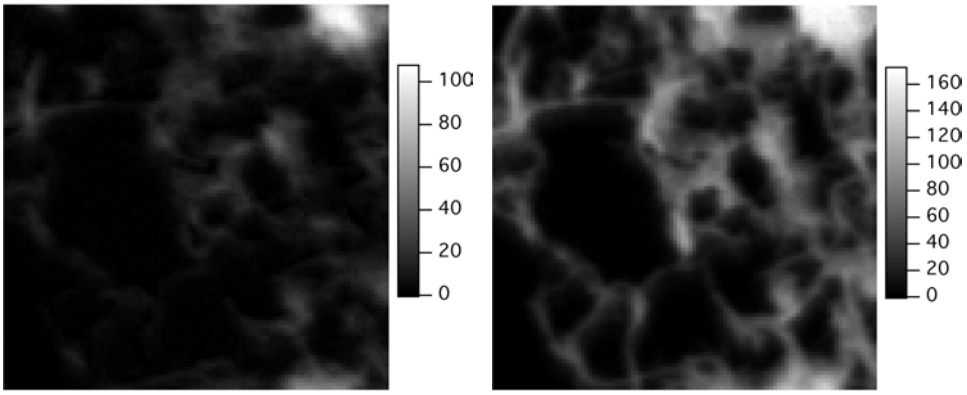

(a) *Thickness map of component 1* **(b)** *Thickness map of component 2*

Figure 5.26: *Thickness maps, representing the parameter A of* **a)** *component 1 and* **b)** *component 2.*

spectrum I_0 was determined for every pixel in the stack area and did no have to be chosen by hand. The obtained components are not abstract, as is the case when using PCA and CA. Instead, within the components the spectral information and their spatial distribution in the image area, i.e., the thickness maps, are combined. In contrast to the PCA/CA method, the data is not constrained to an orthogonal base, but the limitation is that the components cannot take on negative values (Equ. (5.12)), which corresponds to the physical meaning of the data: the absorption is always positive. The only necessary input is the number of components that should be computed. Attempts to evaluate stacks with three or more components are currently tested, but in the scope of this thesis, only the proof of principle is given.

Although the method still needs to be improved, the results are promising. One issue that needs to be regarded carefully is that the CO problem has to be *convex* in A and F separately

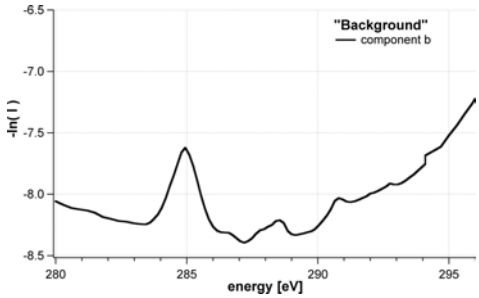

(a) *Background*

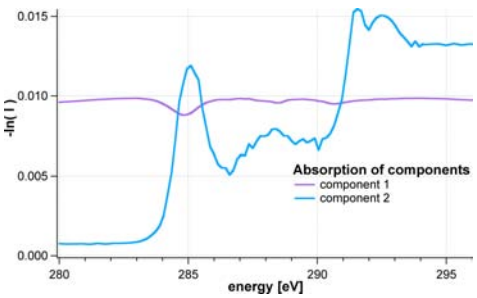

(b) *Absorption spectra of 2 components*

Figure 5.27: *Result of the analysis of the rCNTs in wet state with the CO method, showing absorption coefficients, representing the parameter F of* **a)** *component 1 (purple) and* **b)** *component 2 (blue).*

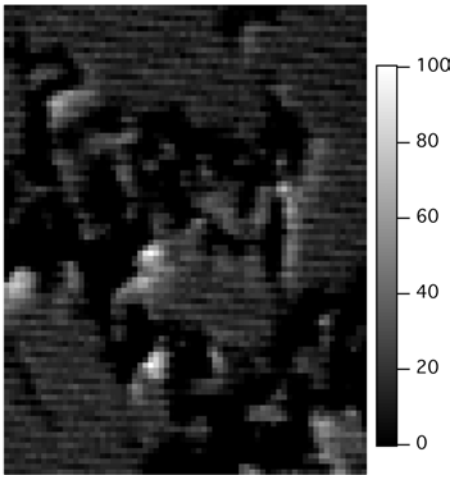

(a) *Thickness map of component 1*

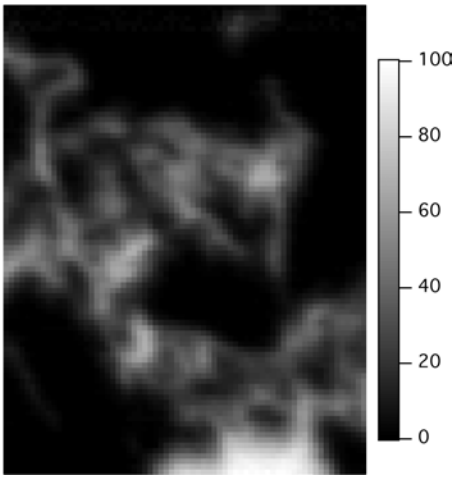

(b) *Thickness map of component 2*

Figure 5.28: *Result of the analysis of the rCNTs in wet state with the CO method. Thickness maps, representing the parameter A of* **c)** *component 1 and* **d)** *component 2.*

but not simultaneously. Hence, there may exist many local minimizers, and the algorithm might get stuck in a local minimum. While modelling A and F on a log-scale improved fitting, a mathematically sound treatment of the problem still needs to be developed.

6 Complex Structures in Biological Cells

Light microscopy reaches a resolution limit at about 200 nm as stated by Abbé ($d = \frac{\lambda}{2n\sin\alpha}$), which is often not sufficient for investigation of biological cells that have a typical size range of 1 µm - 50 µm. One way to achieve a higher resolution is the application of STED microscopy (stimulated emission depletion) [53, 214], STORM (stochastic optical reconstruction microscopy) [83, 84], or PALM (photoactivated localized microscopy) [25, 156]. The advantage of these methods is that the samples are still alive, but certain molecules have to be marked with photo-switchable fluorescent dyes. Detecting the fluorescence signal, resolution values down to 10 nm - 20 nm have been demonstrated in fixed cells. However, this is not the natural state of the cells and furthermore, only the stained parts of the cells can be seen, whereas the rest has to be imaged using other techniques, often involving lower resolution and more preparation of the cells.
Electron microscopy has developed to be one of the primary imaging techniques [154, 175, 186]. The low natural contrast and the small penetration depth of electrons require the samples to be fixed and cut into small sections of less than 0.5 µm. Before slicing, the samples have to be embedded; a process, which might have a significant impact on the structure [119].
As mentioned before, water absorbs much less than organic specimens in the water window [107], i.e., cells can be imaged in water layers of up to 10 µm thickness. This also enables tomographic studies of cells [113, 119, 140, 163]. Because of the high radiation dose, the samples for tomography need to be chemically or cryogenically fixed, too [17]. The radiation dose is however much lower than for electron microscopy.
In addition, it should be mentioned that in the hard x-ray regime, coherent diffraction imaging (CDI), which obtains the image from the diffractive pattern of a sample [65, 84, 171, 194], might soon provide an alternative approach in x-ray microscopy. One difficulty in imaging biomolecular structures is that spatial scales of most biomolecules are below the resolution limit of the x-ray microscopes.

6.1 Imaging Vascular Smooth Muscle Cells (VSMCs)

Microscopic investigations of cells are facing the challenge of how much the samples are altered during the preparation procedure to obtain an exact image of the cells in their natural state. Using X-ray microscopy, no staining of the samples is needed, since natural contrast results from the absorption coefficient, which depends directly on the elemental composition and thickness variations in a sample [121, 217]. Additionally, x-ray spectromi-

croscopic experiments on cells provide deeper understanding of the chemical processes in a cell. For instance, the calcification of bacterial cells [19] or their ability to process sulphur [134] has been assessed by this method. Also, other cell types have been studied using spectromicroscopy [19, 61, 119]. Such a chemical state analysis of low Z elements is hard to achieve with electron microprobes.
To prevent chemical changes and enable simple handling, fixing techniques are usually avoided for the preparation of environmental samples. Here, the effect of non-invasive sample preparation and chemical fixation on VSMCs is investigated [168].
VSMCs were selected because of their high amount of actin, a basic protein of the cytoskeleton. They form the major part of blood vessel walls, regulating the blood pressure by alternating contraction and relaxation. Vessel diseases like ateriosclerosis develop, if these cells proliferate (hypertrophy and/or hyperplasia). Often, these changes of the cells are already observable in the phenotype. Imaging of VSMCs is mainly performed by light microscopy and electron microscopy, for which the cells had been fixed and cut into thin slices [199].
The cells here were studied at the C K-edge and Ca $L_{II,III}$-edges, to find out, which parts of the cells are discernible, from their structure and to gain insights from additional spectroscopic information. A feasible sample thickness at the C and Ca edges is in the range of a few micrometers. Because the VSMCs are comparably thin, it is possible to work with energies at the Ca $L_{II,III}$-edges in absorption, without depending on much more elaborate fluorescence experiments at higher energies.
Starting with fixed, dry and fluorescence-marked cells, it was continued with fixed cells in aqueous environment. To prove that high resolution micrographs of cells are also feasible with compact x-ray sources for imaging-only studies, a compact TXM operated with a laser plasma source was used, too. Thereafter, dry but unfixed cells were investigated and the last step involved living cells kept in medium between two Si_3N_4-membranes. Both high resolution imaging and spectromicroscopic studies involved high radiation doses - this issue is discussed in section 6.3.3. The main experiments were carried out using the STXM at BESSY II, where the images are synchronized as *pgm* files. Therefore, no calibration bars are given, see section 5.1 and the appendix A.

6.2 Materials and Methods

6.2.1 Sample Preparation

The vascular smooth muscle cells (VSMCs), purchased from Coriell Institute of Medical Research (USA), were grown on Si_3N_4-membranes of 100 nm thickness, see appendix B, and treated further depending on the planned experiment.
For an improved adhesion of the cells, the Si_3N_4-membranes were coated with collagen (conc. $1\ \frac{\mathrm{mg}}{\mathrm{ml}}$) for 10 minutes and afterwards rinsed with ultrapure water (MilliQ). The cells, cultivated in a tissue culture dish, were dissociated with trypsin (Invitrogen GmbH, Karlsruhe, Germany), pipetted into a Falcon tube, and spinned down (800 rpm, 10 min.). After removing the supernatant, the pellet was resuspended in medium and the cells were spread over the Si_3N_4-membranes in a tissue culture dish, filled with medium (90 % low glucose DMEM, 9 % fetal calf serum, 1 % penicillin-streptomycin, all from Invitrogen). The

cells were incubated for one day (37 °C, 5 % CO_2). In Fig. 6.1 the preparation of the different cell samples is illustrated.

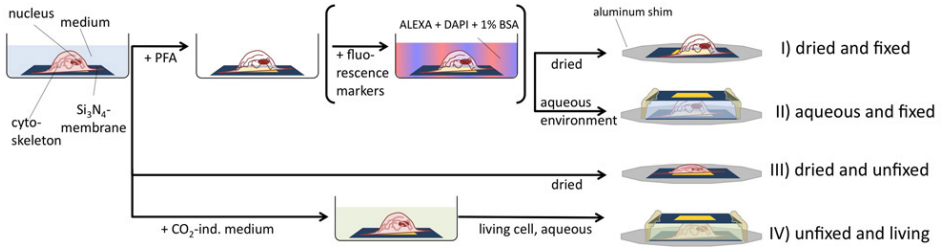

Figure 6.1: *Sketch of the preparation procedure. The drawings show a cell adhered to a Si_3N_4-membrane in a petri dish and the further preparation to I) dried and fixed, II) aqueous and fixed, III) dried and unfixed and IV) unfixed and living cell samples.*

Immobilization of the VSMCs The preparation of the dried and aqueous fixed samples is essentially the same apart from the drying, see step I) and II) in Fig. 6.1. For the fixation, the medium was removed from the Si_3N_4-membranes, and paraformaldehyde (4 % PFA, 0.06 % 1M NaOH in 1× PBS, see appendix B) was filled into the culture dishes, which were then cooled for ca. 15 min on ice. After removing the PFA-solution, the VSMCs on the membranes were rinsed with ultrapure water a few times and put into Eppendorf vessels, containing ultrapure water, for transport. For the x-ray experiments the Si_3N_4-membranes were taken out of the vessel and either left on air to dry or covered with a second Si_3N_4-membrane and sealed with glue forming a wet chamber.
For staining, the membranes with the fixed cells were washed and put into a solution of 0.5 % Triton-100 (in PBS) at room temperature for 10 - 20 minutes. The labels rhodamin-phalloidine (for the actin filaments, 2.5 %) and DAPI (for the nucleus, ~ 0.25%) were dissolved in 1 %-BSA solution and the cells were left in the solution for one hour at room temperature. Then the Si_3N_4-membranes were washed and later stored in ultrapure water. The fluorescent images were recorded with an Olympus BX51 microscope, using a 40×-objective. The subsequent preparation at the x-ray microscope was the same as for the fixed cells without dyes.

VSMCs transported alive For the experiments with unfixed cells, the culture medium was replaced by CO_2-independent medium (Invitrogen). That way, the cells were cultivated for use outside the bio-laboratory at the beamline of the storage ring. Under the microscope, there was no difference in appearance observable, whether the cells were only transported in the new medium or if they had already grown in it.
For the experiments with dry unfixed cells, the Si_3N_4-membranes were taken out of the medium, rinsed with ultrapure water and let dry, before they were glued to an aluminum shim and then mounted into the x-ray microscope (Fig. 6.1, step III).
Samples of living cells were prepared by taking out a Si_3N_4-membrane of the CO_2-independent medium, carefully drying it on the bottom side and gluing it to an aluminum

shim. A second Si_3N_4-membrane was placed on top and sealed with glue forming a wet-chamber (Fig. 6.1, step IV), as described in the preparation of the aqueous fixed cells.

6.2.2 Instrumentation

First images of dry and fluorescence marked cells were recorded using the cTXM, described in section 3.1.3. The exposure times were in the range of several minutes.
The main part of the experiments was carried out using the STXM at BESSY II, see section 3.2.2. To obtain spectroscopic data of the bound C and Ca in the samples, stacks of images were recorded, tuning the energy around the C K-edge (280 eV - 300 eV) and the Ca $L_{III,II}$-edges (342 eV - 357 eV), with a stepsize of 0.2 eV. Being a chromatic optical element, the zone plate was repositioned for every energy step. The dwell times per pixel for the images were between of 2 ms - 6 ms.

6.2.3 Analysis

The evaluation of the x-ray data consisted of three complementary parts: For the visual information of the high resolution images, which also allowed for comparison of the samples before and after taking stacks, ImageJ was used. The image stacks were also processed with *stack_analyze* [94, 118]. The obtained spectra were also used to estimate the radiation dose [17]. A linear pre-edge background was subtracted from each spectrum, defining the zero line, and the spectra were smoothed using a sliding box algorithm with a width of two points. The spectra of the C K-edge were normalized by setting the highest data point to 1. The spectra from the stacks were evaluated using published NEXAFS data from polymer and cell science [19, 24, 114, 131].

6.3 Results and Discussion

6.3.1 Imaging

Due to the lack of comparable x-ray spectromicroscopy studies on VSMCs, electromicroscopic images and images from other cells, e.g., fibroblasts, were used for comparison and to discern cell organelles and ultrastructure [69, 121, 163, 199, 217].

6.3.1.1 Fixed Cells

The first experiments were carried out, using dry and fixed cells, some of the samples were marked with fluorescent dyes. One of these samples is depicted in Fig. 6.2, giving an impression of the average growing pattern of the VSMCs on the Si_3N_4-membranes.
First experiments with dried and fixed cells were carried out using the compact TXM at Stockholm and the STXM at BESSY II, testing whether stress fibers, recognizable from fluorescence images, can also be observed in x-ray micrographs (Fig. 6.3). The fluorescence image in the inset of Fig. 6.3a has been magnified, turned into a half-tone and used as the grid of the collage. The stress fibers and the nucleus with one nucleolus are clearly visible. In particular, in the round x-ray micrograph in the lower right the finer actin fibers of the cytoskeleton are discernible. It is, however, hard to distinguish other objects, apart from

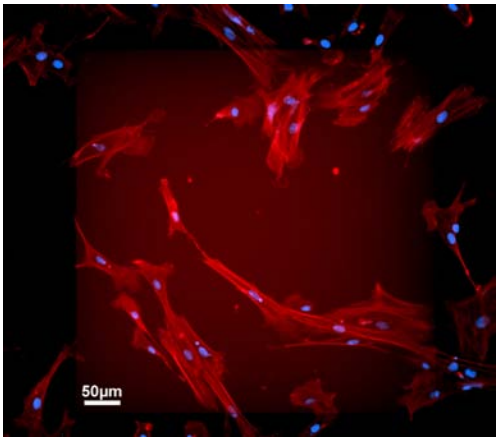

Figure 6.2: *Fluorescence image of the cell sample imaged with the cTXM at KTH Stockholm. The Si_3N_4-membranes used there had a different geometry, but the same thickness, frame: 10× 10 mm^2, window: 0.5× 0.5 mm^2, thickness 100 nm.*

what might be a mitochondrion (arrow).
In Fig. 6.3b and 6.3c, a composition of STXM-images taken an BESSY II is shown, again with an inset of the fluorescence image. Comparing fluorescence and x-ray image, the thicker actin bundles are identified. In the x-ray images, smaller features and more parts of the cytoskeleton are discernible, too. Since they are not visible in the fluorescence image, they are not part of the actin network. The black granules, about 300 nm in size might be lysosomes or endosomes [217]. Mitochondria, having a slightly more absorbing membrane are indicated by white arrows. In the nucleus, several nucleoli can be identified by their stronger absorption. Close to the nucleus, a holey structure is observed, which could be the remainder of a Golgi apparatus, often found close to nuclei.
In the dry and fixed cell in Fig. 6.3d, the lamellipodium was imaged with higher resolution than the rest. Nucleus, nucleoli and black granules are visible in the central cell part. The holey, less absorbing structure around the nucleus is more prominent here. The image demonstrates that possible differences between marked and unmarked cells, stemming from the fluorescence marking procedure, are not visible in the structure of the x-ray images of the cells.
To find out how the contrast of the fixed cell changes in water and to restore eventual collapsed structures and wrinkles originating from the drying process, the experiments were repeated with fixed cells in aqueous environment, see Fig. 6.4. A collage of images covering of a whole fixed cell in aqueous environment is depicted in Fig. 6.4a. A 5×-zoom of the section marked with the red frame is shown in Fig. 6.4b. The sample thickness was estimated to about 4 µm.
Although the absorption of the water is only 10% of the absorption of the organic sample material, the contrast is less sharp than in the dry cell samples, which complicates the recognition of inner cell organelles like mitochondria. Also the lamellipodium stretching out into the upper half of Fig. 6.4c is barely visible (black arrow). Small but dense clusters inside the cells are visible, assumingly lysosomes. Apart from that, nucleoli are hardly observable, maybe due to the lack of an own membrane. From comparison with the fluorescence marked cell, the structures observable in the nucleus area seem to be outside

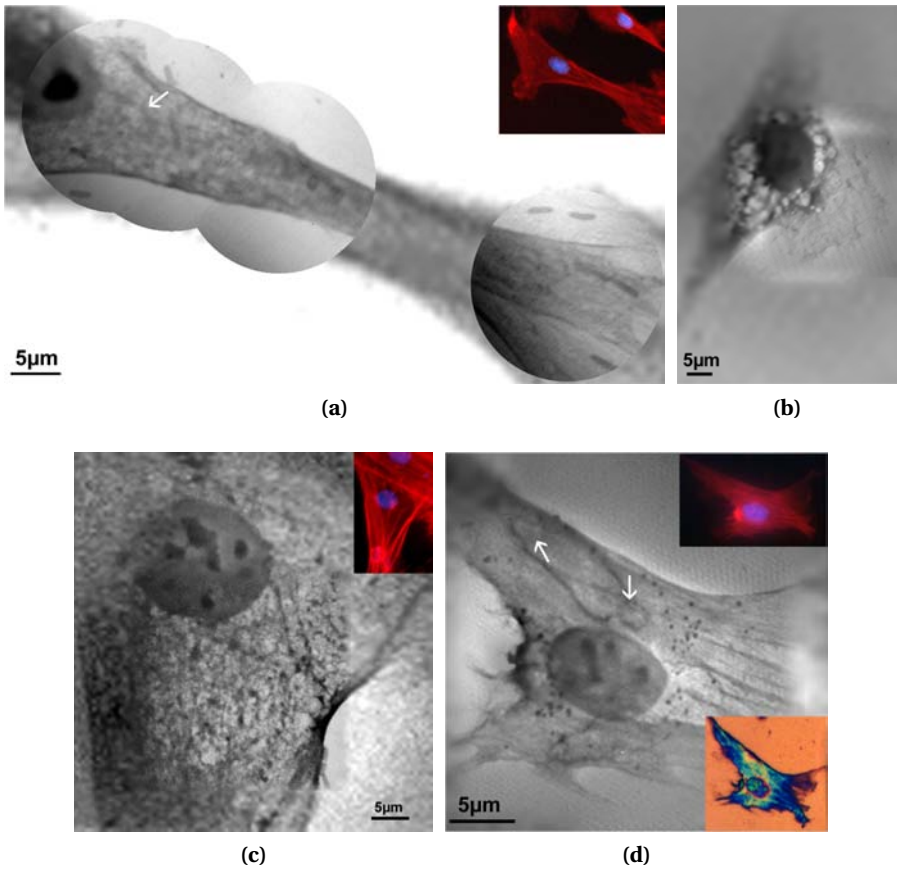

Figure 6.3: *Collages of images of fixed and dried cells, the insets show the fluorescence images.* **a)** *The x-ray image recorded with the cTXM (pixel size 30 nm at 368 eV, 10 min).* **b)** - **d)** *The other three images were taken with a STXM at 300 eV with dwell times between 2 and 6 ms and smallest pixel size of* **c)** *50 nm and* **b)**, **d)** *100 nm.* **d)** *The lower inset shows an image of the cell taken with the light microscope.*

and on top or below the nucleus and part of the actin network and the cytoskeleton. The area around the nucleus has a structure, different from the parts of the cell that are closer to the border. Close to the nucleus, the cell exhibits a holey structure, as also observed in Fig. 6.3a and 6.3b, where less photons are absorbed. In this structure part of the cell, the endoplasmic reticulum and Golgi apparatus could be located, which are found close to or around the nucleous in eukaryotic cells. The outer parts of the cells exhibit a smooth structure, with thick stress fibres and also very dense and actin rich parts, as can be proved from the inset in Fig. 6.4a. In both cells, a horizontal direction of the stress fibers is discernible. Especially in the parts of the collages with the highest resolution (pixel size 50 nm), thicker and thinner parts are very distinct.

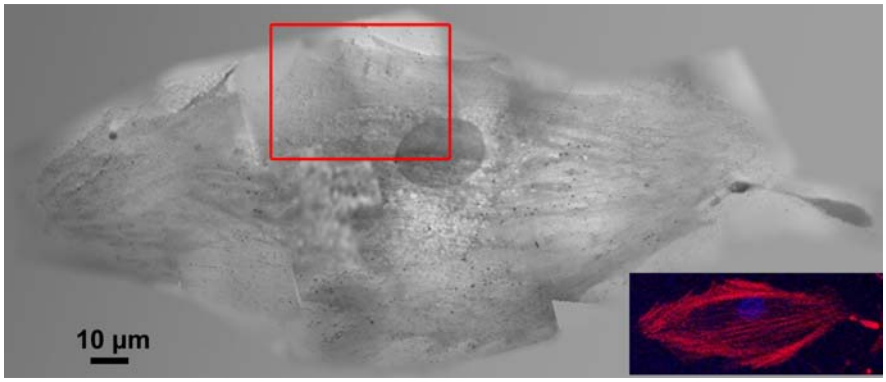

(a) *Fluorescence marked VSMC*

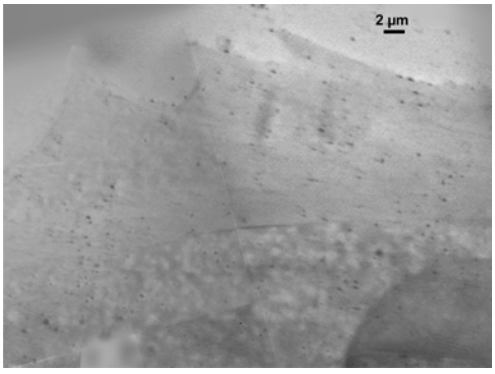

(b) *2.5× zoom of a)*

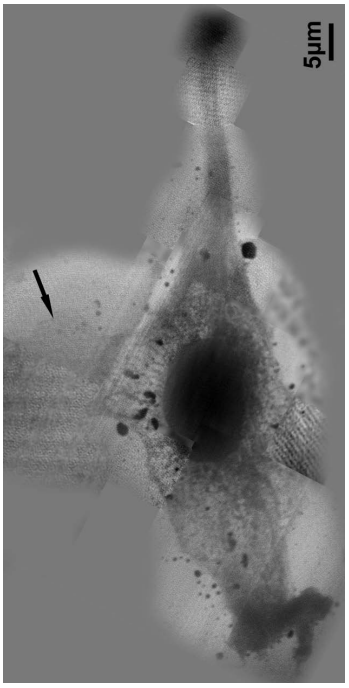

(c) *Unmarked VSMC*

Figure 6.4: *Collages of images from a fixed cell in water, with pixel sizes ranging from 50 nm to 250 nm, recorded at 300 eV.* **a)** *Images of a fixed and fluorescence marked cell are depicted, with the fluorescence image in the inset;* **b)** *Smaller area of the cell, but with an additional 2.5×-zoom.* **c)** *This cell was not marked with the fluorescent dyes. The arrow indicates the lamellipodium.*

6.3.1.2 Cells without Fixation

Unfixed but dried cells were imaged to compare them with the originally living cells. Cellular network and organelles certainly look different, after the cell has dried, but in contrast to the fixed cells, nothing of the cell material was removed. Although the cell has partly disintegrated during the drying process, the nucleus is still visible in Fig. 6.4. Bearing in mind that nucleoli are not membrane-bound structures but are distinguished by their function, it is not surprising that they are not as easily recognized as in the experiments

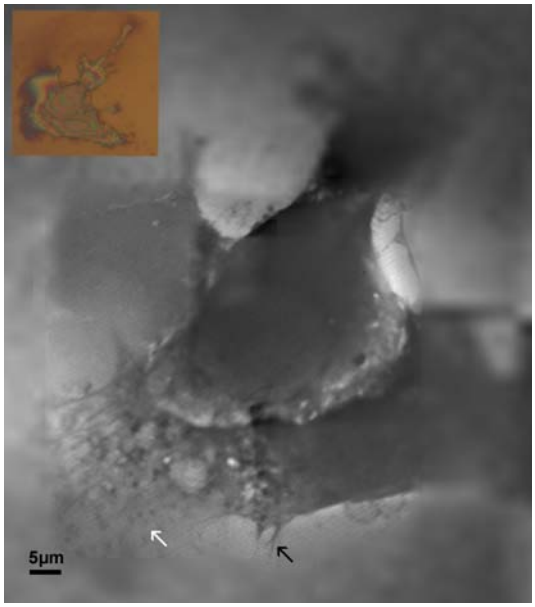

Figure 6.4: *Collage of images of a non-fixed dried cell, recorded with the STXM at 300 eV, with smallest pixel size of 120 nm; the inset shows the light microscope image.*

with the fixed and dried VSMCs. However, some x-ray dense spots are located in the nucleus, which could be nucleoli. Besides, a region with holes can be seen around the nucleus as well as the lamellipodium (white arrow) and even some small tethers (black arrow). Since it was not expected to resolve any fine structures in the dried VSMCs, the smallest pixel size in Fig. 6.4 has been set to only 120 nm.
For the experiments with the living VSMCs shown in Fig. 6.5, extreme care was taken that the cells did not dry out. That means, a cell was alive in the CO_2-independent medium until the first x-ray image was recorded.
The first cell (Fig. 6.5a - 6.5c) grew completely in the medium, while the two cells just after cell division (Fig. 6.5d and 6.5e) were grown in normal medium and then transferred to CO_2-independent medium.
In Fig. 6.5a, structures in the nucleus absorbing slightly more than the rest of it are noticeable, which could be nucleoli (small arrows). In the region marked with the upper red box in Fig. 6.5a and magnified in Fig. 6.5b, presumably a mitochondrion (arrow) and some endosomes (dark spots) are visible. In this cell, the region around the nucleus also exhibits the less absorbing and holey structure as seen in Fig. 6.4, indicating for the endoplasmic reticulum or a Golgi apparatus; this can be seen in more detail in Fig. 6.5c, the magnified image of the lower red box in Fig. 6.5a. The outstretched parts of the cell again display smoother tissue indicating actin fibers, as seen in Fig. 6.4.
The two separating cells in Fig. 6.5d and 6.5e seem to be thicker, making internal structures harder to identify due to the much stronger absorption. The left cell was imaged with higher resolution and is also depicted enlarged in Fig. 6.5e. The cells are not completely separated yet, and some of the tissue, which connects both cells, is noticeable between them and in the membrane of the left cell (arrow in Fig. 6.5d).

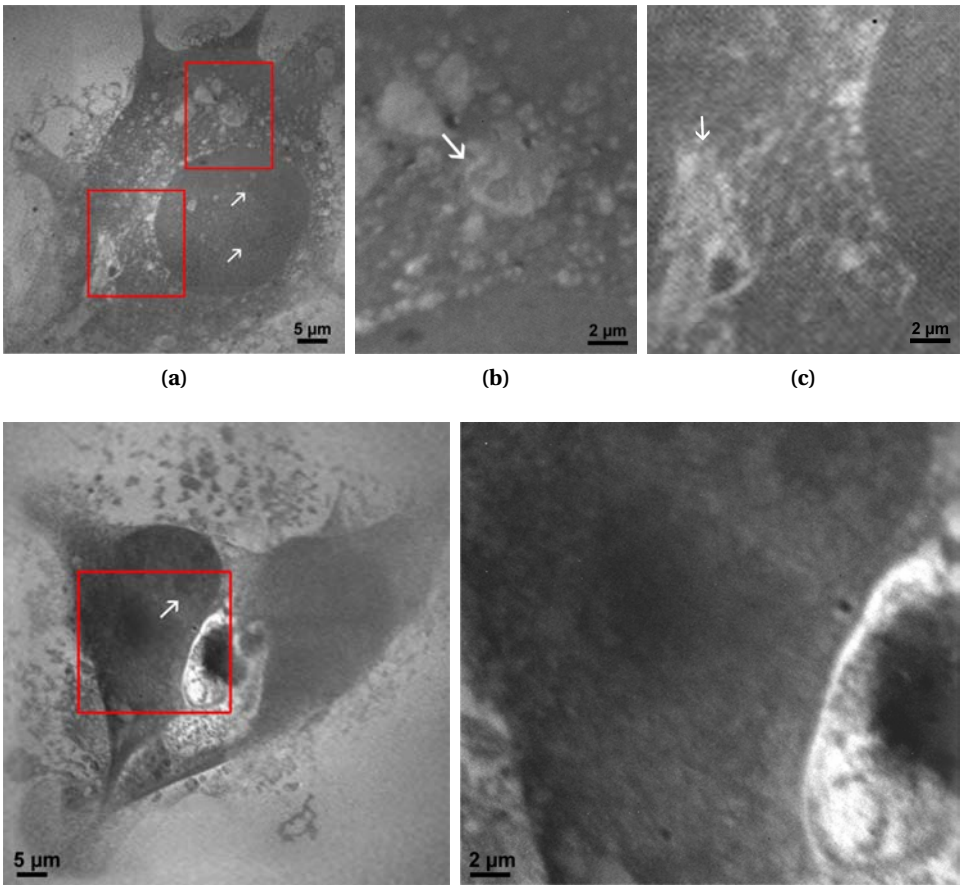

Figure 6.5: *Collages of x-ray micrographs of initially living VSMCs in CO_2-independent medium, with smallest pixel size of 50 nm, recorded at 300 eV.* **a)** *A cell grown in this medium; magnification of cell parts showing, what is supposedly* **b)** *a mitochondrion and* **c)** *part of the endoplasmic reticulum.* **d)** *Two separating VSMCs, originally grown in regular medium, the left cell has been imaged with higher resolution;* **e)** *a magnification of the region around the nucleus.*

In all cell images, natural contrast makes it possible to distinguish larger cell organelles, the nucleus and areas rich in (actin) fibres, if present. For aqueous samples, imaging is more difficult because of the additional absorption of the water, and a longer dwell time is necessary. It is not surprising, that the contrast in the unfixed cells (Fig. 6.4 and 6.5) is not as sharp and the cytoskeleton is not as clearly visible as in case of the fixed cells (Fig. 6.3 and 6.4), because the immobilization procedure mainly preserves the cytoskeleton and most of the other cell material and the cytoplasm is removed. This also applies to the area surrounding the cells. Whereas in case of the fixed specimens the borders of the cells are

well defined, the originally living cells exhibit a lot more tissue around them. Therefore, the experiments of the dry and fixed and the living cells have yielded the most instructive images.
In addition, the precision of Fig. 6.3a demonstrates the ability of imaging delicate objects like cells and tissue with a compact source. If only the microscopic information is of interest using illumination by a laboratory x-ray source is sufficient.

6.3.2 Spectromicroscopy

The results of the spectromicroscopic studies are shown in Fig. 6.6. Areas with supposedly high actin content were selected as ROIs, the nucleus, and, if present, special or noticeable parts like the black granules or localized spots of high Ca absorption, Ca hotspots, which were identified from the Ca-spectra of the samples. These hotspots are no artifact of the preparation procedure, since they were found in almost all cells. Their occurrence is limited to the cytoskeleton part of the cells, close to the nuclei, no hotspots were found. If possible, the same regions of the samples were used for spectromicroscopy at the C K-edge and Ca $L_{II,III}$-edges. At first, the spectra at the C K-edge are discussed, because the effect of the choice of the ROIs and the preparation method are better visible here. Spectra of polysaccharides, lipids, DNA, proteins (albumin and fibrinogen as model) and $CaCO_3$ from the literature were used as reference spectra [19, 76, 114, 208]. Data from other published NEXAFS experiments also supported the peak assignment [10, 108]. The peak positions of the reference data are listed in Table 6.1.

Table 6.1: *Energy positions and assignments of features of the absorption spectra of the C K-edge and the Ca $L_{II,III}$-edges, gained from the areas in the cells as depicted in Fig. 6.6.*

position (eV)	transition	comment
285.1	$\pi^*_{C=C}$	aromatic
286.0	$\pi^*_{C=C}$	phenolic and/or ketonic
287.1	σ^*_{C-H}, 3s, $\pi^*_{C=C}$	C(ring) heterobound, OH-groups
288.2	$\pi^*_{C=O}$	amide carbonyl groups (peptide bond in proteins), ketonic
288.9	$\pi^*_{C=O}$	carboxylic groups in polysaccharides, $CaCO_3$
290.0	σ^*_{C-X}	X: N, P, F,...
> 291	σ^*_{C-C}, σ^*_{C-O}	broad peaks
~ 349	Ca L_{III}-edge	
~ 352	Ca L_{II}-edge	

6.3.2.1 C K-Shell Absorption Edge

The main features visible at the C K-edge are the peaks resulting from transitions to the following orbitals – $\pi^*_{C=C}$ at 285 eV (aromatic rings), $\pi^*_{C=C}$ at 286 eV (phenolic), $\pi^*_{C=O}$ at

288.2 eV (carbonyl) and $\pi^*_{C=O}$ at 289 eV (carboxyl, $CaCO_3$). For the Ca $L_{II,III}$-edges only the two peaks of the edges are of interest, because the resulting spectra are too noisy to analyze any further features.
For the dry and fixed cells, the spectra of the nucleus, the actin rich part and the black granules differ strongly at energies below 291 eV. The black spots exhibit the smallest peak at 285 eV, but have two noticeable peaks at 287.5 eV and 288.5 eV. The spectrum shows features alike to reference spectra of lipids and proteins.
The spectrum of the area in the nucleus has a prominent peak at 288.2 eV and, at least partly, combines characteristics of spectra of nucleic acid and polysaccharide. The spectrum of the actin rich area has the highest $\pi^*_{C=C}$ peak, but no strong resonance around 289 eV, which makes it harder to compare it to the reference spectra, but a combination of the two spectra of the model proteins albumin and fibrinogen seems to be the best guess.
The spectra of the fixed cell in aqueous environment do not show remarkable differences apart from the $\pi^*_{C=C}$ peak at 285 eV being slightly higher for actin than for the nucleus region.
For the unfixed, dried cell, the spectrum of the nucleus area looks similar to the one of the fixed dry cell, but the part between 285 eV and 288.5 eV is different and appears more like the reference nucleic acid in Lawrence et al. [114]. The identified Ca hotspots interestingly have a C NEXAFS spectrum, that is almost exactly like the spectrum of the nucleus region. In the spectrum of the black spot several smaller peaks are found between 286 eV and 290 eV.
A superposition of the reference spectra of lipid, saccharide and protein would lead to a similar structure. The actin rich part has a signature similar to the spectra of the two model proteins. The tethers show a NEXAFS signature, which differs from the other spectra. There is no peak at 285 eV, but rather at 284 eV. This shift could be an artifact, owing to the selection of I_0, or could result from transitions in unsaturated carbohydrate chains [208]. The rest of the spectrum resembles the reference spectrum of fibrinogen.
Regarding the (initially) living cell, the spectrum of the nucleus area again has the smallest $\pi^*_{C=C}$ peak. Compared to the dried unfixed cell, the shoulder around 287 eV is steeper, and there is no new rise at energies above 290 eV. The aromatic and the carbonyl (288.2 eV) peaks from a originally living cell are higher than in the spectra of the unfixed but dried cell. Furthermore, the ratio $\pi^*_{C=C}/\pi^*_{C=O}$ of the area of high actin amount is higher in case of the living cell. In the spectral region of 290 eV, where the transitions $1s \rightarrow \sigma^*_{C\text{-}C}$, $\sigma^*_{C\text{-}O}$ are located, the dried cell shows more absorption than the living cell, again in comparison with the carbonyl peak. This means, that less aromatic rings and less C=O-double bonds are present in the unfixed and dried cell.
A comparison of the C K-edge NEXAFS spectra demonstrates the influence of the preparation. For instance, in dry state, different parts of the fixed cell exhibit different spectra, but in wet state the sample has almost the same C K-edge signature for regions in the nucleus and regions rich in actin. In the water, different ROIs do not yield to different spectra. This might be caused by small parts of cell tissue being detached by radiation, then diffusing in the surrounding water, such that the spectra show an average of the whole cell material.
The most striking difference between the fixed and the unfixed VSMC samples is the comparably higher peak at 288.2 eV, where the resonances of the C=O carbonyl bonds in

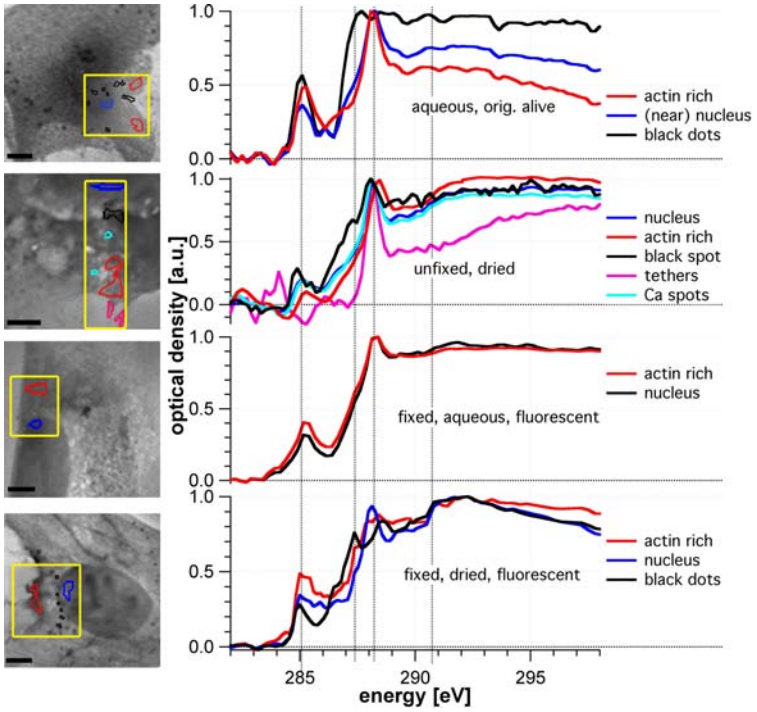

(a) *C K-edge*

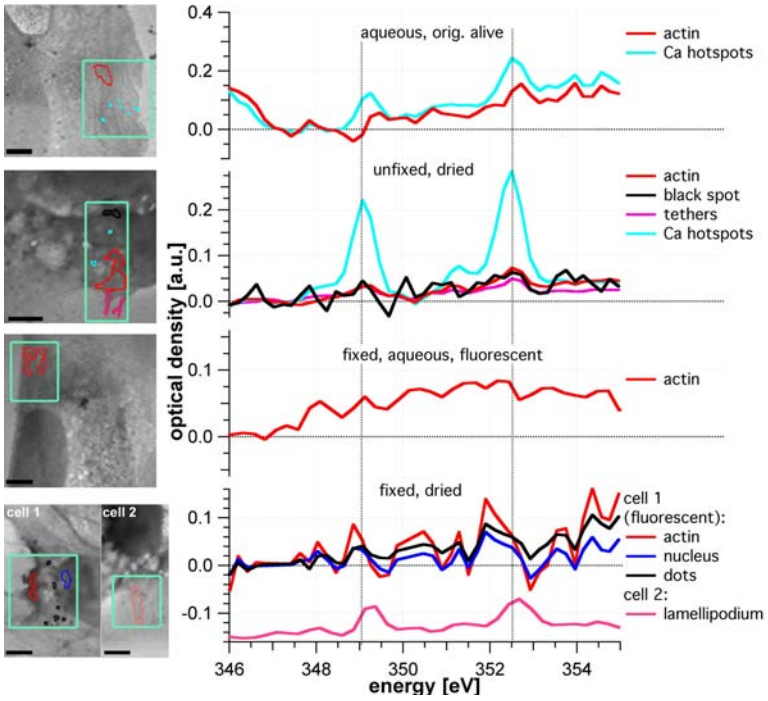

(b) *Ca $L_{II,III}$-edges*

Figure 6.6: *NEXAFS spectra of distinct areas of the cells, prepared in the four described different ways,* **a)** *at the C K-edge (280 eV - 300 eV, stepsize 0.2 eV) and* **b)** *at the Ca $L_{III,II}$-edges (346 eV - 355 eV, stepsize 0.2 eV). The unfixed and dried resp. fixed, dried and fluorescence marked cells, of which the spectra were recorded, are also depicted in Fig. 6.3c resp. 6.4. The size of the scale bar indicates* $5\,\mu m$.

peptides are located, demonstrating that the fixing process preserves only the network structures, but not the chemical composition. In spite of differences between the reference and the recorded spectra, most probably stemming from the reference samples being measured in pristine form and not in the cellular environment, it was possible to identify similar peaks and to draw conclusions about the molecular composition of the ROIs in the cell.

6.3.2.2 Ca $L_{II,III}$-Shell Absorption Edges

It is well known from literature, that Ca is bound within the actin filaments of the cytoskeleton (*F-actin*); some authors state that F-actin in cells is partly used to store Ca^{2+} [112]. Therefore, the intention was to identify actin bundles or actin rich areas due to the Ca signature – but the Ca signal was too uniform over the cell area. However, in the unfixed cells localized spots of very high Ca amount, here called Ca hotspots, were detected. These Ca hotspots could be Ca sparks or buffs [41, 97, 120, 139, 221] that have also been detected in cells before, but since the time dependence was not monitored, this is not specified in further details.
The height of the peaks is proportional to the Ca concentration within the ROIs. For the fixed and dry cells this means that in the lamellipodium of cell 2 Ca is traceable, but the spectra of cell 1 are very noisy, and the Ca peaks are hardly visible if present, see last panel in Fig. 6.6b. Apart from the difference in chosen ROIs, this could also be due to the fact that cell 1 is fluorescence marked, whereas cell 2 is not, leaving out several steps of preparation. In the fixed cell in aqueous medium, no Ca was detected, which could stem from the dissolution of the remaining Ca^{2+} in the surrounding water. In the unfixed dried cell the Ca-peaks are well discernible especially in the tethers, proving that the detected Ca in the dried unfixed cell is not a remainder of the dried buffer. In the living cell the Ca signal is still perceivable, however, much weaker than in case of the dried cell, but again, Ca^{2+} is presumably dissolved in the medium. In both unfixed cells, small spots of high Ca concentrations were detected. The verification of Ca in the living cell, too, proves that the Ca and the hotspots in the dried cell are not resulting from the dried medium.
From the spectra it is also possible to give a semi-quantitative estimation of the C and Ca concentrations in the cells [33]. The density of carbon in the cells can be estimated using

$$\rho_{cell}\, t_{cell} \approx \frac{oD_{300\,eV} - oD_{280\,eV}}{\mu_{cell,300\,eV} - \mu_{cell,280\,eV}}\,, \tag{6.1}$$

with ρ the mass density and t the thickness of the sample. The optical density oD is determined by the Lambert-Beer law, Equ. (2.1). Standard values were used from CXRO [47] to approximate μ_{cell} for a cell of the composition 60 % H, 24 % O, 10 % C and 2 % N, using $\rho_{cell} = 1.06\,\frac{\mathrm{g}}{\mathrm{cm}^3}$. For the cells, the values of the spectra of the whole cell area (shown in Fig. 6.7d) were used, yielding values of $\rho_C t_C$ in the range of $2-3\,\frac{\mu\mathrm{g}}{\mu\mathrm{m}^3}\cdot\mu\mathrm{m}$. In turn, the Ca concentration was estimated via

$$\rho_{Ca}\, t_{Ca} \approx \frac{(oD_{352\,eV} - oD_{345\,eV}) - (\mu_{cell,352\,eV} - \mu_{cell,345\,eV})\rho_{cell}\, t_{cell}}{\mu_{Ca,352\,eV} - \mu_{Ca,345\,eV}}\,. \tag{6.2}$$

For the dry and fixed VSMC sample (cell 2) this yielded a Ca concentration of approximately $3\times10^{-2}\,\frac{\mu g}{\mu m^3}\cdot\mu m$ for the lamellipodium. The Ca concentration of the unfixed cells is roughly two times higher - unfixed, dry: $\sim 4\times10^{-2}\,\frac{\mu g}{\mu m^3}\cdot\mu m$, living $\sim 5\times10^{-2}\,\frac{\mu g}{\mu m^3}\cdot\mu m$. Furthermore, the calculations for the unfixed cells also revealed about two times higher concentrations for the Ca hotspots (unfixed, dry: $\sim 9\times10^{-2}\,\frac{\mu g}{\mu m^3}\cdot\mu m$, living $\sim 8\times10^{-2}\,\frac{\mu g}{\mu m^3}\cdot\mu m$), than for the actin rich areas.
Unlike for the spectra of the C K-edge, conclusions about the molecular composition cannot be drawn from the Ca $L_{II,III}$ spectra. However, the findings again demonstrate how invasive the preparation can be. Due to the fixation process almost half of the Ca and the Ca hotspots of a cell is lost.

6.3.3 Radiation damage

Radiation damage was observed in all cells. Some examples are shown in Fig. 6.7a - 6.7c. The dry and fixed samples were the least affected (Fig. 6.7a, followed by the unfixed, dried cell. In these two cases, only little thinning, or mass loss, of the irradiated part was visible. In addition, this was only observed after recording multiple images of one area with high resolution. Even then, the cellular structures were still visible, but the absorption had decreased.
Thinning was more severe for the aqueous samples, due to the fact that small parts of matter rapidly diffused when they are detached from the cells by x-radiation. Apart from that, the cell borders of the living samples blur, thin parts become broader and x-ray opaque clusters form, as can be seen in Fig. 6.7b and 6.7c. Fig. 6.7b depicts the spectra of the cell parts shown in Fig. 6.6. It proves that the thinning of the cells is most severe for the fixed and aqueous cells, since the transmission for this specimen is highest. Not only thinning, but also carbon clustering effects are noticeable, e.g., the spectrum of the originally alive cell shows a higher absorption between 292 eV and 300 eV than the unfixed and dry cell, although the mass loss was higher due to diffusion. Because of the radiation damage, statements about the features of the spectra at energies higher than 293 eV or 294 eV are not discussed in section 6.3.2. At this point, the stack area had already been imaged about 50 times, and one can assume that the absorption spectra are affected by thinning and clustering effects. However, spectroscopic investigations on living cells without cryo-fixation are feasible, because the loss in chemical bonds is almost equal for cryo and room temperature experiments, about 2% per MGy of the C=O bonds are destroyed [16, 17, 208].
The spectra in Fig. 6.7c were also used to calculate the dose D applied to the sample during the experiments, using

$$D = 2N_A r_e hc\frac{\phi\tau f_2}{\eta\Delta^2 A}, \tag{6.3}$$

with N_A Avogadro's constant, r_e the classical electron radius, h Planck's constant, and c the speed of light, A the atomic weight of the substance ($A_C = 12$), η the detector efficiency, ϕ the flux traversing the sample (in $10^3\,\frac{\text{photons}}{\text{s}}$), τ the dwell time in ms, the pixel size Δ^2

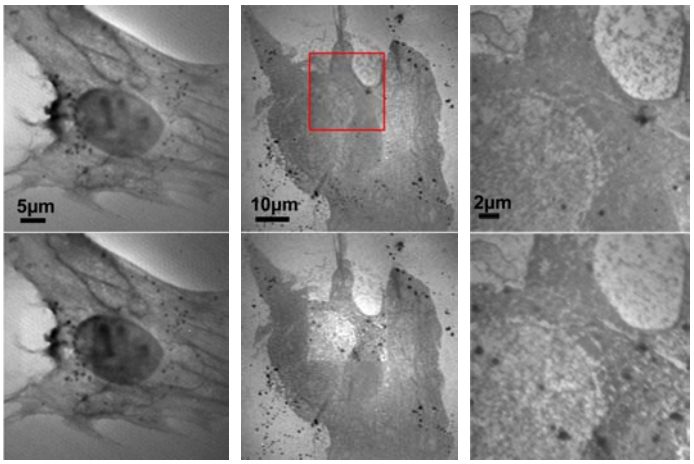

(a) *Fixed, dry* **(b)** *Originally living* **(c)** *Zoom of b)*

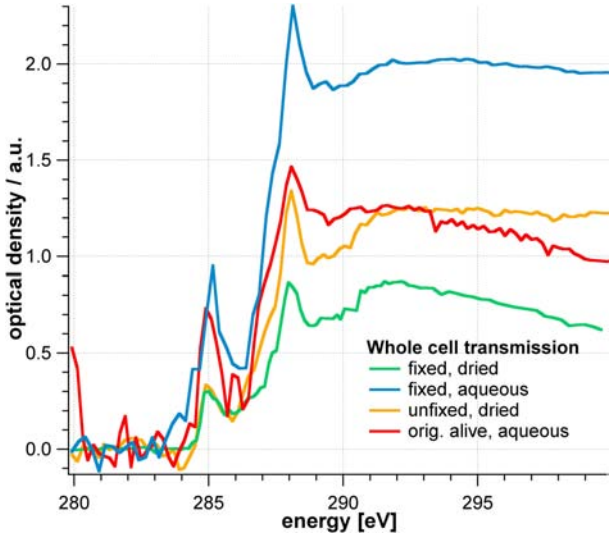

(d) *Spectra of whole cell area in stacks*

Figure 6.7: *Examples for the observed radiation damage.* **a)** *The fixed and dried cell from Fig. 6.3c is shown before (top) and after (bottom) recording two stacks of in total 143 images.* **b)** *Image of an originally alive cell before and after taking a series of 17 images with sub-100 nm resolution of a smaller area of the cell;* **c)** *the first and the last image of the series.* **d)** *Spectra of the whole parts of the cells seen in Fig. 6.6, details are given in the text.*

in nm^2, and f_2 the oscillator strength, which depends on the energy [198]. With

$$f_{2,E} = f_{2,300\,\mathrm{eV}} \frac{E}{300\,\mathrm{eV}} \frac{oD_E}{oD_{300\,\mathrm{eV}}}, \tag{6.4}$$

the radiation dose D could be estimated for one pixel per image and by summing $f_{2,E}$ over the energies the radiation dose D_{stack} per pixel per stack. With a flux of approximately $8\times10^6\,\frac{\mathrm{photons}}{\mathrm{s}}$, dwell times of 2 ms and 3 ms, $\eta = 52\%$, D and D_{stack} were calculated for a stack of 96 images at the C K-edge and are listed in Tab. 6.2. The average dose D was calculated for $E = 290$ eV and is in the range of $10^4 - 10^5$ Gy per image, the total dose for one

stack is about $10^6 - 10^7$ Gy. According to Kirz et al. [107], about 10^5 Gy lead to structural changes in biologic specimens, but also experiments applying doses of 10^7 Gy have been reported with only small structural changes [180].

Table 6.2: *Radiation doses per pixel per image (D) and per stack (D_{stack}); details about the values are given in the text.*

sample	D [Gy]	D_{stack} [Gy]
dried, fixed	2.2×10^5	1.5×10^7
aqueous, fixed	3.3×10^4	1.8×10^6
dried, unfixed	7.9×10^5	4.9×10^6
living	2.4×10^5	1.5×10^7

6.4 Recapitulation

The x-ray microscopy study of VSMCs demonstrates that the intracellular structures can be imaged, and comparison with fluorescence pictures of fixed cells allowed for determining actin rich parts and thick actin bundles. The images recorded with the compact TXM are of comparable validity to the ones gained with the STXM at BESSY II regarding absorption contrast and resolution.
Although only reference spectra of pristine DNA, lipids and model proteins could be used, similar spectral patterns were found and the cell parts in the ROIs could be assigned. The Ca spectra showed that the concentration in the fixed cells is only half as high as for the unfixed cells. In the latter, isolated Ca hotspots were detected, and the concentration of Ca in these distinct locations could be estimated to be two times higher than in the actin rich parts of the unfixed VSMCs. Using Equ. (6.2), the Ca concentration in the cells and the hotspots was estimated. Since no comparable results were found in the literature, an interpretation needs further studies. The spectra also showed the need to carefully prepare spectroscopic experiments because of the danger of destroying the sample due to radiation damage. In the case of the detection of Ca, elemental mapping might have given better results. On the other hand, the thin samples allowed for experimenting in transmission mode, for which the radiation dose is much smaller.
The influence of the different preparation methods is observable in the experiments. While the absorption contrast of the cytoskeleton is improved by fixation of the cells, it is harder to recognize such structures in the unfixed cells. The results show qualitatively how much of the cell matter is actually lost during the fixation process.
Further experiments shall focus on cells that have been marked with green fluorescence protein, to enable the assignment of structures of the cytoskeleton of unfixed or even living cells in x-ray images. Apart from the Ca edges also experiments involving energies around the N (409.9 eV) or O (523 eV) K-edges, or in general other absorption edges of elements in the water window, could yield additional data for determining the intracellular

structures. Because of the radiation damage, tomography of non-vitrified cells is not possible. However, taking just a few images at different angles could provide further information about the spatial arrangements of the organelles and structures of a cell [68].

7 Conclusion

The investigation of environmental and biological samples using x-rays was the subject of this work. Applying soft x-ray spectroscopy, microscopy and spectromicroscopy, the samples were studied in dry and wet state, paying particular attention to the carbon content. The findings of the different sample systems build upon each other, going from bulk measurements to spectromicroscopic probing in the nm-scale. Apart from that, the experiments were selected in a way to expand the instrumental or analytical methods, by using synchrotron based and laboratory based compact source instruments, and developing new approaches to inerpret the data.

Usually, NEXAFS spectra of bulk samples, e.g., from polymer, environmental or biomolecular science, are recorded at synchrotron facilities. In Chapter 4, the C 1s spectra of PI, HAs, an aquatic FA, and a soil, are reported, with a spectrometer working with a laser driven Kr plasma source. The flux and spectral resolution are lower than at storage rings, but because of the highly heterogeneous sample composition this is not a major drawback. Due to that, the analysis of the spectra using linear combination of reference standards would not have been feasible. Thus, a semi-empirical approach was developed to analyze the spectra and draw conclusions to the organic composition. The PI was used as first reference sample of well-known structure. A commercially available HA was used to verify the approach. The results of both are well comparable to literature values. Apart from that it was possible to monitor the effects of different solvents and the stepwise extraction of the commercial HA. Especially for fast testing of such experiments, compact sources are important. To extent the range of samples to study, small wet chambers could be established, such as described in Fig. 5.3a. Other filters than Ti windows or different target materials would allow to assess the L_I-edge of sulfur or the N K-edge. The possibility to study samples in reflection mode would for example allow to study clays at the K and Ca $L_{II,III}$-edges and interactions with organic films.

For the investigation of CNTs and their interaction with soil colloids in Chapter 5, spatial resolution was needed. It was shown that these anthropogenic materials are retrievable from their NEXAFS spectrum, and from their structure, if they were still intact or at least long enough. The peak assignments from the bulk measurements in Chapter 4 were helpful to analyze these samples. For the first time, CNTs and soil colloids were probed in spectromicroscopic experiments in wet state. It turned out, that even supposedly unmodified inert CNTs interact chemically with the surrounding soil colloids in water. To a certain level of complexity, the interactions at interfaces could be simulated by superposition of the single component spectra of the samples. It has been reported that natural organic

matter could be acting as stabilizers for CNTs [87, 162]. A continuation of the experiments, eventually involving different pH-values or different HAs, would therefore be important. Furthermore, the biodegradation of CNTs by bacteria could be studied in a similar manner as has been done with bacterial processes involving calcium [20] mangan [201]. Other interactions of anthropogenic substances in soils were studied, too, but not described here. First experiments with charcoal and siderophores, iron-chelating compounds produced by bacteria or artificially, have already been conducted. The experiments with siderophores will be continued by K. Haselwandter (Innsbruck university) in the fall of 2011.
Apart from that, the CNTs in their pristine form were used to develop an alternative analysis approach. It is based on solving a constrained optimization problem emerging from the Lambert-Beer equation by means of box constraint algorithms. First results are promising, but the prove that the problem is convex and converges has to be shown, yet.
The application of the same soft x-ray techniques to radiation sensitive biological organisms was the topic of the last experiment. VSMCs were investigated, and cell organelles and parts of the cytoskeleton were recognized. Besides, traces of Ca sparks, usually detected by measuring ion current through the cell walls, could be identified. The main focus laid on monitoring the effect of different sample preparation methods, in detail, the comparison of chemically fixed samples to unfixed and even initially alive VSMC samples. The chemical fixation preserved the shape of the cell and also the cytoskeleton, but a major part of the intracellular structure is lost. Spectroscopic investigations are therefore best done with unfixed cells, and to avoid diffusion of material with unfixed and dry cells. Studies aiming at distinct chemical components, such as Ca or trace metals should be carried out using elemental mapping. Initially alive cells could be imaged with high precision, even several times without severe losses in structure. The radiation dose is of course not negligible and was estimated to be around 10^6 Gy per image. This implies that even three dimensional information of living cells without cryo fixation could by gained by applying stereo microscopy [23, 68]. This could also be achieved using a compact source x-ray microscope - it was also demonstrated that VSMCs can be imaged with such an instrument, although only with a fixed sample.
The subject of project B5 in the the *SFB 755 - Nanoscale Photonic Imaging* was the investigation of environmental samples in the nm-range. The experiments conducted in the course of this thesis and the gained results testing new instrumentation and analysis fit well within this context.

A CCD of the STXM at BESSY II

The data recorded at the STXM at BESSY II were transformed to *pgm*-files and the signal I_{real} was spread over the full possible range of 16 bit, i.e., 65535, determining the signal I_{pgm}. According to Wiesemann [212], it is

$$I_{pgm} = \frac{I_{real} - m}{M - m} \cdot 65535, \tag{A.1}$$

with m the minimal and M the maximal number of ADC-counts, the signal of the analog to digital converter of the CCD. From the ADC-counts N_{ADC}, the number of photons N_{phot} reaching the detector can be calculated, using

$$N_{phot} = \frac{N_{ADC}}{0.00551 \frac{\text{counts}}{\text{eV}\cdot\text{photons}} \cdot E[\text{eV}] \cdot \tau}. \tag{A.2}$$

The transformation factor $0.00551 \frac{\text{counts}}{\text{eV}\cdot\text{photons}}$ and the quantum efficiency $\eta = 52\,\%$ are determined by the CCD [211].
The analysis was performed using the values of the *pgm*-files instead of using the original data, as the exact conversion equation was not known at that time. For this reason, no calibration bars are given with the images taken at this STXM, to avoid giving wrong numbers. However, this is possible in good approximation to evaluate solely the *pgm*-files, because the number of photons in the focus, after having traversed a Si_3N_4-membrane and an organic sample specimen, is in the range of $2 - 6 \times 10^6$ photons. This fits well into the range of the *pgm*-files.
The analysis was always carried out within one stack, such that the relations and to some extent the quantitative statements are consistent. For the analysis of the CNT experiments, only qualitative statements regarding peak relations were made. In the analysis of the cell experiments, quantitative statements on the calcium content are made. These should be correct concerning the order of magnitude and the relations, but the exact numbers could be different, if I_{real} was used instead. For the estimate of the radiation damage, the values were taken from Wiesemann [211], and the photon flux on the sample was verified, by taking an image of the OSA (order sorting aperture) without a mounted sample.

B Cell Preparation

The steps for cultivating the VSMCs and fixation procedure are described here. The VSMCs were kept as aliquots in liquid nitrogen. The base of the culture medium was low glucose DMEM, for a ready-to-use medium, 500 ml DMEM, 50 ml FCS (fetal calf serum, Sigma F9665 from Sigma Aldrich), 5 ml Pen-Strep (penicillin streptomycin) and 5 ml glutamine are needed. The CO_2-independent culture medium is prepared in the same way, but instead of DMEM, CO_2-independent medium is used. Apart from the FCS, all chemicals were purchased from Invitrogen (Karlsruhe). The PBS buffer was diluted to 1× concentration, the 10× concentration was prepared with 1.37 M NaCl, 27 mM KCl, 43 mM $Na_2HPO_4 \cdot 12H_2O$ and 14 mM KH_2PO_4

Cultivating The culture medium was warmed to 37°C in a water bath. The cryo-vessels with the cells were taken out of the liquid nitrogen and put into the water bath only to thaw them, not to warm them. Under a flowbench a cell cultivating dish (diameter 3.5 cm, height 1 cm, Falcon) was filled with 2 ml culture medium. The cells were pipetted into the medium and the culture dish is incubated for 24 h (37°C, 5 % CO_2). After incubation, adsorption of the cells to the surface of the dish was checked with a light microscope. Under the flowbench, the culture dish was cleaned by suction, rinsed with PBS (phosphate buffered saline, 37°C, 1 %) and filled with culture medium again. That way, the cryoprotectant DMSO (dimethyl sulfoxide) was removed. The cells were then incubated again.
After the cells had sufficiently grown, they were resuspended with trypsin (Invitrogen). To do so, the culture medium was removed under the flowbench and 0.4 ml trypsin were added. After 5 min in the incubator all cells had dissolved from the culture dish. 2 ml of culture medium were added and the suspension was pipetted into 15 ml centrifuge tubes. The tubes are centrifuged for 10 min at 800 rpm. Meanwhile, the Si_3N_4-membranes were put in collagen (conc.: $1 \frac{mg}{ml}$) for 10 min and afterwards rinsed with purified H_2O (Millipore). Then they were placed in a 2 ml culture dish (3 per dish).
The cells in the centrifuge tube had then formed a pellet. The supernatant medium with the trypsin was removed by suction and the cells were resuspended in 2 ml fresh culture medium. Then, the suspension was pipetted onto the Si_3N_4-membranes in the culture dish, and the dishes were incubated for 24 h - 4h h. If necessary, the culture medium was exchanged again.

VSMCs transported alive For the experiments with initially alive VSMCs and dry, but unfixed cells, the culture medium was exchanged with the CO_2-independent medium

and incubated for 24 h. Afterwards, the Si_3N_4-membranes were put into 1.5 ml Eppendorf vessels, filled with CO_2-independent medium, ready to be transported to the synchrotron facility. The cells prepared that way could be kept alive for at least 3 days.

Fixed VSMCs Before fixation, the culture medium was removed and the samples in the culture dish were rinsed with PBS (37°C). After removing the PBS, the VSMCs were chemically fixed by adding 1 ml 4 % paraformaldehyde (2 mg PFA, 30 µl 1M NaOH, 50 ml PBS) and keeping them on ice for 10 min - 20 min. After that they were washed three times with PBS. For transport, the Si_3N_4-membranes with the fixed cells were kept in 1.5 ml Eppendorf vessels in purified H_2O.

Fluorescence marking The cell membrane of the chemically fixed cells is permeabilized with 0.5 % Triton X-100 (Sigma Aldrich) for 10 min - 20 min at room temperature (2 ml per culture dish). After that, the Si_3N_4-membranes in the dishes were rinsed three times with PBS. As markers, rhodamine-phalloidine was used for the actin fibres, DAPI was used to mark the nuclei. Per dish, 20 µl of the fluorescent dyes and 760 µl PBS with 1 % BSA (bovine serum albumin, Sigma Aldrich) were added. The BSA restored the cell membranes. The culture dishes are kept at room temperature without light for one hour to give the fluorescent markers time to bind. Afterwards, the Si_3N_4-membranes with the fixed and marked cells were rinsed in the dishes three times with PBS with 1 % BSA. They were stored in buffer or purified H_2O, while imaging them with a fluorescence light microscope. For transport, the Si_3N_4-membranes with the fixed cells were kept in 1.5 ml Eppendorf vessels in purified H_2O.
If stored in the fridge, the chemically fixed cells were stable for several months.

Bibliography

[1] H. ADE and H. STOLL: Near-edge X-ray absorption fine-structure microscopy of organic and magnetic materials. *Nature Materials* **8**(4) pp. 281–290, 2009.

[2] H. ADE, A. P. SMITH, H. ZHANG, G. R. ZHUANG, J. KIRZ, E. RIGHTOR and A. P. HITCHCOCK: X-ray Spectromicroscopy of polymers and tribological surfaces at beamline X1A at the NSLS. *Journal of Electron Spectroscopy and Related Phenomena* **84**(1-3) pp. 53–72, 1997.

[3] B. K. AGARWAL: *X-Ray Spectroscopy: An Introduction* (Springer Verlag, Heidelberg, Germany), 2 ed., 1991.

[4] C. AHL, K. W. BECKER, R. G. JÖRGENSEN and H. WILDHAGEN: *Aspekte und Grundlagen der Bodenkunde* (Eigenverlag, Germany), 2007.

[5] J. ALS-NIELSEN and D. MCMORROW: *Elements of Modern X-Ray Physics* (CRC Press Taylor & Francis Group, Boca Raton, FL, USA), 2001.

[6] A. L. ANKUDINOV, B. RAVEL, J. J. REHR and S. D. CONRADSON: Real-space multiple-scattering calculation and interpretation of x-ray-absrption near-edge structure. *Physical Review B* **58**(12) pp. 7565–7575, 1998.

[7] N. W. ASHCROFT and N. D. MERMIN: *Solid State Physics* (Thomson Learning, Cornell, NY; USA), 21 ed., 2000.

[8] D. ATTWOOD: *Soft X-Rays and Extreme Ultraviolet Radiation: Principles and Applications* (Cambridge University Press, Cambridge, UK), 2000.

[9] D. ATTWOOD: *Lecture Fall 2005: Soft X-Rays and Extreme Ultraviolet Radiation, Chapter 6*. Berkeley University, Berkeley, CA, USA, 2005. URL `http://ast.coe.berkeley.edu//sxreuv/2005/Ch05_2005.pdf`, retrieved Jan. 2011.

[10] I. BÅLDEA, B. SCHIMMELPFENNIG, M. PLASCHKE, J. ROTHE, J. SCHIRMER, A. B. TROFIMOV and T. FANGHÄNEL: C 1s near edge X-ray absorption fine structure (NEXAFS) of substituted benzoic acids–A theoretical and experimental study. *Journal of Electron Spectroscopy and Related Phenomena* **154** pp. 109–118, 2007.

[11] S. BANERJEE, T. HEMRAJ-BENNY, M. BALASUBRAMANIAN, D. FISCHER, J. MISEWICH and S. WONG: Ozonized single-walled carbon nanotubes investigated using NEXAFS spectroscopy. *Chemical Commununications* **2004**(7) pp. 772–773, 2004.

[12] S. BANERJEE, T. HEMRAJ-BENNY, M. BALASUBRAMANIAN, D. A. FISCHER, J. A. MISEWICH and S. S. WONG: Surface Chemistry and Structure of Purified, Ozonized, Multiwalled Carbon Nanotubes Probed by NEXAFS and Vibrational Spectroscopies. *ChemPhysChem* **5**(9) pp. 1416–1422, 2004.

[13] U. VON BARTH and G. GROSSMANN: Dynamical effects in x-ray spectra and the final-state-rule. *Physical Review B* **25**(8) pp. 5150–5179, 1982.

[14] I. BAUER: *Redox Activity of Humic Substances and their Role as Electron Mediators between Microorganisms and Fe(III) minerals in Anoxic Aquifers.* Ph.D. thesis, Eberhard-Karls-Universität, Tübingen, Germany, 2009.

[15] I. BAUER and A. KAPPLER: Rates and Extent of Reduction of Fe(III) Compounds and O_2 by Humic Substances. *Environmental Science & Technology* **43**(13) pp. 4902–4908, 2009.

[16] T. BEETZ: *Soft X-ray diffraction imaging with and without lenses and Radiation damage studies.* Ph.D. thesis, State University of New York, Stony Brook, NY, USA, 2004.

[17] T. BEETZ and C. JACOBSEN: Soft X-ray radiation-damage studies in PMMA using a cryo-STXM. *Journal of Synchrotron Radiation* **10**(3) pp. 280–283, 2003.

[18] M. BENZ, B. SCHINK and A. BRUNE: Humic Acid Reduction by *Propionibacterium freudenreichii* and Other Fermenting Bacteria. *Applied and Environmental Microbiology* **64**(11) pp. 4507–4512, 1998.

[19] K. BENZERARA, T. YOON, T. TYLISZCZAK, B. CONSTANTZ, A. SPORMANN and G. B. JR: Scanning transmission X-ray microscopy study of microbial calcification. *Geobiology* **2**(4) pp. 249–259, 2004.

[20] K. BENZERARA, N. MENGUY, P. LÓPEZ-GARCÍA, T. H. YOON, J. KAZMIERCZAK, T. TYLISZCZAK, F. GUYOT and G. E. B. JR.: Nanoscale detection of organic signatures in carbonate microbialites. *Proceedings of the National Academy of Sciences* **103**(25) pp. 9440–9445, 2006.

[21] M. BERTILSON: *Laboratory Soft X-Ray Microscopy and Tomography.* Ph.D. thesis, Royal Institute of Technology, Stockholm, Sweden, 2011.

[22] M. C. BERTILSON, P. A. C. TAKMAN, A. HOLMBERG, U. VOGT and H. M. HERTZ: Laboratory arrangement for soft x-ray zone plate efficiency measurements. *Review of Scientific Instruments* **78**(026103), 2007.

[23] M. C. BERTILSON, O. VON HOFSTEN, J. THIEME, M. LINDBLOM, A. HOLMBERG, P. A. C. TAKMAN, U. VOGT and H. M. HERTZ: First application experiments with the Stockholm compact soft x-ray microscope. *Journal of Physics: Conference Series* **186** p. 012025, 2009.

[24] P. M. BERTSCH and D. B. HUNTER: Applications of Synchrotron-Based X-ray Microprobes. *Chemical Reviews* **101** pp. 1809–1842, 2001.

[25] E. BETZIG, G. H. PATTERSON, R. SOUGRAT, O. W. LINDWASSER, S. OLENYCH, J. S. BONIFACINO, M. W. DAVIDSON, J. LIPPINCOTT-SCHWARTZ and H. F. HESS: Imaging Intracellular Fluorescent Proteins at Nanometer Resolution. *Science* **313**(5793) pp. 1642–1645, 2006.

[26] J. BOESE, A. OSANNA, C. JACOBSEN and J. KIRZ: Carbon edge XANES spectroscopy of amino acids and peptides. *Journal of Electron Spectroscopy and Related Phenomena* **85**(1-2) pp. 9–15, 1997.

[27] K. BRADLEY, J.-C. P. GABRIEL and G. GRÜNER: Flexible Nanotube Electronics. *Nano Letters* **3** pp. 1353–1355, 2003.

[28] J. A. BRANDES, C. LEE, S. WAKEHAM, M. PETERSON, C. JACOBSEN, S. WIRICK and G. CODY: Examining marine particulate organic matter at sub-micron scales using scanning transmission X-ray microscopy and carbon X-ray absorption near edge structure spectroscopy. *Marine Chemistry* **92** pp. 107–121, 2004.

[29] A. BRAUN: Carbon speciation in airborne particulate matter with C (1s) NEXAFS spectroscopy. *Journal of Environmental Monitoring* **7**(11) pp. 1059–1065, 2005.

[30] A. BRAUN, S. WIRICK, A. KUBÁTOVÁ, B. MUN and F. HUGGINS: Photochemically induced decarboxylation in diesel soot extracts. *Atmospheric Environment* **40**(30) pp. 5837–5844, 2006.

[31] A. BRAUN, F. HUGGINS, A. KUBATOVA, S. WIRICK, M. MARICQ, B. MUN, J. MCDONALD, K. KELLY, N. SHAH and G. HUFFMAN: Toward distinguishing woodsmoke and diesel exhaust in ambient particulate matter. *Environmental Science & Technology* **42**(2) pp. 374–380, 2007.

[32] H. BUBERT, J. LAMBERT and P. BURBA: Structural and elemental investigations of isolated aquatic humic substances using X-ray photoelectron spectroscopy. *Fresenius Journal of Analytical Chemistry* **2**(368) pp. 274–280, 2000.

[33] C. J. BUCKLEY: Measuring and mapping in mineralized tissues by absorption difference imaging. *Review of Scientific Instruments* **66**(2) pp. 1318–1321, 1995.

[34] M. W. BUCKLEY and N. A. BESLEY: A theoretical study of the near edge X-ray absorption fine structure of amino acids and proteins. *Chemical Physical Letters* **501**(4-6) pp. 540–546, 2011.

[35] L. G. BULUSHEVA, A. V. OKOTRUB, Y. V. LAVSKAYA, D. V. VYALIKH, U. DETTLAFF-WEGLIKOWSKA, A. FONSECA and K. HATA: Comparative NEXAFS examination of single-wall carbon nanotubes produced by different methods. *Physica Status Solidi B* **246**(11-12) pp. 2637–2640, 2009.

[36] G. BUNKER: *Introduction to XAFS - A Practical Guide to X-Ray Absorption Fine Structure Spectroscopy* (Cambridge University Press, Cambridge, UK), 2011.

[37] G. BUNKER: *XAFS tutorial documents*. xafs.org, 2011. URL `http://gbxafs.iit.edu/training/tutorials.html`, retrieved Mar. 2011.

[38] V. CARRAVETTA, O. PLASHKEVYCH and H. A. GREN: A theoretical study of the near-edge x-ray absorption spectra of some larger amino acids. *Journal of Chemical Physical* **109**(4) pp. 1456–1464, 1998.

[39] W. CHAO, J. KIM, S. RAKEWA, P. FISCHER and E. H. ANDERSON: Demonstration of 12 nm Resolution Fresnel Zone Plate Lens based Soft X-Ray Microscopy. *Optics Express* **17**(20) pp. 17669–17667, 2009.

[40] M. A. CHAPPELL, A. J. GEORGE, K. M. DONTSOVA, B. E. PORTER, C. L. PRICE, P. H. ZHOU, E. MORIKAWA, A. J. KENNEDY and J. A. STEEVENS: Surfactive stabilization of multi-walled carbon nanotube dispersions with dissolved humic substances. *Environmental Pollution* **157**(4) pp. 1081–1087, 2009.

[41] H. CHENG and W. LEDERER: Calcium sparks. *Physiological Reviews* **88**(4) pp. 1491–1545, 2008.

[42] I. CHRISTL and R. KRETZSCHMAR: C-1s NEXAFS spectroscopy reveals chemical fractionation of humic acid by cation-induced coagulation. *Environmental Science & Technology* **41**(6), 2007.

[43] G. CODY, R. BOTTO, H. ADE, S. BEHAL, M. DISKO and S. WIRICK: Innershell spectroscopy and imaging of a subbituminous coal–in situ analysis of organic and inorganic microstructure using C (1s)-NEXAFS, Ca (2p)-NEXAFS, and C1 (2s)-NEXAFS. *Energy & Fuels* **9**(3) pp. 525–33, 1995.

[44] G. CODY, H. ADE, S. WIRICK, G. MITCHELL and A. DAVIS: Determination of chemical-structural changes in vitrinite accompanying luminescence alteration using C-NEXAFS analysis. *Organic Geochemistry* **28**(7-8) pp. 441–455, 1998.

[45] P. CONTE and A. PICCOLO: Conformational Arrangement of Dissolved Humic Substances. Influence of Solution Composition on Association of Humic Molecules. *Environmental Science & Technology* **33**(10) pp. 1682–1690, 1999.

[46] R. COONEY and S. URQUHART: Chemical Trends in the Near-Edge X-ray Absorption Fine Structure of Monosubstituted and Para-Bisubstituted Benzenes. *Journal of Physical Chememistry B* **108**(47) pp. 18185–18191, 2004.

[47] CXRO: *X-Ray Interactions With Matter*. Center for X-Ray Optics, Lawrence Berkeley National Laboratory (LBNL), Berkeley, CA USA, 2011. URL `http://henke.lbl.gov/optical_constants`, retrieved Jan. 2011.

[48] CXRO: *XM-1*. Center for X-Ray Optics, Lawrence Berkeley National Laboratory (LBNL), Berkeley, CA USA, 2011. URL `http://cxro.lbl.gov/XM1`, retrieved Jan. 2011.

[49] G. DENBEAUX, E. ANDERSON, W. CHAO, T. EIMÜLLER, L. JOHNSON, M. KÖHLER, C. LARABELL, M. LEGROS, P. FISCHER and A. PEARSON: Soft X-ray microscopy to 25 nm with applications to biology and magnetic materials. *Nuclear Instruments and Methods in Physics Research Section A: Accelerators, Spectrometers, Detectors and Associated Equipment* **467** pp. 841–844, 2001.

[50] O. DHEZ, H. ADE and S. URQUHART: Calibrated NEXAFS spectra of some common polymers. *Journal of Electron Spectroscopy and Related Phenomena* **128** pp. 85–96, 2003.

[51] O. DHEZ, H. ADE and S. URQUHART: Website: Polymers NEXAFS Spectroscopy. 2010. `http://www.physics.ncsu.edu/stxm/polymerspectro/` retrieved 15-03-2010.

[52] M. D. DYAR, J. S. DELANEY and S. R. SUTTON: Fe XANES spectra of iron-rich micas. *European Journal of Mineralogy* **13**(6) pp. 1079–1098, 2001.

[53] A. EGNER and S. W. HELL: Fluorescence microscopy with super-resolved optical sections. *Trends in Cell Biology* **15**(4) pp. 207–215, 2005.

[54] F. EINSIEDL, B. MAYER and T. SCHÄFER: Evidence for incorporation of H2S in groundwater fulvic acids from stable isotope ratios and sulfur K-edge X-ray absorption near edge structure spectroscopy. *Environmental Science & Technology* **42**(7) pp. 2439–2444, 2008.

[55] M. E. ESSLINGTON: *Soil and water chemistry: an integrative approach* (CRC Press, Boca Raton, FL, USA), 2004.

[56] N. FAKHRI, F. C. MACKINTOSH, B. LOUNIS, L. COGNET and M. PASQUALI: Brownian Motion of Stiff Filaments in a Crowded Environment. *Science* **330**(6012) pp. 1804–1807, 2010.

[57] FEFF-PROJECT: John J. Rehr and Fernando Vila and Micah Prange and Joshua Kas and Yoshinari Takimoto and Adam Sorini and Kevin Jorissen and Aleksi Soininen and Alex Ankudinov and Towfiq Ahmed, University of Washington, WA, USA, 2011. URL `http://leonardo.phys.washington.edu/feff/`, retrieved Mar. 2011.

[58] A. FELTEN, H. HODY, C. BITTENCOURT, J.-J. PIREAUX, D. H. CRUZ and A. P. HITCHCOCK: Scanning transmission x-ray microscopy of isolated multiwall carbon nanotubes. *Applied Physics Letters* **89**(9) p. 093123, 2007.

[59] H. FIEDOROWICZ: Generation of soft X-rays and extreme ultraviolet (EUV) using a laser-irradiated gas puff target. *Laser and Particle Beams* **23**(03) pp. 365–373, 2005.

[60] R. L. FIMMEN, R. M. CORY, Y. P. CHIN, T. D. TROUTS and D. M. MCKNIGHT: Probing the oxidation-reduction properties of terrestrially and microbially derived dissolved organic matter. *Geochimica et Cosmochimica Acta* **71**(12) pp. 3003–3015, 2007.

[61] M. E. FLEET and X. LIU: Calcium L2, 3-edge XANES of carbonates, carbonate apatite, and oldhamite (CaS). *American Mineralogist* **94**(8-9) p. 1235, 2009.

[62] J. T. FRANCIS and A. P. HITCHCOCK: Inner-shell spectroscopy of p-benzoquinone, hydroquinone, and phenol: Distinguishing quinoid and benzenoid structures. *The Journal of Physical Chemistry* **96**(16) pp. 6598–6610, 1992.

[63] F. H. FRIMMEL, G. ABBT-BRAUN and K. G. HEUMANN: *Refractory Organic Substances in the Environment* (Wiley-VCH, New York, USA), 2002.

[64] B. FUGETSU, S. SATOH, T. SHIBA, T. MIZUTANI, Y.-B. LIN, N. TERUI, Y. NODASAKA, K. SASA, K. SHIMIZU, T. AKASAKA, M. SHINDOH, K. ICHIRO SHIBATA, A. YOKOYAMA, M. MORI, K. TANAKA, Y. SATO, K. TOHJI, S. TANAKA, N. NISHI and F. WATARI: Caged Multiwalled Carbon Nanotubes as the Adsorbents for Affinity-Based Elimination of Ionic Dyes. *Environmental Science & Technology* **38** pp. 6890–6896, 2004.

[65] K. GIEWEKEMEYER, P. THIBAULT, S. KALBFLEISCH, A. BEERLINK, C. KEWISH, M. DIEROLF, F. PFEIFFER and T. SALDITT: Quantitative biological imaging by ptychographic x-ray diffraction microscopy. *Proceedings of the National Academy of Sciences* **107**(2) p. 529, 2010.

[66] G. GLEBER, J. THIEME, J. NIEMEYER and M. FESER: Interaction of organic substances with iron studied by O1s spectroscopy - Development of an analysis program. *Journal de Physique IV* **104** pp. 3153–3168, 2003.

[67] S.-C. GLEBER: *Soft X-ray stereo microscopy for investigation of dynamics and elemental distribution of colloidal systems from the environment.* Ph.D. thesis, Georg-August-Universität Göttingen, 2009.

[68] S.-C. GLEBER, J. THIEME, W. CHAO and P. FISCHER: Stereo soft X-ray microscopy and elemental mapping of haematite and clay suspensions. *Journal of Microscopy* **235**(2) pp. 199–208, 2009.

[69] T. GRECO, R. HODARA, I. PARASTATIDIS, H. HEIJNEN, M. DENNEHY, D. LIEBLER and H. ISCHIROPOULOS: Identification of S-nitrosylation motifs by site-specific mapping of the S-nitrosocysteine proteome in human vascular smooth muscle cells. *Proceedings of the National Academy of Science* **103**(19) pp. 7420–7425, 2006.

[70] F. DE GROOT and A. KOTANI: *Core Level Spectroscopy of Soils* (John Wiley & Sons, Ltd., West Sussex, UK), 2001.

[71] P. GUTTMANN, S. HEIM, S. WERNER, B. NIEMANN, R. FOLLATH and G. SCHNEIDER: X-ray microscopy at the new U41-FSGM beam line. *BESSY - Annual Report 2007* pp. 297–300, 2007.

[72] B. L. HENKE, E. GULLIKSON and J. DAVIS: X-ray interactions: Photoabsorption, scattering, transmission, and reflection at E = 50 - 30,000 eV, Z = 1 - 92. In *Atomic Data and Nuclear Data Tables*, vol. 54 (Lawrence Berkeley National Laboratory), 1993.

[73] H. M. HERTZ, M. BERTILSON, E. CHUBAROVA, J. EWALD, S.-C. GLEBER, O. HEMBERG, M. HENRIKSSON, O. V HOFSTEN, A. HOLMBERG, M. LINDBLOM, E. MUDRY, M. OTENDAL, J. REINSPACH, M. SCHLIE, P. SKOGLUND, P. A. C. TAKMAN, J. THIEME, J. SEDLMAIR, R. TJÖRNHAMMER, T. TUOHIMAA, M. VITA and U. V. U: Laboratory x-ray micro imaging: Sources, optics, systems and applications. *Journal of Physics: Conference Series* **186** p. 012027, 2009.

[74] H. M. HERTZ, M. BERTILSON, O. VON HOFSTEN, S.-C. GLEBER, J. SEDLMAIR and J. THIEME: Laboratory x-ray microscopy for high-resolution imaging of environmental colloid structure. *Chemical Geology* 2010. Submitted.

[75] O. HIGNETTE, P. CLOETENS, G. ROSTAING, P. BERNARD and C. MORAWE: Efficient sub 100 nm focusing of hard x rays. *Review of Scientific Instruments* **76** p. 063709, 2005.

[76] A. HITCHCOCK: Website: Gas Phase Core Excitation Database. 2009. `http://unicorn.mcmaster.ca/corex/cedb-title.html` retrieved 10-02-2009.

[77] A. HITCHCOCK, C. MORIN, X. ZHANG and T. ARAKI: Soft X-ray spectromicroscopy of biological and synthetic polymer systems. *Journal of Electron Spectroscopy and Related Phenomena* **144-147** pp. 259–269, 2005.

[78] A. P. HITCHCOCK, J. J. DYNES, G. JOHANSSON, J. WANG and G. BOTTON: Comparison of NEXAFS microscopy and TEM-EELS for studies of soft matter. *Micron* **39**(6) pp. 741–8, 2008.

[79] J. HLAVAY, T. PROHASKA, M. WEISZ, W. W. WENZEL and G. J. STINGEDER: Determination of trace elements bound to soils and sediment fractions. *Pure and Applied Chemistry* **76**(2) pp. 415–442, 2004.

[80] A. HOLMBERG, S. REHBEIN and H. M. HERTZ: Nano-fabrication of condenser and micro-zone plates for compact X-ray microscopy. *Microelectronic Engineering* **73–74** pp. 639–643, 2004.

[81] T. HOTZ ET AL.: Drift estimation for single marker switching based imaging schemes. unpublished.

[82] M. HOWELLS, C. JACOBSEN and T. WARWICK: Principles and Applications of Zone Plate X-Ray Microscopes. In P. W. HAWKES and J. C. H. SPENCE (Eds.), *Science of Microscopy* (Springer, New York, NY, USA), 2007.

[83] B. HUANG, W. WANG, M. BATES and X. ZHUANG: Three-Dimensional Super-Resolution Imaging by Stochastic Optical Reconstruction Microscopy. *Science* **319**(5864) pp. 810–813, 2008.

[84] X. HUANG, J. NELSON, J. KIRZ, E. LIMA, S. MARCHESINI, H. MIAO, A. NEIMAN, D. SHAPIRO, J. STEINBRENER, A. STEWART, J. TURNER and C. JACOBSEN: Soft X-Ray Diffraction Microscopy of a Frozen Hydrated Yeast Cell. *Physical Review Letters* **103**(19) p. 198101, 2009.

[85] G. HUFFMAN, S. MITRA, F. HUGGINS, N. SHAH, S. VAIDYA and F. LU: Quantitative analysis of all major forms of sulfur in coal by X-ray absorption fine structure spectroscopy. *Energy & Fuels* **5**(4) pp. 574–581, 1991.

[86] H. HYANG, J. D. FORTNER, J. B. HUGHES and J.-H. KIM: Natural Organic Matter Stabilizes Carbon Nanotubes in the Aqueous Phase. *Environmental Science & Technology* **41**(1) pp. 179–184, 2007.

[87] H. HYUNG, J. D. FORTNER, J. B. HUGHES and J.-H. KIM: Natural Organic Matter Stabilizes Carbon Nanotubes in the Aqueous Phase. *Environmental Science & Technology* **41**(1) pp. 179–184, 2007.

[88] HZDR: Helmholtz Zentrum Dresden Rossendorf, Helmholtz Gemeinschaft, 2010. URL `http://www.hzdr.de/db/Cms?pNid=38&pOid=10883`, retrieved Jul. 2010.

[89] G. HÄHNER: Near edge X-ray absorption fine structure spectroscopy as a tool to probe electronic and structural properties of thin organic films and liquids. *Chemical Society Reviews* **35**(12) pp. 1244–1255, 2006.

[90] S. IIJIMA: Helical microtubules of graphitic carbon. *Nature* **354**, 1991.

[91] I. ISHII and A. P. HITCHCOCK: A quantitative experimental study of the core excited electronic states of formamide, formic acid, and formyl fluoride. *Journal of Chemical Physics* **87** p. 830, 1987.

[92] I. ISHII and A. P. HITCHCOCK: The oscillator strengths for C1s and O1s excitation of some saturated and unsaturated organic alcohols, acids and esters. *Journal of electron spectroscopy and related phenomena* **46**(1) pp. 55–84, 1988.

[93] C. JACOBSEN, S. ABEND, T. BEETZ, M. CARLUCCI-DAYTON, M. FESER, K. KAZNACHEYEV, J. KIRZ, J. MASER, U. NEUHÄUSLER and A. OSANNA: Recent Development in Scanning Microscopy at Stony Brook. *AIP Conference Proceedings* **507** pp. 12–18, 2000.

[94] C. JACOBSEN, S. WIRICK, G. FLYNN and C. ZIMBA: Soft X-ray spectroscopy from image sequences with sub-100 nm spatial resolution. *Journal of Microscopy* **197**(2) pp. 173–184, 2000.

[95] C. JACOBSEN ET AL.: Website: X1-A x-ray absorption spectra. 2010. `http://xray1.physics.sunysb.edu/ micros/xas/xas.html` retrieved 15-03-2010.

[96] G. JANDL, P. LEINWEBER, H.-R. SCHULTEN and K. EUSTERHUES: The concentrations of fatty acids in organo-mineral particle - size fractions of a Chernozem. *European Journal of Soil Science* **55** pp. 459–469, 2004.

[97] R. JANIAK, S. WILSON, S. MONTAGUE and J. HUME: Heterogeneity of calcium stores and elementary release events in canine pulmonary arterial smooth muscle cells. *American Journal of Physiology-Cell Physiology* **280**(1) pp. C22–33, 2001.

[98] P. A. C. JANSSON, U. VOGT and H. M. HERTZ: Liquid-nitrogen-jet laser-plasma for compact soft x-ray microscopy. *Review of Scientific Instruments* **76** p. 043503, 2005.

[99] A. JAVEY, J. GUO, D. B. FARMER, Q. WANG, E. YENILMEZ, R. G. GORDON, M. LUNDSTROM and H. DAI: Self-Aligned Ballistic Molecular Transistors and Electrically Parallel Nanotube Arrays. *Nano Letters* **4**(7) pp. 1319–1322, 2004.

[100] I. T. JOLLIFFE: *Principle Component Analysis* (Springer, New York, NY, USA), 2 ed., 2002.

[101] Y. JOLY: X-ray absorption near-edge structure calculations beyond the muffin-tin approximation. *Physical Review B* **63**(12) p. 125120, 2001.

[102] K. KAZNACHEYEV, A. OSANNA, C. JACOBSEN, O. PLASHKEVYCH, O. VAHTRAS, H. ÅGREN, V. CARRAVETTA and A. P. HITCHCOCK: Inner-Shell Absorption Spectroscopy of Amino Acids. *Journal of Chemical Physics* **46**(106) pp. 55–84, 2002.

[103] B. P. KELLEHER and A. J. SIMPSON: Humic substances in soils: are they really chemically distinct? *Environmental Science & Technology* **40**(15) pp. 4605–4611, 2006.

[104] S. KHAN: Free-electron lasers. *Journal of Modern Optics* **55**(21) pp. 3469–3512, 2008.

[105] J. KIKUMA and B. P. TONNER: XANES spectra of a variety of widely used organic polymers at the C K-edge. *Journal of Electron Spectroscopy and Related Phenomena* **82**(1–2) pp. 53–60, 1996.

[106] S. D. KILLOPS and V. J. KILLOPS: *An Introduction to Organic Geochemistry* (Wiley-Blackwell, New York, USA), 2005.

[107] J. KIRZ, C. JACOBSEN and M. HOWELLS: Soft x-ray microscopes and their biological applications. *Quarterly Reviews of Biophysics* **28**(1) pp. 33–130, 1995. Reprinted 2009.

[108] C. KOLCZEWSKI, R. PÜTTNER, M. MARTINS, A. S. SCHLACHTER, G. SNELL, M. M. SANT'ANNA, K. HERMANN and G. KAINDL: Spectroscopic analysis of small organic molecules: a comprehensive near-edge x-ray-absorption fine-structure study of C6-ring-containing molecules. *Journal of Chemical Physics* **124**(3) p. 034302, 2006.

[109] M. O. KRAUSE: Atomic Radiative and Radiationless Yields for K and L Shells. *Journal of Chemical and Physical Reference Data* **8**(2) pp. 307–327, 1979.

[110] A. KUZNETSOVA, I. POPOVA, J. Y. JR, M. BRONIKOWSKI, C. HUFFMAN, J. LIU, R. SMALLEY, H. HWU and J. CHEN: Oxygen-containing functional groups on single-wall carbon nanotubes: NEXAFS and vibrational spectroscopic studies. *Journal of the American Chemical Society* **123**(43) pp. 10699–10704, 2001.

[111] C. LAM, J. T. JAMES, R. MCCLUSKEY, S. AREPALLI and R. L. HUNTER: A Review of Carbon Nanotube Toxicity and Assessment of Potential Occupational and Environmental Health Risks. *Critical Reviews in Toxicology* **36**(3) pp. 189–217, 2006.

[112] K. LANGE and J. GARTZKE: F-actin-based Ca signaling – a critical comparison with the current concept of Ca signaling. *Journal of Cellular Physiology* **209**(2) pp. 270–287, 2006.

[113] C. A. LARABELL and M. A. L. GROS: X-ray tomography generates 3-D reconstructions of the yeast, saccharomyces cerevisiae, at 60 nm- resolution. *Molecular Biology of the Cell* **15**(3) pp. 957–62, 2004.

[114] J. LAWRENCE, G. SWERHONE, G. LEPPARD, T. ARAKI, X. ZHANG, M. WEST and A. P. HITCHCOCK: Scanning transmission X-ray, laser scanning, and transmission electron microscopy mapping of the exopolymeric matrix of microbial biofilms. *Applied and environmental microbiology* **69**(9) p. 5543, 2003.

[115] R. D. LEAPMAN: Novel techniques in electron microscopy. *Current opinion in neurobiology* **14**(5) pp. 591–598, 2004.

[116] J. LEHMANN, J. KINYANGI and D. SOLOMON: Organic matter stabilization in soil microaggregates: implications from spatial heterogeneity of organic carbon contents and carbon forms. *Biogeochemistry* **85** pp. 45–57, 2007.

[117] M. LEROTIC: *Finding the patterns in complex specimens by improving the acquisition and analysis of x-ray spectromicroscopy.* Ph.D. thesis, State University of New York, Stony Brook, NY, USA, 2005.

[118] M. LEROTIC, C. JACOBSEN, T. SCHÄFER and S. VOGT: Cluster analysis of soft X-ray spectromicroscopy data. *Ultramicroscopy* **100** pp. 35–57, 2004.

[119] G. MCDERMOTT, M. A. L. GROS, C. G. KNOECHEL, M. UCHIDA and C. A. LARABELL: Soft X-ray tomography and cryogenic light microscopy: the cool combination in cellular imaging. *Trends in Cell Biology* **19**(11) pp. 587–95, 2009.

[120] G. MCGEOWN: GL Brown Lecture 2010: Seeing is believing: imaging Ca2+-signalling events in living cells. *Experimental Physiology* **95**(11) pp. 1049–1060, 2010.

[121] W. MEYER-ILSE, D. HAMAMOTO, A. NAIR, S. A. LELIÉVRE, G. DENBEAUX, L. JOHNSON, A. L. PEARSON, D. YAGER, M. A. LEGROS and C. A. LARABELL: High resolution protein localization using soft X-ray microscopy. *Journal of Microscopy* **201**(3) pp. 395–403, 2001.

[122] H. MIMURA, S. MORITA, T. KIMURA, D. YAMAKAWA, W. LIN, Y. UEHARA, S. MATSUYAMA, H. YUMOTO, H. OHASHI and K. TAMASAKU: Focusing mirror for x-ray free-electron lasers. *Review of Scientific Instruments* **79** p. 083104, 2008.

[123] G. MITREA, J. THIEME, P. GUTTMANN, S. HEIM and S.-C. GLEBER: X-ray spectromicroscopy with the scanning transmission X-ray microscope at BESSY II. *Journal of Synchrotron Radiation* **15**(1) pp. 26–35, 2008.

[124] H. MODROW, S. BUCHER, J. J. REHR and A. L. ANKUDINOV: Calculation and interpretation of K-shell x-ray absorption near-edge structure of transition metal oxides. *Physical Review B* **67**(3) p. 035123, 2003.

[125] F. MONTEIL-RIVERA, E. BROUWER and S. MASSET: Combination of X-ray photoelectron and solid-state ^{13}C nuclear magnetic resonance spectroscopy in the structural characterisation of humic acids. *Analytica Chimica Acta* **424** pp. 243–255, 2000.

[126] C. MORAWE and M. OSTERHOFF: Hard X-Ray Focusing with Curved Reflective Multilayers. *X-Ray Optics and Instrumentation* **2010**, 2010.

[127] R. S. MULLIKEN: Molecular Orbital Method and Molecular Ionization Potentials. *Physical Review* **74**(7) pp. 736–738, 1948.

[128] R. S. MULLIKEN: *Spectroscopy, Molecular Orbitals, and Chemical Bonding - Nobel Lecture 1966.* Nobel Lectures, Chemistry 1963-1970 (Elsevier Publishing Company, Amsterdam, The Netherlands), 1972. URL `http://nobelprize.org/chemistry/laureates/1966/mulliken-lecture.html`.

[129] S. C. B. MYNENI: Soft X-ray Spectroscopy and Spectromicroscopy Studies of Organic Molecules in the Environment. *Reviews in Mineralogy and Geochemistry* **49**(1) pp. 485–579, 2002.

[130] A. NASIBULIN, S. SHANDAKOV, L. NASIBULINA, A. CWIRZEN, P. MUDIMELA, K. HABERMEHL-CWIRZEN, D. GRISHIN, Y. GAVRILOV, J. MALM and U. TAPPER: A novel cement-based hybrid material. *New Journal of Physics* **11** p. 023013, 2009.

[131] T. R. NEU, B. MANZ, F. VOLKE, J. J. DYNES, A. P. HITCHCOCK and J. R. LAWRENCE: Advanced imaging techniques for assessment of structure, composition and function in biofilm systems. *FEMS Microbiology Ecology* **72** pp. 1–21, 2010.

[132] NIST: *X-Ray Form Factor, Attenuation and Scattering Tables.* National Institute of Standards and Technology (NIST), U.S. Commerce Department, USA, 2011. URL `http://physics.nist.gov/PhysRefData/FFast/html/form.html`, retrieved Jan. 2011.

[133] J. NOCEDAL and S. J. WRIGHT: Numerical Optimization. In T. V. MIKOSCH, S. I. RESNICK and S. R. ROBINSON (Eds.), *Springer Series in Operations Research and Financial Engineering* (Springer Verlag, New York, NY, USA), 2 ed., 2006.

[134] K. L. I. NORLUND, G. SOUTHAM, T. TYLISZCAK, Y. HU, C. KARUNKARAN, M. OBST, A. P. HITCHCOCK and L. A. WARREN: Microbial Architecture of Environmental Sulfur Processes: A Novel Syntrophic Sulfur-Metabolizing Consortia. *Organic Geochemistry* **43**(23) pp. 8781–8786, 2009.

[135] E. NOVÁKOVÁ, G. MITREA, C. PETH, J. THIEME, K. MANN and T. SALDITT: Solid supported multicomponent lipid membranes studied by x-ray spectromicroscopy. *Biointerphases* **3**(2) pp. 44–54, 2008.

[136] A. OSANNA: *Soft X-ray Spectromicroscopy with a Cryo Scanning Transmission X-ray Microscope.* Ph.D. thesis, State University of New York, Stony Brook, NY, USA, 2000.

[137] S. PAGEL-WIEDER, J. NIEMEYER, W. R. FISCHER and F. G. F: Effects of physical and chemical properties of soils on adsorption of the insecticidal protein (Cry1Ab) from Bacillus thuringiensis at Cry1Ab protein concentrations relevant for experimental field sites. *Soil Biology and Biochemistry* **39**(12) pp. 3034–3042, 2007.

[138] B. J. PANESSA-WARREN, M. M. MAYE, J. B. WARREN and K. M. M. CROSSON: Single walled carbon nanotube reactivity and cytotoxicity following extended aqueous exposure. *Environmental Pollution* **157**(4) pp. 1088–1094, 2009.

[139] I. PARKER, J. CHOI and Y. YAO: Elementary events of InsP3-induced Ca2+ liberation in Xenopus oocytes: hot spots, puffs and blips. *Cell Calcium* **20**(2) pp. 105–121, 1996.

[140] D. Y. PARKINSON, G. MCDERMOTT, L. D. ETKIN, M. A. L. GROS and C. A. LARABELL: Quantitative 3-D imaging of eukaryotic cells using soft X-ray tomography. *Journal of Structural Biology* **162**(3) pp. 380–6, 2008.

[141] C. PETH: *XUV-Laserplasmaquellen für die Absorptions-Spektroskopie und zeitaufgelöste Röntgenbeugung*. Ph.D. thesis, Georg-August-Universität Göttingen, 2008a.

[142] C. PETH, A. KALININ, F. BARKUSKY, K. MANN, J. P. TOENNIES and L. Y. RUSIN: XUV laser-plasma source based on solid Ar filament. *Review of Scientific Insruments* **78**(10) p. 103509, 2007.

[143] C. PETH, F. BARKUSKY and K. MANN: Near-edge x-ray absorption fine structure measurements using a laboratory-scale XUV source. *Journal of Physics D: Applied Physics* **41**(10) p. 105202, 2008b.

[144] C. PETH, F. BARKUSKY, J. SEDLMAIR, S.-C. GLEBER, E. NOVÁKOVÁ, J. NIEMEYER, J. THIEME, T. SALDITT and K. MANN: Near-Edge X-Ray Absorption Fine Structure Measurements Using a Laser Plasma XUV Source. *Journal de Physique Conference Series* **186** p. 0120032, 2009.

[145] K. PILLAYA, E. CUKROWSKAB and N. COVILLE: Multi-walled carbon nanotubes as adsorbents for the removal of parts per billion levels of hexavalent chromium from aqueous solution. *Journal of Hazardous Matter* **166**(2-3) pp. 1067–1075, 2008.

[146] P. PLUCIŃSKI, Z. GÓRSKI and J. SŁAWIŃSKI: RESISTANCE OF MODEL HUMIC ACIDS TO ULTRAVIOLET-C RADIATION. *Acta Agrophysica* **9**(1) pp. 191–202, 2007.

[147] M. PRATO, K. KOSTARELOS and A. BIANCO: Functionalized carbon nanotubes in drug design and discovery. *Accounts of Chemical Research* **41**(1) pp. 60–68, 2007.

[148] R-PROJECT: Robert Gentleman and Ross Ihaka, 1992. URL `http://www.r-project.org/`, retrieved Mar. 2011.

[149] H. RARBACK, C. BUCKLEY, H. ADE, F. CAMILO, R. DIGENNARO, S. HELLMAN, M. HOWELLS, N. ISKANDER, C. JACOBSEN, J. KIRZ, S. KRINSKY, S. LINDAAS, I. MCNULTY, M. OVERSLUIZEN, S. ROTHMAN, D. SAYRE, M. SHARNOFF and D. SHU: Coherent

Radiation for X-ray Imaging–The Soft X-ray Undulator and the X1A Beamline at the NSLS. *Journal of X-Ray Science and Technology* **2**(4) pp. 274–296, 1990.

[150] J. J. REHR and R. C. ALBERTS: Theoretical approaches to x-ray absorption fine structure. *Reviews in Modern Physics* **72**(3) pp. 621–653, 2000.

[151] J. J. REHR and A. L. ANKUDINOV: Progress in the theory and interpretation of XANES. *Coordination Chemistry Review* **249**(1-2) pp. 131–140, 2005.

[152] J. J. REHR, A. L. ANKUDINOV and S. I. ZABINSKI: New developments in NEXAFS/EXAFS theory. *Catalysis Today* **39**(4) pp. 263–269, 1998.

[153] M. REIBOLD, P. PAUFLER, A. A. LEVIN, W. KOCHMANN, N. PÄTZKE and D. C. MEYER: Materials: Carbon nanotubes in an ancient Damascus sabre. *Nature* **286**(444), 2006.

[154] G. RESCH, K. GOLDIE, A. KREBS, A. HOENGER and J. SMALL: Visualisation of the actin cytoskeleton by cryo-electron microscopy. *Journal of Cell Science* **115**(9) pp. 1877–1882, 2002.

[155] A. L. RODRIGUES, A. G. BRITO, P. JANKNECHT, J. SILVA, A. V. MACHADO and R. NOGUEIRA: Characterization of biofilm formation on a humic material. *Journal of Industrial Microbiology and Biotechnology* **35**(11) pp. 1269–1276, 2008.

[156] M. J. RUST, M. BATES and X. ZHUANG: Sub-diffraction-limit imaging by stochastic optical reconstruction microscopy (STORM). *Nat Methods* **3**(10) pp. 793–796, 2006.

[157] L. RYMELL and H. M. HERTZ: Droplet target for low-debris laser-plasma soft X-ray generation. *Optics Communications* **103** pp. 105–110, 1993.

[158] N. B. SALEH, L. D. PFEFFERLE and M. ELIMELECH: Influence of Biomacromolecules and Humic Acid on the Aggregation Kinetics of Single-Walled Carbon Nanotubes. *Environmental Science & Technology* **44**(7) pp. 2412–2418, 2010.

[159] M. SAMANT, J. STÖHR, H. BROWN, T. RUSSELL, J. SANDS and S. KUMAR: NEXAFS studies on the surface orientation of buffed polyimides. *Macromolecules* **29**(26) pp. 8334–8342, 1996.

[160] D. E. SAYERS, E. A. STERN and F. W. LYTLE: New Technique for Investigating Noncrystalline Structures: Fourier Analysis of the Extended X-Ray—Absorption Fine Structure. *Physical Review Letters* **27**(18) pp. 1204–1207, 1971.

[161] F. SCHEFFER and P. SCHACHTSCHABEL: *Lehrbuch der Bodenkunde* (Spektrum), 16 ed., 2010.

[162] A. SCHIERZ and H. ZAENKER: Aqueous suspensions of carbon nanotubes: Surface oxidation, colloidal stability and uranium sorption. *Environmental Pollution* **157**(4) pp. 1140–1151, 2009.

[163] G. SCHNEIDER, P. GUTTMANN, S. HEIM, S. REHBEIN, F. MUELLER, K. NAGASHIMA, J. B. HEYMANN, W. G. MÜLLER and J. MCNALLY: Three-dimensional cellular ultrastructure resolved by X-ray microscopy. *Nature Methods* **7**(12) pp. 985–959, 2010.

[164] M. SCHUMACHER, I. CHRISTL, A. SCHEINOST, C. JACOBSEN and R. KRETZSCHMAR: Chemical heterogeneity of organic soil colloids investigated by scanning transmission X-ray microscopy and C-1s NEXAFS microspectroscopy. *Environmental Science & Technology* **39**(23) pp. 9094–9100, 2005.

[165] T. SCHÄFER, P. MICHEL, F. CLARET, T. BEETZ, S. WIRICK and C. JACOBSEN: Radiation sensitivity of natural organic matter: Clay mineral association effects in the Callovo-Oxfordian argillite. *Journal of Electron Spectroscopy and Related Phenomena* **170**(1-3) pp. 49–56, 2009.

[166] J. SEDLMAIR, S.-C. GLEBER, C. PETH, K. MANN, J. NIEMEYER and J. THIEME: Characterization of refractory organic substances by NEXAFS using a compact x-ray source. *Journal of Soils and Sediments* . URL `http://dx.doi.org/10.1007/s11368-011-0385-9`, in press 2011.

[167] J. SEDLMAIR, S.-C. GLEBER, S. WIRICK, P. GUTTMANN and J. THIEME: Interaction between Carbon Nanotubes and Soil Colloids Studied with X-Ray Spectromicroscopy. *Chemical Geology* . URL `http://dx.doi.org/10.1016/j.chemgeo.2011.08.009`, in press 2011.

[168] J. SEDLMAIR, S.-C. GLEBER, S. ÖZTÜRK MERT, M. BERTILSON, O. VON HOFSTEN, J. THIEME and T. PFOHL: Imaging of Vascular Smooth Muscle Cells with Soft X-Ray Spectromicroscopy. *Microscopy and Microanalysis* . In press 2011.

[169] J. SERES, V. S. YAKOLEV, E. SERES, C. STRELI, P. WOBRAUSCHEK, C. SPIELMANN and F. KRAUSZ: Coherent superposition of laser-driven soft-X-ray harmonics from successive sources. *Nature Physics* **3**(12) pp. 878–883, 2007.

[170] T. K. SHAM, B. X. YANG, J. KIRZ and J. S. TSE: K-edge near-edge x-ray-absorption fine structure of oxygen-and carbon-containing molecules in the gas phase. *Physical Review A* **40**(2) pp. 652–669, 1989.

[171] D. SHAPIRO, P. THIBAULT, T. BEETZ, V. ELSER, M. HOWELLS, C. JACOBSEN, J. KIRZ, E. LIMA, H. MIAO and A. NEIMAN: Biological imaging by soft x-ray diffraction microscopy. *Proceedings of the National Academy of Sciences USA* **102**(43) p. 15343, 2005.

[172] A. L. SHOBER, D. L. HESTERBERG, J. T. SIMS and S. GARDNER: Characterization of Phosphorus Species in Biosolids and Manures Using XANES Spectroscopy. *Journal of Environmental Quality* **35**(6) p. 1983, 2006.

[173] M. M. D. SIERRA, M. GIOVANELA, E. PARLANTI, V. ESTEVES, A. DUARTE, A. FRANSOZO and E. SORIANO-SIERRA: Structural Description of Humic Substances from Subtropical Coastal Environments using Elemental Analysis, FT-IR and ^{13}C-Solid State NMR Data. *Journal of Coastal Research* **42** pp. 370–382, 2005.

[174] B. SINGH and M. GRÄFE (Eds.): *Developments in Soil Science – Synchrotron -Based Techniques in Soils and Sediments* (Elsevier, Amsterdam, The Netherlands), 2010.

[175] J. V. SMALL, S. AUINGER, M. NEMETHOVA, S. KOESTLER, K. N. GOLDIE, A. HOENGER and G. P. RESCH: Unravelling the structure of the lamellipodium. *Journal of Microscopy* **231**(3) pp. 479–485, 2008.

[176] A. P. SMITH, S. G. URQUHART, D. A. WINESETT, G. MITCHELL and H. ADE: Use of Near Edge X-ray Absorption Fine Structure Spectromicroscopy to Characterize Multicomponent Polymeric Systems. *Applied Spectroscopy* **55**(12) pp. 1676–1681, 2001.

[177] C. J. SMITH and B. J. S. R. D. HANDY: Toxicity of single walled carbon nanotubes to rainbow trout, (Oncorhynchus mykiss): Respiratory toxicity, organ pathologies, and other physiological effects. *Aquatic Toxicology* **82**(2) pp. 94–109, 2007.

[178] D. SOLOMON, J. LEHMANN, J. KINYANGI, B. LIANG and T. SCHÄFER: Carbon K-edge NEXAFS and FTIR-ATR spectroscopic investigation of organic carbon speciation in soils. *Soil Science Society of America Journal* **69**(1) pp. 107–119, 2005.

[179] D. SOLOMON, J. LEHMANN, J. KINYANGI, B. LIANG, K. HEYMANN, L. DATHE, K. HANLEY, S. WIRICK and C. JACOBSEN: Carbon (1s) NEXAFS Spectroscopy of Biogeochemically Relevant Reference Organic Compounds. *Soil Science Society of America Journal* **73**(6) p. 1817, 2009.

[180] C. SONG, H. JIANG, A. MANCUSO, B. AMIRBEKIAN, L. PENG, R. SUN, S. S. SHAH, Z. H. ZHOU, T. ISHIKAWA, and J. MIAO: Quantitative Imaging of Single, Unstained Viruses with Coherent X Rays. *Physical Review Letters* **101**(8) p. 158101, 2008.

[181] D. SPARKS: *Environmental Soil Chemistry* (Academic Press, Elevier, San Diego, CL, USA), 2003.

[182] S. DI STASIO and A. BRAUN: Comparative NEXAFS Study on Soot Obtained from an Ethylene/Air Flame, a Diesel Engine, and Graphite. *Energy & Fuels* **20**(1) pp. 187–194, 2006.

[183] F. J. STEVENSON: *Humus Chemistry: Genesis, Composition, Reactions* (Wiley, New York, USA), 2nd ed., 1994.

[184] H. STOLLBERG, S. YULIN, P. A. C. TAKMAN and H. M. HERTZ: High-reflectivity Cr/Sc multilayer condenser for compact soft x-ray microscopy. *Review of Scientific Instruments* **77**(123101), 2006.

[185] Z. STRUYK and G. SPOSITO: Redox properties of standard humic acids. *Geoderma* **102**(3–4) pp. 329–346, 2001.

[186] D. STUDER, B. M. HUMBEL and M. CHIQUET: Electron microscopy of high pressure frozen samples: bridging the gap between cellular ultrastructure and atomic resolution. *Histochemistry and Cell Biology* **130**(5) pp. 877–889, 2008.

[187] J. STÖHR: *NEXAFS Spectroscopy* (Springer, Berlin, Germany), 1992.

[188] J. STÖHR, M. G. SAMANT, J. LUNING, A. C. CALLEGARI, P. CHAUDHARI, J. P. DOYLE, J. A. LACEY, S. A. LIEN, S. PURUSHOTHAMAN and J. L. SPEIDELL: Liquid crystal alignment on carbonaceous surfaces with orientational order. *Science* **292**(5525) pp. 2299–302, 2001.

[189] SUNY and NSLS: *STXM*. Stony Brook University NY and National Synchrotron Light Source, Brookhaven National Laboratoy (BNL), Stony Brook, NY, USA, 2011. URL `http://xray1.physics.sunysb.edu/research/intro2.php`, retrieved Jan. 2011.

[190] R. SUTTON and G. SPOSITO: Molecular Structure in Soil Humic Substances: The New View. *Environmental Science & Technology* **39**(23) pp. 9009–9015, 2005.

[191] P. A. TAKMAN, H. STOLLBERG, G. A. JOHANSSON, A. HOLMBERG, M. LINDBLOM and H. M. HERTZ: High-resolution compact X-ray microscopy. *Journal of Microscopy* **226**(2) pp. 175–181, 2007.

[192] I. TANAKA, T. MIZOGUCHI and T. YAMAMOTO: XANES and ELNES in ceramic science. *Journal of the American Ceramic Society* **88**(8) pp. 2013–2029, 2005.

[193] Y. H. TANG, T. K. SHAM, Y. F. HU, C. S. LEE and S. T. LEE: Near-edge X-ray absorption fine structure study of helicity and defects in carbon nanotubes. *Chemical Physics Letters* **366**(5-6) pp. 636–641, 2002.

[194] P. THIBAULT, V. ELSER, C. JACOBSEN, D. SHAPIRO and D. SAYRE: Reconstruction of a yeast cell from X-ray diffraction data. *Acta Crystallographica A - Foundations of Crystallography* **62**(4) pp. 248–261, 2006.

[195] J. THIEME, G. SCHNEIDER and C. KNÖCHEL: X-ray tomography of a microhabitat of bacteria and other soil colloids with sub-100 nm resolution. *Micron* **34**(6-7) pp. 339–344, 2003.

[196] J. THIEME, I. MCNULTY, S. VOGT and D. PATERSON: X-Ray Spectromicroscopy - A Tool for Environmental Sciences. *Environmental Science & Technology* **41**(20) pp. 6885–6889, 2007.

[197] J. THIEME, J. SEDLMAIR, S.-C. GLEBER, J. PRIETZEL, J. COATES, K. EUSTERHUES, G. ABBT-BRAUN and M. SALOME: X-ray spectromicroscopy in soil and environmental sciences. *Journal of Synchrotron Radiation* **17**(2) pp. 149–157, 2010.

[198] A. THOMPSON, D. VAUGHAN, J. KIRZ, D. ATTWOOD, E. GULLIKSON, M. HOWELLS, K.-J. KIM, J. KORTRIGHT, I. LINDAU, P. PIANATTA, A. ROBINSON, J. UNDERWOOD, G. WILLIAMS and H. WINICK: *X-ray Data Booklet* (Center for X-Ray Optics and Advanced Light Source, Lawrence Berkeley National Laboratory, Berkeley, CA, USA), 2nd ed., 2001.

[199] J. THYBERG: Differences in caveolae dynamics in vascular smooth muscle cells of different phenotypes. *Laboratory Investigation* **80**(6) pp. 915–929, 2000.

[200] E. TIPPING: *Cation Binding by Humic Substances* (Cambridge University Press, Cambridge, UK), 2002.

[201] B. TONER, S. F. ANS M VILLALOBOS, T. WARWICK and G. SPOSITO: Biofilm Production within a Bacterial of Biogenic Manganese Oxide Spatially Resolved Characterization. *Applied and Environmental Micorbiology* **71**(3) pp. 1300–1310, 2005.

[202] R. TUCOULOU, G. MARTINEZ-CRIADO, P. BLEUET, I. KIEFFER, P. CLOETENS, S. LABOURÉ, T. MARTIN, C. GUILLOUD and J. SUSINI: High-resolution angular beam stability monitoring at a nanofocusing beamline. *Journal of Synchrotron Radiation* **15**(4) pp. 392–398, 2008.

[203] K. W. URBAN: Studying atomic structures by aberration-corrected transmission electron microscopy. *Science* **321**(5888) pp. 506–510, 2008.

[204] S. G. URQUHART and H. ADE: Trends in the carbonyl core (C 1S, O 1S) $\rightarrow \pi^*_{C=O}$ transition in the near-edge X-ray absorption fine structure spectra of organic molecules. *Journal of Physical Chemistry B* **106**(34) pp. 8531–8538, 2002.

[205] S. G. URQUHART, A. P. HITCHCOCK, A. P. SMITH, H. W. ADE, W. LIDY, E. G. RIGHTOR and G. E. MITCHELL: NEXAFS spectromicroscopy of polymers: overview and quantitative analysis of polyurethane polymers. *Journal of Electron Spectroscopy and Related Phenomena* **100**(1-3) pp. 119–135, 1999.

[206] U. VOGT, R. FRUEKE, T. WILHEIN, H. STOLLBERG, P. JANSSON and H. M. HERTZ: High-resolution spatial characterization of laser produced plasmas at soft x-ray wavelengths. *Applied Physics B: Lasers and Optics* **78** pp. 53–58, 2004.

[207] I. H. WALTHER, R. L. JAFFE, E. M. KOTSALIS, T. WERDER, T. HALICIOGLU and P. KOUMOUTSAKOS: Hydrophobic hydration of C_60 and carbon nanotubes in water. *Carbon* **42**(5-6) pp. 1185–1194, 2004.

[208] J. WANG, C. MORIN, L. LI, A. P. HITCHCOCK, A. SCHOLL and A. DORAN: Radiation damage in soft X-ray microscopy. *Journal of Electron Spectroscopy and Related Phenomena* **170**(1-3) pp. 25–36, 2009.

[209] X. WANG, C. CHEN, W. HU, A. DING, D. XU and X. ZHOU: Sorption of ^{243}Am(III) to multiwall carbon nanotubes. *Environmental Science & Technology* **39**(8) pp. 2856–2860, 2005.

[210] Y. WANG, E. GRANADOS, M. A. LAROTONDA, M. BERRILL, B. M. LUTHER, D. PATEL, C. S. MENONI and J. J. ROCCA: High-brightness injection-seeded soft-x-ray-laser amplifier using a solid target. *Physical Review Letters* **97**(12) p. 123901, 2006.

[211] U. WIESEMANN: *The Scanning Transmission X-Ray Microscope at BESSY II.* Ph.D. thesis, Georg-August-Universität Göttingen, 2003.

[212] U. WIESEMANN: personal comunication. May 2011.

[213] U. WIESEMANN, J. THIEME, R. FRÜKE and P. GUTTMANN: Construction of a scanning transmission X-ray microscope at the undulator U-41 at BESSY II. *Nuclear Instruments and Methods in Physics Research A* **467–468** pp. 861–863, 2001.

[214] K. WILLIG, S. RIZZOLI, V. WESTPHAL, R. JAHN and S. HELL: STED microscopy reveals that synaptotagmin remains clustered after synaptic vesicle exocytosis. *Nature* **440**, 2006.

[215] B. WINN, H. ADE, C. BUCKLEY, M. FESER, S. HULBERT, C. JACOBSEN, K. KAZNACHEYEV, J. KIRZ, A. OSANNA, J. MASER, I. MCNULTY, J. MIAO, T. OVERSLUIZEN, S. SPECTOR, B. SULIVAN, Y. WANG, S. WIRICK and H. ZHANG: Illumination for coherent softX-ray applications: the new X1A beamline at the NSLS. *Journal of Synchrotron Radiation* **7**(6) pp. 395–404, 2000.

[216] K. XIA, F. WEESNER, W. F. BLEAM, P. A. HELMKE, P. R. BLOOM and U. L. SKYLLBERG: XANES Studies of Oxidation States of Sulfur in Aquatic and Soil Humic Substances. *Soil Science Society of America Journal* **62** pp. 1240–46, 1998.

[217] A. YAMAMOTO, R. MASAKI, P. GUTTMANN, G. SCHMAHL and H. KIHARA: Studies on intracellular structures of COS cells by X-ray microscopy. *Journal of Synchrotron Radiation* **5**(3) pp. 1105–1107, 1998.

[218] C. YUAN, C.-H. HUNG and K.-C. CHEN: Electrokinetic remediation of arsenate spiked soil assisted by CNT-Co barrier – The effect of barrier position and processing fluid. *Journal of Hazardous Materials* **171**(1-3) pp. 563–570, 2009.

[219] H. ZAENKER: Colloidal carbon nanotubes and their influence on dissolved uranium. In *Nuclear Safety Research*, vol. 3 of *FZD Biennial Scientific Report 2007-2008* (Forschungszentrum Dresden-Rossendorf), 2009.

[220] H. ZAENKER: personal comunication. 2009, 2010, 2011.

[221] D. ZENISEK, V. DAVILA, L. WAN and W. ALMERS: Imaging calcium entry sites and ribbon structures in two presynaptic cells. *The Journal of neuroscience* **23**(7) pp. 2538–2548, 2003.

[222] M. ZEPF, B. DROMEY, M. LANDREMAN, P. FOSTER and S. M. HOOKER: Bright Quasi-Phase-Matched Soft-X-Ray Harmonic Radiation from Argon Ions. *Physical Review Letters* **99**(12) p. 143901, 2007.

[223] J. ZHONG, L. SONG, D. YAN, Z. WU, C. WANG, S. XIE and H. QIAN: A XANES characterization of structural defects in single-walled carbon nanotubes. *Radiation Physics and Chemistry* **75**(11) pp. 1861–1865, 2006.

[224] H. ÅGREN, V. CARRAVETTA, O. VAHTRAS and L. G. M. PETTERSSON: Direct, atomic orbital, static exchange calculations of photoabsorption spectra of large molecules and clusters. *Chemical Physics Letters* **222**(1-2) pp. 75–81, 1994.

Publications

- J. M. SEDLMAIR, S.-C. GLEBER, S. ÖZTÜRK, M. BERTILSON, O. V. HOFSTEN, J. THIEME AND T. PFOHL: Imaging of Vascular Smooth Muscle Cells with Soft X-Ray Spectromicroscopy. *Microscopy and Microanalysis*, in press, 2011.
- J. M. SEDLMAIR, S.-C. GLEBER, S. WIRICK, P. GUTTMANN AND J. THIEME: Interaction between Carbon Nanotubes and Soil Colloids Studied with X-Ray Spectromicroscopy. *Chemical Geology*, DOI: 10.1016/j.chemgeo.2011.08.009, in press, 2011.
- J. SEDLMAIR S.-C. GLEBER, C. PETH, K. MANN, J. NIEMEYER AND J. THIEME: Characterization of refractory organic substances by NEXAFS by using a compact X-ray source. *Journal of Soils and Sediments*, DOI: 10.1007/s11368-011-0385-9 „ in press, 2011.
- J. SEDLMAIR, S.-C. GLEBER, S. ÖZTÜRK, T. PFOHL, P. GUTTMANN, S. WIRICK AND J. THIEME: X-Ray Spectromicroscopy of Biomolecular Matter and Soils. *AIP Conference Proceedings* **1365**, in press, 2010.
- J. THIEME, J. SEDLMAIR, S.-C. GLEBER, J. PRIETZEL, J. COATES, K. EUSTERHUES, G. ABBT-BRAUN, M. SALOME: X-ray spectromicroscopy in geo- and environmental sciences. *Journal of Synchrotron Radiation* **17**(1), pp. 149–157, 2010.
- J. THIEME, S.-C. GLEBER, J. SEDLMAIR, J. RIEGER, J. NIEMEYER, J. COATES: X-ray spectromicroscopy studies of nanoparticles in aqueous media. In R. NIESSNER AND F. H. FRIMMEL (Eds.), *Nanoparticles in the Water Cycle* (Springer, Heidelberg), pp. 103–115, 2010.
- J. SEDLMAIR, S.-C. GLEBER, C. PETH, K. MANN AND J. THIEME: NEXAFS spectroscopy with a laser plasma x-raysource on soil samples *Journal of Physics: Conference Series* **186**, p. 012034, 2009.
- J. THIEME, J. SEDLMAIR, S.-C. GLEBER, M. BERTILSON, O. V. HOFSTEN, P. TAKMAN AND H. M. HERTZ: High-resolution imaging of soil colloids in aqueous media with a compact soft X-ray microscope *Journal of Physics: Conference Series* **186**, p. 012107, 2009.
- S.-C. GLEBER, J. SEDLMAIR, M. BERTILSON, O. V. HOFSTEN, S. HEIM, P. GUTTMANN, H. M. HERTZ, P. FISCHER AND J. THIEME: X-ray stereo microscopy for investigation of dynamics in soils *Journal of Physics: Conference Series* **186**, p. 012104, 2009.

- C. PETH, F. BARKUSKY, J. SEDLMAIR, S.-C. GLEBER, E. NOVAKOVA, J. NIEMEYER, J. THIEME, T. SADLITT AND K. MANN: Near-Edge X-Ray Absorption Fine Structure Measurements Using a Laser Plasma XUV Source. *Journal of Physics: Conference Series* **186**, p. 012104, 2009.

- H. M. HERTZ, M. BERTILSON, E. CHUBAROVA, J. EWALD, S.-C. GLEBER, O. HEMBERG, M. HENRIKSSON, O. V. HOFSTEN, A. HOLMBERG, M. LINDBLOM, E. MUDRY, M. OTENDAL, J. REINSPACH, M. SCHLIE, P. SKOGLUND, P. TAKMAN, J. THIEME, J. SEDLMAIR, R. TJÖRNHAMMAR, T. TUOHIMAA, M. VITA AND U. VOGT: Laboratory x-ray micro imaging: Sources, optics, systems and applications *Journal of Physics: Conference Series* **186**, p. 012027, 2009.

- J. MORFILL, F. KÜHNER, K. BLANK, R. A. LUGMAIER, J. SEDLMAIR, H. E. GAUB: B-S transition in short oligonucleotides. *Biophysical Journal* **93**(7), 2007.

Acknowledgements

Zuallererst möchte ich mich bei dem Betreuer meiner Arbeit Dr. Jürgen Thieme bedanken, für die spannende Themenstellung, für die Einführung in ein für mich völlig neues Gebiet, und dafür, mich mit seiner Begeisterung für interdiziplinäre Fragen anzustecken. In der gesamten Zeit habe ich von seinem Wissen über Mikroskopie und Spektroskopie, den Diskussionen (nicht nur) zu meiner Arbeit und seiner (auch nach dem Umzug) fast ständigen Erreichbarkeit profitiert.
Großer Dank gilt auch meinem Doktorvater Prof. Dr. Tim Salditt: für die Möglichkeit meine Doktorarbeit an seinem Institut anzufertigen, für die Freiheiten, die er mir dabei gelassen hat aber auch dafür, zu wissen, wann ich einen Motivationsschub gebrauchen konnte; außerdem für die hilfreichen Kommentare zu meiner Arbeit und die organisatorische Unterstützung in der Endphase.
Ich danke Prof. Dr. Thomas Pfohl für die Zusammenarbeit am Zellprojekt und darüber hinaus, für die Zustimmung einer meiner Prüfer zu sein, die überaus schnellen und immer freundlichen E-Mail-Antworten und außerdem dafür, mir zeitweise die Weiterführung meiner Arbeit als Teil seiner Gruppe ermöglicht zu haben.
Dr. Jürgen Niemeyer danke ich für seine Geduld mit dem NEXAFS-Paper, die unvergleichlichen Gespräche dazu und die Einblicke in Chemie, Umwelt und mehr.
Prof. Dr. Sarah Köster danke ich für eine hervorragende Vorlesung zu weicher Materie, für die immer offene Tür, für die Möglichkeit einige der Experimente in ihrem Labor vorzubereiten und die Ermutigungen.
Ich bedanke mich ausserdem bei Prof. Dr. Hans-Ulrich Krebs dafür, dass er das Koreferat meiner Arbeit übernommen hat.
Ein herzlicher Dank an Dr. Sophie-Charlotte Gleber für das Durchlesen von Manuskripten, wissenschaftliche und nicht wissenschaftliche Gespräche, optimalst ausgenutzte Mess- und Dienstreisen, die Nachmittage auf dem Balkon oder am See, Hundephobietherapie und vieles andere, was eine Freundschaft entstehen ließ.
Mareike Mathes ist eine großartige Bürokollegin und inzwischen Freundin, die nicht nur mit mir Konferenzbeiträge u.ä. durchgegangen ist, des weiteren hat sie viele meiner kleinen und großen Anliegen und Albernheiten über sich ergehen lassen. Danke dafür!
Besonderer Dank gilt auch Dr. Christian Peth und Dr. Klaus Mann für die Zusammenarbeit bei den Huminstoffexperimenten. Ohne Christians Bereitschaft so häufig zu messen, wären die Versuche nicht möglich gewesen.
Dr. Harald Zaenker und Dr. Ariette Schierz danke ich für die Zusammenarbeit beim CNT-Projekt und den aufschlussreichen Diskussionen zu diesem Thema.

Außerdem danke ich Dr. Thomas Hotz für seine Denkanstöße zur Auswertung spektromikroskopischer Daten und seiner Geduld bei der Erklärung der mathematischen Sachverhalte.
Mein Dank geht auch Semra Öztürk-Mert für die großartige Hilfe und Einweisung bei der Zellpräparation.
I thank Prof. Dr. Hans Hertz and his group for the opportunity to work with the compact TXM and it was always a great pleasure to meet again. Special thank goes to Olov von Hofsten and Michael Bertilson, not only for the support during and after the experiments, but also for the enjoyable reunions at the XRM IX and XRM X.
Vielen Dank auch an die Mitarbeiter am BESSY II für die hervorragenden Arbeitsbedingungen. Insbesondere danke ich Dr. Peter Guttmann für seine Unterstützung bei den Messungen am STXM und für die schnelle Beantwortung aller zusätzlichen Fragen.
I am also thankful to the staff at the NSLS for providing excellent working conditions. Due to the expertise of Sue Wirick, the CNT-experiments at the X1-A microscope worked out so well.
Herzlicher Dank geht an die Mitglieder des IRP für die gute Stimmung am Institut, die hilfreichen Tipps beim D-Café und das Engagement zur Feierei. Ebenso gilt mein Dank den Mitgliedern des SFB für die Schaffung einer einzigartigen Atmosphäre. Im Zuge dessen möchte ich mich ganz herzlich bei Eva Hetzel und Kerstin Grüny bedanken, besonders dafür, dass sie sich meist sofort um meine Anliegen gekümmert haben, wenn ich bei ihnen unangemeldet in der Tür stand. Außerdem vielen Dank an Dr. Jörg Hallmann, der mit Engelsgeduld und der angemessenen Ernsthaftigkeit meine Arbeit korrigiert hat.
Diese Arbeit hätte nicht fertiggestellt werden können, ohne die Unterstützung vieler Freunde, neu gefundene in Göttingen, alte in München, und in der Welt verstreute, die trotzdem immer für mich da waren. Alle aufzuzählen wäre zu lang, ihr wisst, wer gemeint ist, aber kurz erwähnen möchte ich Eva, die immer wieder nachfragt und mich aufbaut.
Mein größter Dank gilt meiner Familie, ohne deren Unterstützung und Zuneigung ich mein Studium und diese Arbeit nicht hätte vollbringen können. Ihr wisst, wie wichtig ihr für mich seid. Mama, Papa, Jonas – Danke für alles!

Lebenslauf

Julia Maria Sedlmair
Geboren am 17. Dezember 1981 in München
Staatsangehörigkeit: deutsch

Wissenschaftlicher Werdegang

7/2001	Erlangung der Allgemeinen Hochschulreife, Städtisches Luisengymnasium München
10/2001–7/2003	Studium der Physik an der Ludwig-Maximilians-Universität München
09/2004–1/2005	Studium der Physik an der Lunds Universitet, Schweden
2/2005–7/2007	Studium der Physik an der Ludwig-Maximilians-Universität München
7/2007	Diplom in Physik, Schwerpunkt Biophysik, Titel der Arbeit: "Kraftspektroskopie an doppelsträngiger DNA – Auswirkungen externer und interner Modifikationen", bei Prof. Dr. H. E. Gaub, Lehrstuhl für Angewandte Physik und Biophysik, Ludwig-Maximilians-Universität München
seit 11/2007	wissenschaftliche Mitarbeiterin am Institut für Röntgenphysik, Georg-August-Universität Göttingen

Soft x-ray spectromicroscopy was used to investigate environmental and biological specimens paying particular attention to their carbon content, of organic or anthropogenic origin. To be more specific, energies in the spectral region of the so-called water window, between the K absorption edges of carbon (284 eV) and oxygen (523 eV), were applied. In this region the absorbance of substances of high carbon content such as proteins is ten times higher than the absorbance of water which provides natural contrast and in turn allows for a natural or close to natural environment for such samples. The experiments presented in this thesis were chosen in such a way that either new instruments or new analysis methods are studied on different non-model sample specimens. To understand the effect of nanoparticles on the environment, the interaction between carbon nanotubes and soil was monitored, both in dry and aqueous sample environment. Additionally, for the characterization of heterogeneous samples like soils, spectroscopic experiments with a laser driven plasma source were performed. It demonstrated the feasibility of such a complementary technique, if not sometimes alternative to NEXAFS studies using synchrotron radiation. In the third project the possibility to image vascular smooth muscle cells without the necessity of additional embedding or staining was inquired, but by applying a simple, non-cryo fixation sample preparation.

GEORG-AUGUST-UNIVERSITÄT
GÖTTINGEN

ISBN 978-3-86395-036-1
ISSN 2191-9860

Universitätsverlag Göttingen